# Device Engineering of AlN/Si based substrate template for Deep Ultraviolet Applications



Engr. Syed Hasan Murtaza Bokhari

Registration No. 91-FET-PhDEE/S15

A dissertation submitted to IIU in partial fulfilment

of the requirements for the degree of

DOCTOR OF PHILOSOPHY

Supervised by

Prof. Dr. Ahmed Shujit Syed

Department of Electrical Engineering Faculty of Engineering and Technology

INTERNATIONAL ISLAMIC UNIVERSITY, ISLAMABAD

2022

PhD 620.5 BOD

Accession No THOS 74

Electrical properties materials science microelectronics -- Technological inmovations

\_\_\_\_\_



# CERTIFICATE OF APPROVAL

Title of Thesis: "Device Engineering of AlN/Si based substrate template for Deep Ultraviolet Applications".

Name of Student: Syed Hasan Murtaza Bokhari

Registration No: 91-FET/PHDEE/S15

Accepted by the Department of Electrical & Computer Engineering, Faculty of Engineering and Technology, International Islamic University (IIU), Islamabad, in partial fulfillment of the requirements for the Doctor of Philosophy degree in Electronic Engineering.

# Viva voce committee:

Prof. Dr. Ahmed Shuja Syed (Supervisor)

V.P (HS&R)IIUI/Professor/ Director, CAEPE

Dr. Gul Hassan(Internal)

Assistant Professor CAEPE, DECE, FET, IIU Islamabad.

Prof. Dr. Ehsan Ullah Khan (External-I)

Ex-PAEC/Professor, NAMAL University, Mianwali.

Prof. Dr. Salman Iqbal(External-II)

Director General/Professor. KICSIT.

Dr. Shahid Ikram (Chairman, DECE)

Assistant Professor DECE, FET, IIU Islamabad.

Prof. Dr. Nadeem Ahmad Sheikh (Dean, FET)

Professor DME, FET, IIU Islamabad.

Chassan

FLUIN\_

This thesis titled "Device Engineering of AlN/Si based substrate for Deep Ultraviolet Applications" is submitted by Engr. Syed Hasan Murtaza Bokhari Registration No.: 91-FET/PhDEE/S15 to the Faculty of Engineering and Technology(FET), International Islamic University Islamabad (IIUI), in partial fulfilment of the requirements for the degree of PhD Electronics Engineering.

The work presented in the thesis is carried out in the Center for Advanced Electronics and Photovoltaics Engineering, International Islamic University Islamabad.

This Thesis is dedicated to my late Father and my Mother

#### List of Publication

- i. Hassan, S., Ahmed, S., Ali, M., & Fahad, S. (2022). Advanced electrical characterization of AlN/Si based heterogeneous junction for photonic applications. *Materials Science in Semiconductor Processing*, 138, 106292. DOI:10.1016/j.mssp.2021.106292
- ii. Murtaza, S. H., Ahmed, S., & Ali, M. (2022). Investigation of AlN/Si based Heterogeneous Junction using Inter-digitated electrodes for enhanced UV Light Detection. Optik, 169534. <u>DOI:10.1016/j.ijleo.2022.169534</u>

## **Patent**

Title: A method of detecting low energy photon quanta from ultra-wide-bandgap Aluminum Nitride on Silicon (AlN/Si) using ion implantation technique [Filed in 2022]

Inventor 1: Prof. Dr. Ahmed Shuja Syed

Inventor 2: Engr. Syed Hasan Murtaza Bokhari

Inventor 3: Engr. Abdul Saboor

Inventor 4: Engr. Muhammad Ali

#### Abstract

Aluminium Nitride based devices are currently the hotbed of R&D for UV based detectors and generators. The direct wide band gap of Aluminum Nitride makes it best bet for UV devices. The lattice match of 19% and the dislocation density normally makes the junction of the Aluminium Nitride and Silicon problematic, Aluminium Nitride over Silicon (AlN/Si) based heterogeneous junction is investigated, herein, for photonic applications. A hyperfine layer of AIN onto the n-type Silicon substrate is fabricated, and a detailed analysis of subject stack has been carried out by variety of techniques such as Scanning Electron Microscopy (SEM), Current-Voltage (I-V), Capacitance-Voltage (C-V), Charge Deep Level Transient Spectroscopy (Q-DLTS), Transient of Photo-voltages (TPV) and Kinetics of Dark and Luminous Currents. The occurrence of Si<sub>3</sub>N<sub>4</sub> layer at the interface of AlN and Si has been witnessed and extensively studied by the electrical diagnostic approaches to identify a crucial role of the charges, which may directly affect the properties and operation of whole AlN/Si stack. Optical measurements been performed to evaluate the performance of Si<sub>3</sub>N<sub>4</sub> layer formation at the AIN and Silicon interface. Furthermore, the defect levels and their respective qualitative as well as quantitative analysis near the valence and conduction band edges of AlN is also reported. Multi-bias and switched voltage (positive/negative) routines at different active areas of subject AlN device matrix for their potential usage in Deep ultra-violet (DUV) and related photonic application. Another hierarchy of Metal-Semiconductor-Metal (MSM) metrics onto the previously fabricated AlN structure is deployed and adopted five different circuit schemes. Among all circuit sequences, one has provided best optimum circuit window for proper UV detection circuitry. Finally, the subject AlN lattice is implanted with silicon atoms of energy and fluence of 800keV and ~10<sup>+14</sup>cm<sup>-2</sup> respectively. A responsivity of light gain of more than unity was observed for UV as well as the visible light spectrum. Hence the resulting device was found good for both UV and visible light spectrum.

# **Table of Contents**

Dedications	iv
List of Publications	V
Abstract	vi
List of Figures	х
List of Tables	xv
List of Abbreviations	xvi
Chapter 1 Introduction	1
1.1 Introduction	
1.2 UV Basics	3
1.3 UV generation and detection.	4
1.3.1 UV Detectors	4
1.3.2 Photoconductive detectors	5
1.3.3 Schottky detectors	6
1.3.4 P-N & P-I-N junction detectors	6
1.3.5 MSM Detectors	6
1.3.6 Non-III-V matrix for UV/DUV applications.	7
1.3.6.1 Metal Oxides	7
1.3.6.2 Graphene	7
1.3.6.3 Silicon Carbide	8
1.3.7 III-Nitride semiconductors Matrix choice for proficient	8
optoelectronics	
1.3.7.1 Gallium Nitride	8
1.3.7.2 Aluminum Nitride	
1.4 Problem Statement.	9
1.5 Significance of Research.	10
1.6 Thesis Outline	10
Charles O Daylor and When	
Chapter 2 Background Theory	12
2.1 Electromagnetic Spectrum	12
2.1.1 Gamma Rays.	
2.1.2 X-Rays	14
2.1.3 Ultraviolet	15
2.1.4 Visible Light	16
2.1.5 Infrared.	16
2.1.6 Microwaves	17
2.1.7 Radio Waves	17
2.2 Photo-Voltaic Effects vs Photo-Electric effects	18
2.3 Photodetectors and Photo Diodes	20

2.4	Principle of Photodetection	21	
	2.4.1 Photovoltaic Detection		
	2.4.2 Photoconductive Detection	22	
2.5	Types of Photo-detectors	23	
	2.5.1 PN Photo-diode.	24	
	2.5.2 PIN Photo-diode.	24	
	25.3 Avalanche Photodiode	25	
	2.5.4 MSM Photodetectors	27	
2.6	Summary	28	
Chap	oter 3 Literature Review	28	
3.1	Introduction	28	
3.2	Summary	46	
Chap	ter 4 Fabrication and Characterization Techniques	44	
4.1	Fabrication Techniques	44	
4.2	Epitaxial Growth	44	
4.3	4.3 Types of Epitaxy		
4.3.1 Molecular Beam Epitaxy 4		45	
	4.3.2 Microchannel Epitaxy	46	
	4.3.3 Hydride Vapor Phase Epitaxy	47	
4.4	Physical Vapor Deposition	49	
4.5	- Spin Coating	50	
4.6	Characterization techniques	52	
	4.6.1 Current Voltage analysis	52	
	4.6.2 Capacitance-Voltage Analysis	52	
	4.6.3 Transient of Photo Voltage	53	
	4.6.4 Kinetics of Photo and Dark Current	53	
	4.6.5 Rectification Ratio	54	
	4.6.6 Spectroscopic Elipsometry	54	
	4.6.7 Scanning Electron Microscopy	56	
	4.6.8 Electron Dispersive X-Ray Analysis	58	
	4.6.9 Charge deep level transient spectroscopy	58	
4.7	Summary	63	

Cha	pter 5 Results and Discussions	66
5.1	Fabrication and Characterization of AlN over Silicon Wafer	66
	5.1.1 Fabrication of AlN over n-Silicon	67
	5.1.2 Characterization of deposited ALN	69
	5.1.2.1 Current Voltage Characterization	70
	5.1.2.2 Capacitance-Voltage Characterization	74
	5.1.2.3 Charge Deep Level Transient Spectroscopy of AlN/Si	76
	5.1.2.4 Transient of Photo-voltage of AIN/Si stack	81
	5.1.2.5 Kinetics of Dark and Photo Current on AlN/Si stack.	83
	5.1.2.6 Spectroscopic Elipsometry on AlN/Si stack	86
5.2	Development of MSM on AlN/Si for UV Sensing	89
	5.2.1 Fabrication of MSM on AIN/Si	91
	5.2.2 Characterization of MSM Structure	91
	5.2.2.1 Current-Voltage Characterization of MSM Structure	93
	5.2.2.2 Kinetics of Dark and Photo-Current of MSM Structure	97
	5.2.2.3 QDLTS analysis of the MSM structure	107
5.3	Ion Implantation of Silicon and Development of MSM On AlN/Si	118
	5.3.1 Development of MSM structure on the Silicon implanted region.	119
	5.3.2 Characterization of Silicon implanted AIN/Si structure	121
	5.3.2.1 Current-Voltage characterization of Silicon implanted AlN	
	structure	121
	5.3.2.2 QDLTS of Silicon implanted AlN/Si structure	
	5.3.2.3 TPV of Silicon Implanted AIN/Si Structure	125
	5.3.2.4 Kinetic of Dark and light current of Si implanted AlN/Si structu	127
5.4	Comparison with reported literature	138
Char	pter 6 Conclusion and Future Work	141
6.1	Conclusion	141
6.2	Future Work	145
Refe	erences	146

# List of Figures

Figure. 1.1: Solar Radiation Spectrum	1
Figure. 1.2: Potential Applications of DUV LEDs and LDs	2
Figure. 1.3: Spectrum of UV light	3
Figure. 1.4: Classification of UV detectors	4
Figure. 1.5: Schematic structure of different types of UV detectors	5
Figure. 1.6: A photoconductive detector symmetrically pumped by the optical pump,	
b a photoconductive detector asymmetrically pumped by the optical pump. Inset	
shows the equivalent circuit model of both symmetrically pumped and	l
asymmetrically pumped photoconductive detectors	
	1
	5
Figure 1.7: Schottky Diode Detector	6
1-B-10-1111 Selection 2-10-10-10-10-10-10-10-10-10-10-10-10-10-	*
Figure 2.1: Comparison of wavelength, frequency and energy for the	
electromagnetic spectrum.	
alasa amagnata apada atti	12
Figure 2.2: A schematic of SAS-2 gamma rays, an experiment which was flown in	<del>  `~</del>
1972-73	13
1972-73	14
2.5a. 2 most of 1 obtains supriso accommina a ray	17
Figure 2.4: Milestone events in the development of UV light sources in water and	
surface disinfection	15
Figure, 2.5: Visible light spectrum.	16
Figure. 2.6: A landscape seen at night time in the infrared spectrum	16
Figure. 2.7: Inside a microwave oven	17
Figure. 2.8: Radio Transmission.	18
Figure. 2.9: Photovoltaic effect.	19
Figure.2.10: Photoelectric effect.	19
Fig. 2.11: Basic principle of Photovoltaic detection	21
Figure. 2.12: Photoconductive Mode	22
Figure. 2.13: Cross section of a P-N Junction Photodiode	23
Figure. 2.14: Cross section of a PIN Diode	24
Figure. 2.15: Cross Section of an Avalanche Photodetector.	25
Figure 2.16: Typical MSM detector.	27
Figure. 3.1: Schematic representation of optical model for SE analysis	30
Figure 3.1. Schematic representation of optical model for SE analysis	
Figure 3.2: Different categories of UV and their benefits	31
Figure. 3.3: A SiN based gas sensor PIC, manufactured by Lionix Intl	33
rigure. 3.4: Cross sectional aberration-corrected stem image of the fresh UVC-LED	
chip	34
Figure. 3.5: Schematic of (a) Vertical (b) lateral AIN LEDs grown on n-type SiC(001)	
substrate	35

Figure. 3.6: (a) The honeycomb structure of the 2D h-BN supercell B atoms shown in green N in gray (b) Calculated electronic band structure of the 2D h-Bn	26
supercell.  Figure. 3.7: Surface morphology of porous silicon carbide on Si substrate synthesized	36
<del>-</del>	
using UV assisted electrochemical anodization technique with different etching	
current densities (a) 5 (b) 10 and (c) 15 A/cm <sup>2</sup> for 10 mins	37
Figure. 3.8: The process diagram of AlN synthesis by arc discharge with assistance	
of direct nitridation	38
Figure. 3.9: The synthesis mechanism of high purity AlN by arc discharge with	
assistance of direct nitridation	38
Figure. 3.10: Representative DLTS spectrum of 6H-SiC exhibits the minority and	
majority carriers	39
Figure. 3.11: Fabrication schematic of the quantum dot (QD)-coated silicon(Si)	
photodiodes (SIPDs), featuring spraying and drying of nanocrystals QDs, and	
photograph of spray coating using an airbrush noozle	40
Fig. 3.12: Photographs of QD layers deposited on SIPD (a) quartz substrate (b) by	<u> </u>
spraying the drawing process wrt number of spray steps	40
Figure. 3.13: Schematic diagram showing (a) preparation of BN/GO composite layer	
on Sio <sub>2</sub> /Si substrate and experimental setup (b) I-V and (c) temporal measurement	41
Figure. 3.14: Measured and simulated DLTS spectra of the ZnO: As/n-GaN diode (a)	
for lock in frequency of 20Hz (b) 50Hz	42
Figure. 3.15: SEM of the fracture surfaces for AlN ceramics	43
Figure. 3.16: Device Fabrication and cleaning process.	44
Figure. 3.17: Q-DLTS approach of charge and discharge events for localized traps of	
CdTe lattice	44
Figure. 4.1: Schematic Drawing of a generic MBE system	47
Figure. 4.2: Schematic drawing of a typical MBE effusion cell	47
Figure. 4.3: Epitaxy Stepwise.	49
Figure. 4.4: The concept of vertical HVPE reactor	51
Figure. 4.5: Physical vapor deposition	52
Figure. 4.6: General Mechanism of PVD	52
Figure. 4.7: Different stages of spin coating	53
Figure. 4.8: a. Typical IV circuit b. Typical IV curve	55
Figure 4.9: a. A CV curve b. Typical CV circuitry	56

Fig. 4.10: TPV and CE regimes	57
Fig. 4.11: Vacuum-Ultraviolet Photon Detection	58
Figure. 4.12: Spectroscopic Ellipsometry	59
Figure. 4.13: Scanning Electron Microscope	60
Figure. 4.14: Electron Dispersive X-Ray spectroscopy	61
Figure 5.1: Main hierarchy of Aluminum Nitride growth and characterization for	
UV sensing	64
Figure 5.2: Fabrication processes of AlN/Silicon substrate; (a) Silicon Wafer. (b) Cleaning protocols for Silicon Wafer, (c) Deposition of AlN on Silicon Wafer, (d) Cleaving of AlN/Silicon Wafer, (e) 2D-view of cleaved sample, (f) 3D-view of cleaved sample.	67
Figure 5.3: SEM image of the AIN layers on Silicon substrate	67
Figure 5.4: Physical schemes of electrical characterizations; (a) Top surface, (b) Top-	
Bottom, (c) Etched Surface and (d) Rare side (backside) Silicon	69
Figure 5.5: Current-Voltage characteristics of AlN stack	70
Figure 5.6: Temperature wise current-voltage analysis; (a) Silicon side Temperature	
wise IV analysis, (b) Arrhenius analysis of all said cases	72
Figure 5.7: Capacitance voltage analysis of AIN stack	73
Figure 5.8: Time based voltage-charge (V-Q) diagram for Q-DLTS	75
Figure 5.9: Q-DLTS analysis of AlN-Si stack	77
Figure 5.10: Q-DLTS analysis, (a) Q-DLTS of Top AlN surface under different	78
temperatures, (b) Arrhenius analysis of AlN/Si stacks	79
Figure 5.11: Band picture of AlN stack	
Figure 5.12: TPV measurements of AlN stack	81
Figure 5.13: Kinetics of Current under ground biased Dark and luminous condition of AlN stack	83
Figure 5.14: Kinetics of Current under photovoltaic Dark and luminous condition of	0.4
AlN stack.	84
Figure 5.15: Layer wise model of the layers associated to the device under test  Figure 5.16: Dielectric constants of AlN, Si <sub>3</sub> N <sub>4</sub> and Si stack	85 86
Figure 5.17: Extinction coefficients of AlN, Si3N4 and Si stack	87
Figure 5.18: Cross-sectional view of AlN/Silicon and interdigitated electrode	
structure	90
Figure 5.19: Current-Voltage analysis of AlN/Silicon structure under dark and UV-	
Mode	92

Figure 5.20: (a-j) Current-voltage analysis of AIN/Si based stated for different	
biasing cases(C1-C5) under dark and UV conditions (K) Arrhenius analysis based	94
on current voltage analysis	
Figure 5.21: Kinetics of dark and UV current for C1 case; (a) 300K temperature, (b)	<del> </del>
310K temperature, (c) 320K temperature, (d) 330K temperature, (e) 340K	
	97
temperature	<del></del>
310K temperature, (c) 320K temperature, (d) 330K temperature, (e) 340K	
temperature	98
Figure 5.23: Kinetics of dark and UV current for C3 case; (a) 300K temperature, (b)	70
310K temperature, (c) 320K temperature, (d) 330K temperature, (e) 340K	
temperature.	99
Figure 5.24: Kinetics of dark and UV current for C4 case; (a) 300K temperature, (b)	
310K temperature, (c) 320K temperature, (d) 330K temperature, (e) 340K	
temperature.	100
Figure 5.25: Kinetics of dark and UV current for C5 case; (a) 300K temperature, (b)	100
310K temperature, (c) 320K temperature, (d) 330K temperature, (e) 340K	
temperature	101
Figure 5.26: Kinetics of dark and UV current particularly for 0-Volts under 300-340K	101
temperature; (a) I-t for C1 case at 0-Volts under 300-340K temperature, (b) ) I-t for	
C2 case at 0-Volts under 300-340K temperature, (c) 1-t for C3 case at 0-Volts under	
300-340K temperature, (d) I-t for C4 case at 0-Volts under 300-340K temperature,	
(e) I-t for C5 case at 0-Volts under 300-340K temperature, (f) I-t for C1, C2, C3, C4	
and C5 cases at 0-Volts under only Room temperature (300K)	102
(2001	102
Figure 5.27: Numerical Gain of under 300K temperature	103
Figure 5.28: Numerical Gain of under 310K temperature	104
Figure 5.29: Numerical Gain of under 320K temperature	105
Figure 5.30: Numerical Gain of under 330K temperature	106
Figure 5.31: Time based voltage-charge (V-Q) diagram for Q-DLTS	107
Figure 5.32: Q-DLTS analysis of AlN-Si stack against each boundary condition/configuration.	107
condition/configuration	
from 10-100mV (a) 300K temperature, (b) 310K temperature, (c) 320K temperature,	
(d) 330K temperature, (e) 340K temperature.	110
Figure 5.34: Q-DLTS analysis of Case C2 under multiple bias sequences ranging	
from 10-100mV (a) 300K temperature, (b) 310K temperature, (c) 320K temperature,	
(d) 330K temperature, (e) 340K temperature	111
Figure 5.35: Q-DLTS analysis of Case C3 under multiple bias sequences ranging	
from 10-100mV (a) 300K temperature, (b) 310K temperature, (c) 320K temperature,	
(d) 330K temperature, (e) 340K temperature	112

from 10-100mV, (a) 310K temperature, (b) 320K temperature, (c) 330K temperature, (d) 340K temperature
Figure 5.37: Q-DLTS analysis of Case C5 under multiple bias sequences ranging from 10-100mV, (a) 300K temperature, (b) 310K temperature, (c) 320K temperature, (d) 330K temperature, (e) 340K temperature
from 10-100mV, (a) 300K temperature, (b) 310K temperature, (c) 320K temperature, (d) 330K temperature, (e) 340K temperature
(d) 330K temperature, (e) 340K temperature
Figure 5.38: Q-DLTS analysis, (a) Q-DLTS of 40mV-Dark-C2, (b) Arrhenius analysis of all detectable cases
analysis of all detectable cases
Figure 5.39: Atomic and disorder profile of silicon atoms within the AlN/Silicon 118
structure.
Figure 5.40: Development of MSM structure on implanted AlN region, (a)
AlN/Silicon structure, (b) Silicon ion implantation using peletron accelerator, (c)
Masking procedure using Photo-Lithography and (d) development of MSM structure 119
using Physical Vapor Deposition (PVD)
Figure 5.41: Current-Voltage and Arrhenius analysis of Silicon implanted 120
AIN/Silicon structure
Figure 5.42: Current-Voltage and Arrhenius analysis of Silicon implanted 122
AlN/Silicon structure
Figure 5.43: Charge Deep Level Transient Spectroscopy (Q-DLTS) at different
temperature of Silicon implanted AlN/Silicon structure, (a) Q-DLTS spectra at 1V.
(b) Q-DLTS spectra at 2V, (c) Q-DLTS spectra at 3V, (d) Q-DLTS spectra at 4V, (e) 123
Q-DLTS based Arrhenius analysis, (f) Energy band picture at different drift
potentials
Figure 5.44: Transient of Photo-voltage (TPV) of Silicon Implanted AlN/Silicon 125
Structure
Figure 5.45: : (a-z) Kinetics of Dark and visible and UV light sequences through
silicon implanted region at AIN/Silicon structure under 0mV and 10-300mV applied 135
drift potential (i-xiv) from 400-1000mV
Figure 5.46: Gain magnitudes for Visible and UV light on silicon implanted AlN   137
structure

# List of Tables

Table 2.1: Summary of different devices discussed in Chapter 2	28
Table 5.1: Trap analysis of AlN-Si Stack	
Table 5.2: Kinetics of Dark and Photocurrent of AIN stack	
Table 5.3: Geometrical and instrumental approach associated against each bias condition	91
Table 5.4: Activation Energies associated with each case	95
Table 5.5: Q-DLTS based Arrhenius analysis of successfully observed trap parameters-	116
Table 5.6: Silicon Ion implantation on AlN/Si	118
Table 5.7: Dark, visible light and UV currents for Gain measurements ——————	136

# List of Abbreviation

Abbreviations	
AlN	Aluminium Nitride
QDLTS	Charge Deep Level Transient
	Spectroscopy
UV	Ultraviolet
DUV	Deep Ultraviolet
I-V	Current Voltage
C-V	Capacitance Voltage
SEM	Scanning Electron Microscopy
LED	Light Emitting Diode
EDX	Electron-Dispersive X-Ray Analysis
XRD	X-Ray Diffraction
MSM	Metal Semiconductor Metal
APD	Avalanche Photodiode
TPV	Transient of Photo-voltage
SE	Spectroscopic Ellipsometry
PVD	Physical Vapor deposition
HVPE	Hydride Vapor Phase Epitaxy
MCE	Micro-Channel Epitaxy
ALE	Atomic Layer Epitaxy
UHV	Ultra High Viscosity
MCE	Molecular Beam Epitaxy
ELO	Epitaxial Layer overgrowth
SAE	Selective Area Epitaxy
ev	Electron Volt
EM	Electromagnetic
PN	P-type N-type
CD	Compact Disc
DVD	Digitl versatile disc

MSM	Metal-Semiconductor-Metal
SOI	Silicon on Insulator
CMOS	Complementary metal oxide
	semiconductor
PIC	Peripheral interface controller
MQW	Multi Quantum Well
DLTS	Deep Level Transient Spectroscopy
CdTe	Cadmium Telluride
V <sub>oc</sub>	Open Circuit Voltage
SAG	Selective Area Growth
MOCVD	Metal Organic chemical Vapor deposition
WPE	Wall plug efficiency
EQE	External Quantum Efficiency
IPA	Isopropyl Alcohol
RMS	Root Mean Square
C1	Case 1
C2	Case 2
C3	Case 3
C4	Case 4
C5	Case 5



# Chapter 1

# Introduction

## 1.1 Introduction

UV radiation covers only 10% of the total solar radiation spectrum however it is regarded as most important component of solar radiations. It has played a vital role in the survival and development of mankind. UV light provides many benefits to human health in the form of synthesis of Vitamin D, killing germs, treating, or preventing rickets etc. However, there are health risks as well due to excessive exposure of UV radiation which can causes diseases such as cataracts and skin cancer and it can also promote aging process. Figure 1.1 shows the solar radiation spectrum [1].

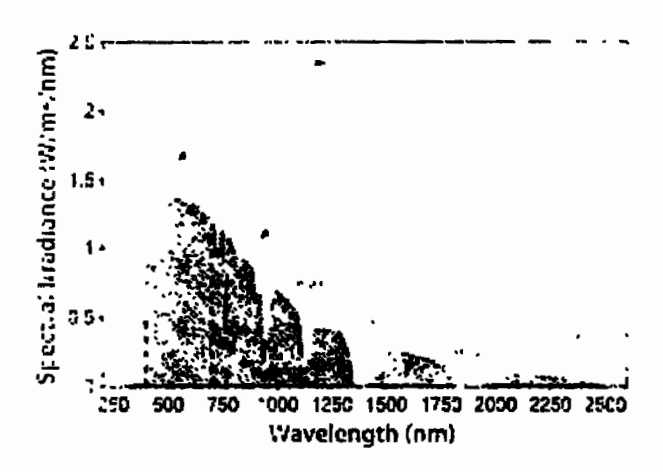


Figure. 1.1: Solar Radiation Spectrum [1]

Apart from effects on human health, UV radiations also affects crops and buildings. Stratosphere ozone absorbs almost all of the UV radiation, however due to man induced environmental pollution the concentration of stratospheric ozone is decreasing and currently there is a hole in ozone layer as huge as Antarctica. Most alarming is the fact that for every 1% decrease in volume of ozone layer, will increase 2% in UV radiations at ground level,

leading to an increase of "3% in the incident rate of skin cancer". Thus, recently UV photodetection has received increased attention of research community [2 3].

Ultraviolent systems are rapidly taking over other technologies specially in water treatment applications, as these radiations have the ability to remove broad spectrum microbial agents with reduced disinfection from by-product formation. In this scenario, they provide an alternative to chemical disinfectants which are also harmful for human health. UV light in proper intensity can remove micro-organisms by damaging their DNA molecules and restrict them from reproducing [4].

Solid state UV LEDs have number of uses in biomedical industry such as purifying air and water, treating skin diseases, disinfecting surfaces, for industrial curing, printing, forensic investigations and forgery detection [5]. Pictorial representation of UV application in Health Care sector is shown in Figure 1.2:

Pollutant Materials

| Figh-Speed Dissociation of Pollutant Materials
| Figh-Speed Dissociation of Pollutant Materials
| Figh-Speed Dissociation of Pollutant Materials
| Figh-Speed Dissociation of Pollutant Materials
| Figh-Speed Dissociation of Pollutant Materials
| Figh-Speed Dissociation of Pollutant Materials
| Figh-Speed Dissociation of Pollutant Materials
| Figh-Speed Dissociation of Pollutant Materials
| Figh-Speed Dissociation of Pollutant Materials
| Figh-Speed Dissociation of Pollutant Materials
| Figh-Speed Dissociation of Pollutant Materials
| Figh-Speed Dissociation of Pollutant Materials
| Figh-Speed Dissociation of Pollutant Materials
| Figh-Speed Dissociation of Pollutant Materials
| Figh-Speed Dissociation of Pollutant Materials
| Figh-Speed Dissociation of Pollutant Materials
| Figh-Speed Dissociation of Pollutant Materials
| Figh-Speed Dissociation of Pollutant Materials
| Figh-Speed Dissociation of Pollutant Materials
| Figh-Speed Dissociation of Pollutant Materials
| Figh-Speed Dissociation of Pollutant Materials
| Figh-Speed Dissociation of Pollutant Materials
| Figh-Speed Dissociation of Pollutant Materials
| Figh-Speed Dissociation of Pollutant Materials
| Figh-Speed Dissociation of Pollutant Materials
| Figh-Speed Dissociation of Pollutant Materials
| Figh-Speed Dissociation of Pollutant Materials
| Figh-Speed Dissociation of Pollutant Materials
| Figh-Speed Dissociation of Pollutant Materials
| Figh-Speed Dissociation of Pollutant Materials
| Figh-Speed Dissociation of Pollutant Materials
| Figh-Speed Dissociation of Pollutant Materials
| Figh-Speed Dissociation of Pollutant Materials
| Figh-Speed Dissociation of Pollutant Materials
| Figh-Speed Dissociation of Pollutant Materials
| Figh-Speed Dissociation of Pollutant Materials
| Figh-Speed Dissociation of Pollutant Materials
| Figh-Speed Dissociation of Pollutant Materials
| Figh-Speed Dissociation of Pollutant Materials
| Figh-Speed Dissociation of Pollutant Materials
| Figh-Speed Dissociation of Pollutant Materials
| Figh-Speed Dis

Figure. 1.2: Potential Applications of DUV LEDs and LDs [5]

UV LEDs play an important role particularly in water purifying applications by providing benefits such as:

- UV LEDs are environment friendly as they do not contain any harmful material
- UV LEDs are more tolerant to disturbances during transit and handling

- No start-up time needed, since UV LEDs turn on instantly
- UV LEDs utilize lower voltages resulting in lower power consumption
- Lower power consumption would provide higher energy efficiency
- UV LEDs can be utilized in applications where there is a need to switch lights at high frequency

Due to above features, UV LEDs have longer service life and need less replacement and better advantages over other technologies counterparts.

# 1.2 UV Basics

UV light represents the electromagnetic radiation having a wavelength range of 10-400 nm [6]. A pictorial view of it is presented in Figure 1.3. UV radiations can be classified in to following wavelength regimes:

- I. "UVA (400-315 nm)"
- II. "UVB (315-280 nm)"
- III. "UVC (280-200 nm)"
- IV. "VUV (200-10 nm)"

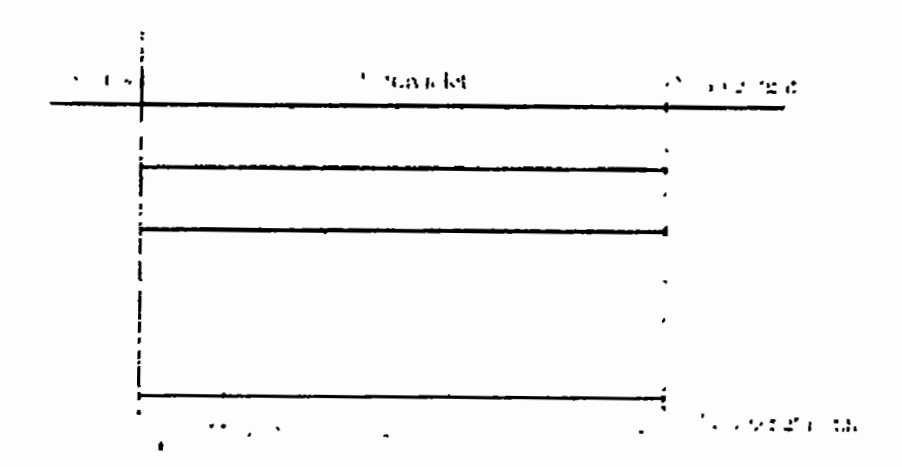


Figure. 1.3: Spectrum of UV light [6]

## 1.3 UV Generation and detection

Wide bandgap semiconductors exhibit properties like low permittivity, high break down electric fields, good thermal conductivity, high electron saturation rates and radiation resistance, which makes them highly suitable to operate in high temperatures, at a high frequency and power withstanding highly radiation active environments. As an example, III-Nitrides provides a coverage from infrared to ultraviolet band since their energy band gap can vary from 0.77 eV (InN) to 6.28 eV (AIN). Mostly blue, green and other short wavelength light emitting diodes, semiconductor lasers and UV detector devices are fabricated using Wide band gap semiconductors in the fields of optoelectronics and microelectronics [7 8 9].

#### 1.3.1 UV Detectors

The classification of UV detectors is best highlighted by Figure 1.4:

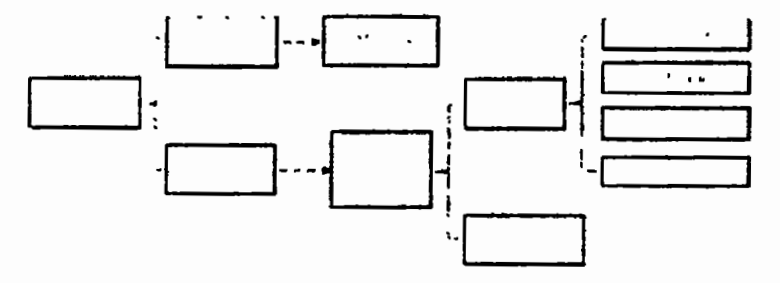


Figure. 1.4: Classification of UV detectors [9]

UV detectors are divided into two categories with respect to its special modes of operation i.e. photoconductive UV detectors and photovoltaic UV detectors [9]. Schematic description of them is given in Figure 1.5.

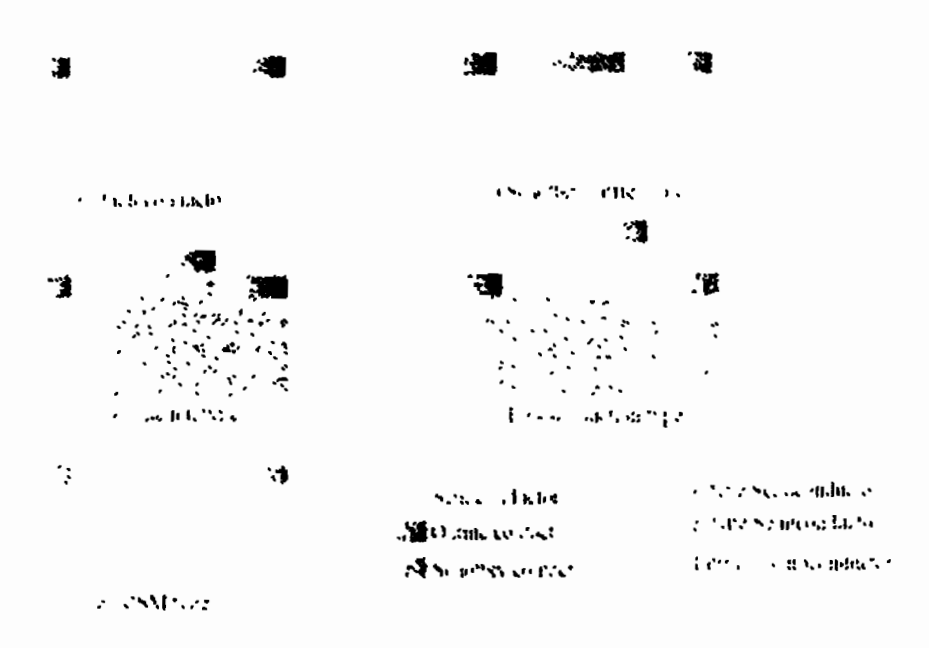


Figure. 1.5: Schematic structure of different types of UV detectors [9]

#### 1.3.2 Photoconductive Detectors

Photoconductive detectors work on the principle of photoconductivity where in the conductivity of the material varies with incidence of light [10]. Photoconductive UV detectors have the advantage of having simple structure, easy process control and high internal gain however their disadvantages are slow response speed and large dark current [10]. A photoconductive detector and its equivalent circuit is shown in Figure 1.6.

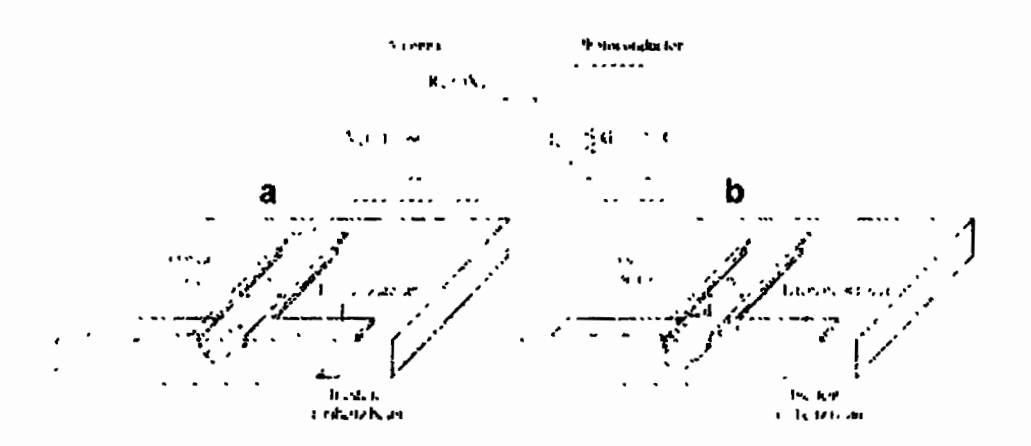


Figure. 1.6: A photoconductive detector symmetrically pumped by the optical pump, b a photoconductive detector asymmetrically pumped by the optical pump. Inset shows the equivalent circuit model of both symmetrically pumped and asymmetrically pumped photoconductive detectors [11]

#### 1.3.3 Schottky Detectors

Schottky detector is simply a metal-semiconductor interface. The metal/semiconductor junctions behave as rectifier. Schottky detector behave much better than detectors in terms of high quantum efficiency, high response speed, low dark current, high UV/visible contrast, and possible zero-bias operation. Schottky detectors are mostly suitable for broadband photo-detection, since their photo response is flat [12]. Figure 1.7 shows a Schottky diode detector and its symbol.

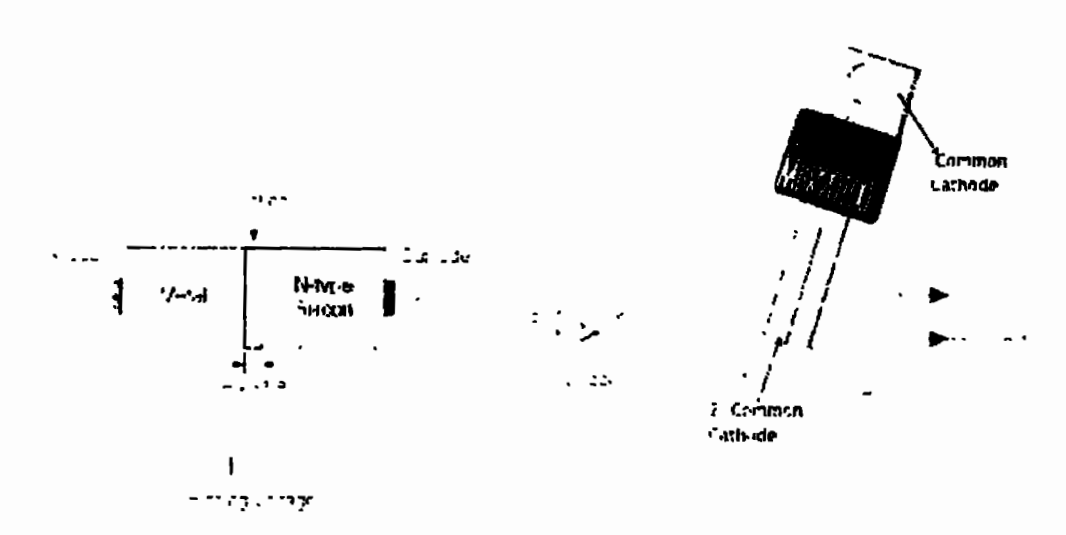


Figure 1.7: Schottky Diode Detector [12]

# 1.3.4 p-n and p-i-n Junction Detectors

In p-n junction photo detector, incident photon creates an electron-hole pair if the incident light energy is greater than bandgap. Carriers which are under diffusion length would be swept to other side under the action of field. In p-i-n photodetectors normal operation occurs at zero bias or reverse bias, so that sensitivity of detector is improved [12].

#### 1.3.5 MSM Detectors

The main features of MSM photodetectors are low dark currents, the high resistivity, a single dopant active layer, high speed, linear optical power, an extremely low parasitic capacitance and low noise. MSM detectors are mostly suited for military and space applications [12]

#### 1.3.6 Non- III-V Material Matrix for UV/DUV Applications

UV detectors are normally described in terms of high performance, quantum efficiency, response speed, and signal-to-noise ratio. The inherent characteristics of the semiconductor material play an important role in describing the performance of a UV detector. The process of transformation of optical signals into electrical signals involves electron-hole pair generation, transportation and recombination in the semiconductor material. A summary of subject materials is presented as under:

#### 1.3.6.1 Metal Oxides

Due to easy availability of Metal oxide materials, all the current research efforts are directed towards their development. Nanoscale photodetectors have been extensively fabricated and utilizing 1D metal oxides [13]. ZnO belongs to II-VI group of semiconductors, properties like strong radiation hardness, high chemical stability and its abundance make it an attractive material. ZnO has a band gap of  $Eg=3.365\pm0.005eV$  under normal room temperature and atmospheric pressure. ZnO is an excellent material for fabrication of photoelectric [14] and photonics devices working in the UV range [15]. Chemical stability, non-toxicity and thermal stability of Titanium dioxide (TiO<sub>2</sub>) makes it an attractive material for application in UV detection [16]. It also demonstrates a wide band gap of "3.0 to 3.2 eV". TiO<sub>2</sub> films [16], TiO<sub>2</sub> nanorods, and TiO<sub>2</sub> nanowires have been utilized for development of UV detectors and shown excellent results [17]. Tin(IV) dioxide (SnO<sub>2</sub>) is a compound semiconductor having wide bandgap of around 3.6 eV [17]. SnO<sub>2</sub> due to optical properties and chemical stability is another useful material that can be used for UV photodetectors [17]. Nanostructures of SnO<sub>2</sub> have been developed as nano-whiskers [18], nano-belts [19], nano-rods [20] and nano-wires [13-21].

#### 1.3.6.2 Graphene

Graphene has shown great potential in optoelectronic devices of its unique electrical and mechanical properties. Many research groups have developed UV photodetectors based on

graphene, which showed excellent properties as desired in optical applications [22 23].

#### 1.3.6.3 Silicon Carbide (SiC)

SiC demonstrates a high breakdown electric field, high thermal conductivity and excellent chemical stability. Owning to these physical and electrical properties it can be utilized in extremely harsh environment applications for visible-blind UV photodetectors. SiC nanowires have been utilized as Schottky contacts, p-n junctions and ohmic contact. They have demonstrated excellent photocurrent I-V characteristics, photo response and time response [24].

#### 1.3.7 III-Nitride Semiconductors: Matrix Choice for Proficient Optoelectronics

III-V compound semiconductors are formed from two, ternary and quaternary alloys of these compounds such as GaN, AIN, AlGaN, AlGaAsP etc. III-V semiconductors are direct band gap materials with a wurtzite crystal structure. III-V materials band gap can be continuously changed by varying the chemical composition of alloy. This feature provides a unique advantage to these materials over others in optical applications. However major hurdle in their use in UV electronics is poor crystal growth which results in high density of dislocations and other structural defects [25 26 27].

#### 1.3.7.1 Gallium Nitride (GaN)

GaN is the most promising material of III-V family. GaN nanowire-based UV photodetectors have shown considerable improvements in dark current and response time [27]. The results of opto-electrical characterization clearly reflects better response to irradiation with UV light. GaN nanowire based MSM Schottky contact device demonstrated excellent performance in terms of better sensitivity and external quantum efficiency [28 29].

#### 1.3.7.2 Aluminum Nitride (AIN)

AIN provides the most widest opportunities among III-V semiconductor materials due to its

promising bandgap. It's an ideal material for new generation of Deep UV and UV photoelectronic devices. AlN nanowires were grown utilizing chemical vapor deposition shown fast response speed and high photocurrent response. Also utilizing physical vapor deposition high quality AlN micro/nanowires have been grown. The AlN micro/nanowire VUV photodetectors have much better photo current and response speed characteristics [30 31 32].

#### 1.4 Problem Statement

"AIN electronics" originating from III-nitride semiconductor system is an area of emerging interest for future generation of high-power electronics and optoelectronics devices including the RF assisted filters, HEMTs and NEMS applications. This becomes particularly important when applications are targeted for "Deep Ultra-Violet" regime of performance. With literature survey and gap analysis in hand; it has been learnt that the quality and composition of substrate in making such devices and systems play a significant role. Thus, several variations both in terms of substrate selection and fabrication strategies are being researched. Si-based AlN substrates for "Deep Ultra-violet" device manufacturing has started gaining attention with an effort to understand the underlying physical phenomenon to address the substrate effects, junction dynamics and interface. Our problem is focused to provide a "technology-ready" level AlN/Si substrate matrix for Deep UV devices and systems with a detailed assessment made to optimize the "output performance" characteristics. This would require attending the problems of formation of parasitic channel conduction pathway at the nitride/Si interface affecting the efficiency and output power, and little-known physical dynamics of defects at the interfaces responsible for substrate losses, which may otherwise be undesirable for proficient Deep UV applications.

As discussed in the introduction part of this proposals Deep Ultraviolet devices have numerous applications in the fields of optoelectronics, photonics, water purification, chemical detection etc. but the major challenge is its output efficiency. The UV output power for many

applications like fingerprint identification, medical light therapy, water sterilization and polymer curing at less than 365 nm is only about 5% to 8% of input power. The efficiency increases to 15% at wavelength of 385nm and lower. If the output efficiency is improved maximum UV band will be utilized. This challenge is being addressed in the current research by addressing various bottlenecks currently present on substrate level. The work is significant in order to support providing a technology ready solution to the DUV manufacturing industry with a detailed assessment of substrate effects on the output performance cycle of such devices.

## 1.5 Significance of Research

As discussed in the introduction part of this proposals Deep Ultraviolet devices have numerous applications in the fields of optoelectronics, photonics, water purification, chemical detection etc. but the major challenge is its output efficiency. The UV output power for many applications like fingerprint identification, medical light therapy, water sterilization and polymer curing at less than 365 nm is only about 5% to 8% of input power. The efficiency increases to 15% at wavelength of 385nm and lower. If the output efficiency is improved maximum UV band will be utilized. This challenge is being addressed in the current research by addressing various bottlenecks currently present on substrate level. The work is significant in order to support providing a technology ready solution to the DUV manufacturing industry with a detailed assessment of substrate effects on the output performance cycle of such devices.

# 1.6 Thesis outline

Chapter 1 describes introductory overview of the global paradiam of the Aluminium Nitride based Photo Detection.

Chapter 2 describes the background theory.

Chapter 3 provides the recent findings published in the literature with an assessment on the key results and gaps, on the Aluminium Nitride (AIN).

Chapter 4 describes the experimental techniques used in our work in terms of the design, fabrication and characterization.

Chapter 5 describes each aspect of our work comprising of experiments, results and discussion on the findings of the study.

Chapter 6 describes the summary of the findings as well as in sight about the future work.

# Chapter 2

# **Background Theory**

# 2.1 Electro Magnetic (EM) Spectrum

The range of all types of electromagnetic (EM) radiation is called electromagnetic spectrum. The energy that travels and spreads out along the way is called radiation. The EM radiations or the EM spectrum is a part of our everyday life, The visible light from our household lamps or the radio waves caught and transmitted by our transistor or FM radio, all belong to the EM spectrum. Microwave, infrared, ultraviolet, X-rays and gamma rays are other forms of EM radiations that make up the EM spectrum [33].

Our knowledge about the EM spectrum is in fact more than we realize. Figure 2.1 shows the different types and the range of the EM spectrum.

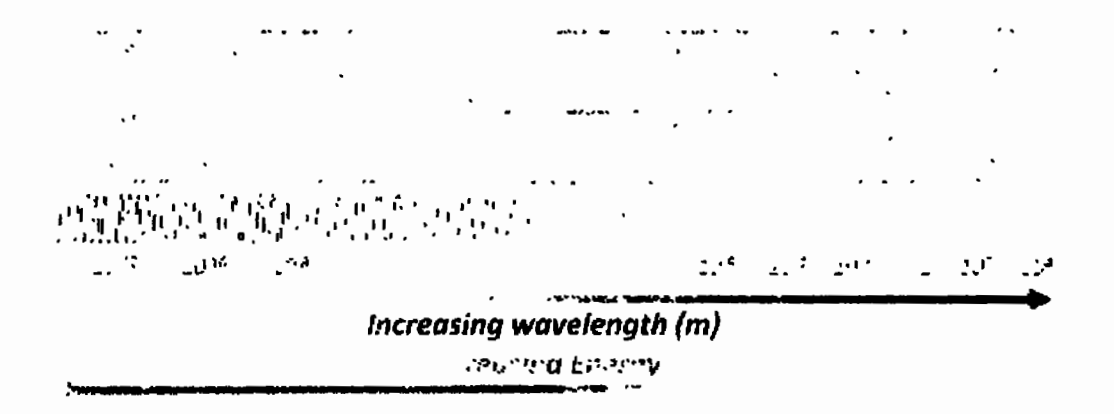


Figure 2.1: Comparison of wavelength, frequency and energy for the electromagnetic spectrum [34]

There is a range of frequencies of different rays, that are characterised in the electromagnetic spectrum, starting from the radio waves with lowest frequencies in the spectrum and the highest wavelengths to the gamma rays with the lowest wavelengths and highest corresponding frequencies. All the electromagnetic rays are same in the sense that they are made of same kind

of vibrations varying in their frequencies and wave lengths [34]. Let's discuss different categorisations of rays in descending order with respect to their frequencies.

#### 2.1.1 Gamma Rays

Gamma rays have the highest frequencies and the lowest corresponding wavelengths. Due to the ultra high frequencies, these rays carry high amount of energy and can pass through most of the materials with a relative ease. Only the materials like lead and concrete can stop these rays. Stars and some of the radioactive materials give off gamma rays [35].

Gamma rays have the property that they can kill living cells. That is the reason they are used to kill the cancerous cells. Sometime doctors can put slightly radioactive particles inside the body of the patient and scan them afterwards to get a picture of what is going on inside the body. The injected radioactive particles are called tracers. The same technique is used in industry when the tracers are introduced to pipes and machineries to know where the substances are going. Gamma rays can kill germs, so they are also sometimes used sterilize medical equipment. Prolonged and heavy exposure to gamma rays can cause variety of cancers like skin cancer etc [35]. A schematic of the SAS-2 gamma rays, an experiment that was performed back in 1972-73 is shown in Figure 2.2.

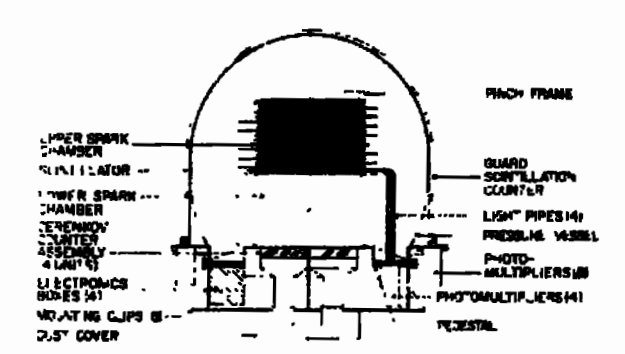


Figure 2.2: A schematic of SAS-2 gamma rays, an experiment which was flown in 1972-73 [36]

## 2.1.2 X-Rays

X-rays are high frequencies, that pass through most of the bodies [37]. Many stars and nebulas are the source of X-rays. X-rays are especially useful in the field of medicine [37]. X-rays are produced artificially by firing high energy electron on a target [37]. For medical purposes, X-rays are focused on a human body, these rays pass through the soft tissues easily but can not pass through the bones, consequently the image is transferred on the film [37]. Sometimes low energy X-rays are passed through the body to the get the image of soft tissues like brain [37]. Airport security also uses X-rays to see inside the bags full of luggage. On the downside, X-rays can cause severe cancers, If the exposure is for longer period, or the dose is too high [37]. That is why radiographers are required to stand behind a shield while x-raying their patients [37]. A patient under the X-ray tube is shown in Figure 2.3.



Figure 2.3: Anterior Posterior supine abdominal x-ray [38]

#### 2.1.3 Ultraviolet

Like the Gamma rays and the X-rays, Ultraviolet rays also lie in the invisible band and have very high frequencies [39]. They are further categorized into UV-A, B, and C according to their increasing frequencies and decreasing wavelengths [39]. Sun is the basic source of the ultraviolet light, although many of the rays are blocked by the ozone layer, but it can also be received from the mercury UV lamps made for this purpose [39]. UV LEDs have also made it in to the market [39]. The benefits of UV include sun tanning, killing harmful bacteria. It has

an ability to destroy the DNA, therefore its application as a sterilizing agent has gained currency lately [39]. It can also be used for checking the currency notes and identifying the forged ones [39]. If one marks any of one's possession with the security marker pen, then it would be only visible when the UV light is shown on it [39]. UV light is also used for hardening of some of the dental filling [39]. A timeline of UV generation for a range of purposes is shown in Figure 2.4.

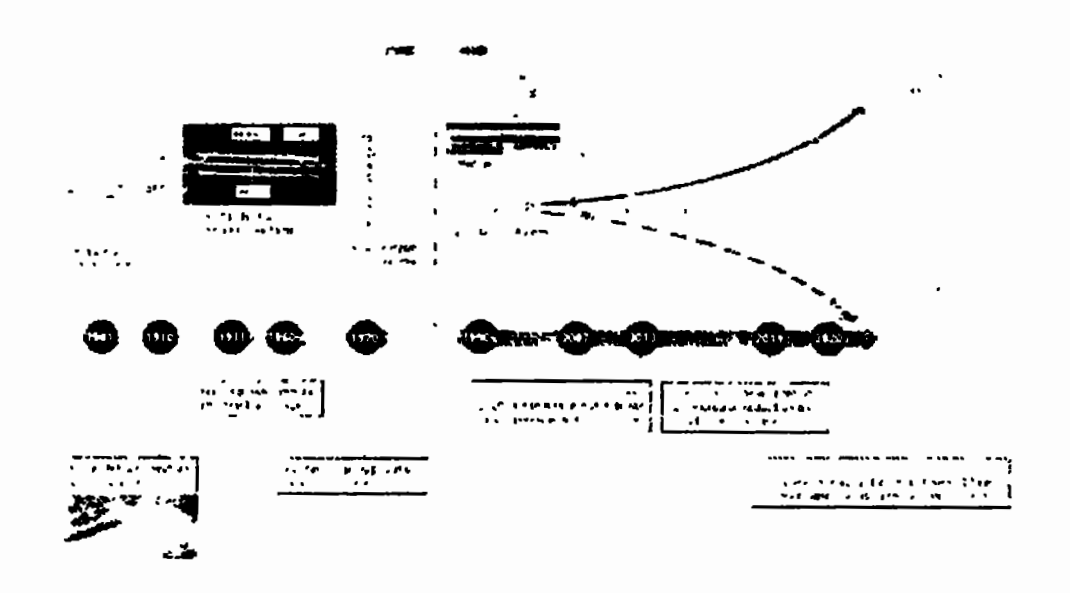


Figure 2.4: Milestone events in the development of UV light sources in water and surface disinfection [40]
Ultraviolet light can also cause skin cancer if the exposure is for longer duration or if the ozone layer is depleted from the area where the exposure occurs [41]. UV lights can also damage the retina of the eye [41].

## 2.1.4 Visible Light

Visible light is the spectrum of light visible to the naked eye [42]. Anything hot enough to glow produces this light. Sun, fire, different bulb, and LEDs are the source of this light [42]. When . white light passes through the spectrum, it disperses in to a spectrum of different colours [42].

Each colour has a frequency of its own [42]. The spectrum of the visible light in terms of wavelength is 380nm to 750nm as shown in Figure 2.5 [43].

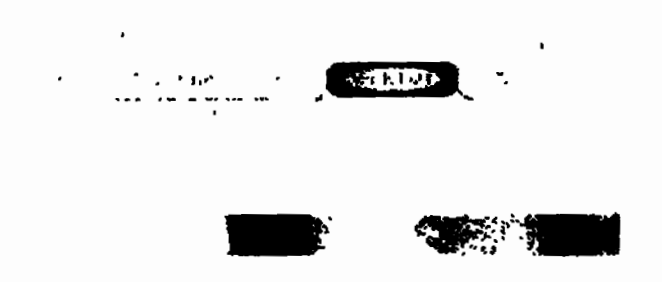


Figure. 2.5: Visible light spectrum [43]

Laser is a form of the visible light, which has been used in different ways in the daily life [44]. From the use of laser light for medical purposes to the laser jet printers [44].

#### 2.1.5 Infrared

Infrared are the rays just below the visible spectrum [45]. They have frequencies below the red light in the spectrum [45]. Infrared are given off by many bodies like animal and human, who have warmth in their bodies [45]. Infrared has many uses and benefits in the daily like remote controls, night time vision googles, burglar alarms, auto on off lights on the detection of any passer-by, all are the examples of the infrared applications [45]. Infrared can be used very efficiently for night time vision as shown in Figure 2.6.



Figure. 2.6: A landscape seen at night time in the infrared spectrum [46]

## 2.1.6 Microwaves

Microwaves are very high frequency waves given by some of the stars, the microwave oven and the mobile phones [47]. Their wavelength is normally a couple of centimetres. Microwaves cause vibrations in the water and fat molecules making them hot, hence they are used in microwave oven for cooking and food warming purposes [47]. Microwaves are also given off by the cell phones, that's why it is advised to keep them away especially while sleeping [47]. Microwave oven has a special application for cooking and warming of food as shown in Figure 2.7.



Figure. 2.7: Inside a microwave oven [48]

### 2.1.7 Radio Waves

Radio waves are used in radio transmission. Various kinds of radio waves depending on their frequencies are given by the different radio transmitters. They also come from some of the stars and during the thunderstorm causing noise in the radio transmission [49]. Radio waves are categorised as Medium waves (MW), Short waves (SW), Very High Frequency(VHF), and Ultra High Frequency (UHF) [49]. A schematic of the radio transmission transceiver is shown in Figure 2.8.

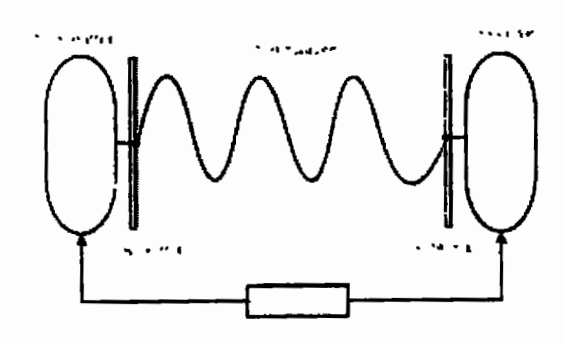


Figure. 2.8: Radio Transmission [49]

#### 2.2 Photo-Voltaic Effect vs Photo-Electric Effect

Photovoltaic Effect: A process that results in the generation of voltage and the resulting current in a photovoltaic cell on exposure to the sunlight is called photovoltaic effect [50]. It is this phenomenon that makes a solar panel useful [50]. Edmond Becquerel first discovered the photovoltaic effect in 1839 [50]. While doing an experiment on wet cells he observed that the voltage of the cell increased in the duration during which it silver plates are exposed to the sunlight [50].

The photovoltaic effect is normally observed in the solar cells [50]. The solar cell is composed of a p-n junction that is created by the respective combination of p-type and N-type material [50]. When the p-n junction is formed, an electric field is generated in the junction region as the electrons move to the positive p-side and the holes move towards the negative N-side [50]. Light is composed of packets of energy called photons [50]. If the incident light is of suitable energy the photon transfers the energy to an atom of the semiconducting material in the p-n junction [50]. The electrons in the material gets the energy, and get excited and jump in to the conduction band, leaving behind a hole [50]. Hence an electron-hole pair is formed. A schematic of the photovoltaic effect inside a solar cell is shown in Figure 2.9.

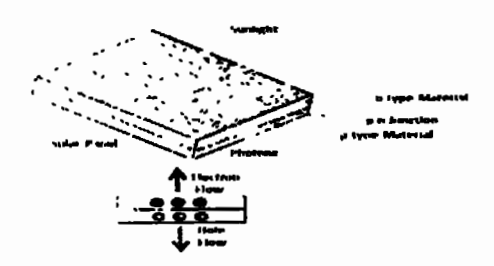


Figure. 2.9: Photovoltaic effect [51]

Normally the electrons are bonded within the lattice of the semiconductor and cannot move, but when they are in their excited state, they move to the conduction band and are free to move, and after the initial diffusion of electrons towards the P-side and the holes towards N-side, a potential barrier is formed and electrons tend to stay towards the N-side [52]. The vacancy of electrons create a hole and these holes move towards the P-side [52]. All this happens due to the electromagnetic effect inside the cell or the P-N Junction [53]. This is how the current is formed inside the cell [54]. This above-mentioned procedure is shown with the help of a diagram in the figure.

Photoelectric Effect: In case of Photoelectric effect an actual emission of electrons take place from the surface of the material, on the surface of which the light is incident [55]. The phenomenon occurs when the incident photons provide enough energy to the electrons to break the bonds and emit from the surface [55]. In this case no flow of electric current takes place. The principle of photoelectric effect is shown in Figure 2.10.

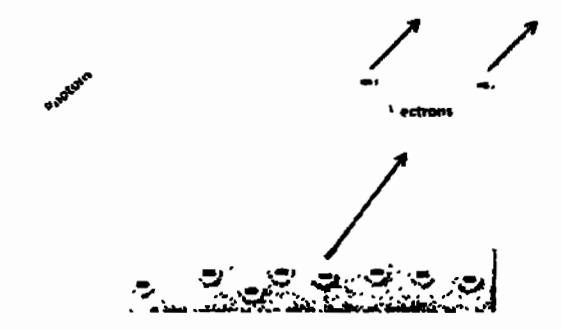


Figure 2.10: Photoelectric effect [56]

The electrons hence emitted are called Photo electrons [57]. Energy of the emitted electron is not a function of the energy of the incident light [57]. Electron is ejected if the energy of the incident light is enough to break free from the electron binding energy [57]. The number of ejected electrons depend on the number of photons with enough energy to break the binding energy of the electron and set it free to emit [57]. The energy of the incident photon in excess of this threshold is used to supply the emitted electron with the required kinetic energy [57].

### 2.3 Photodetectors and Photo Diodes

The incident light is converted into voltage or current in a photodetector. Photodiodes and phototransistors are the examples of photodetectors [58]. Photodetectors work in a similar way to the solar cell, where the incident light in the form of solar energy is converted into electrical energy [58]. Metal halide perovskite materials are one of the choicest materials for photodetectors [58].

The devices that are used for the detection of light are called photodetectors [58]. It would be more appropriate to say that they are photon detectors, they utilize the photoexcitation of electric carriers [58]. Photodetectors gives an electronic output signal – for example, the output might be delivered in the form of a voltage or electric proportional to the incident optical power [58]. They are thus categorized as optoelectronics devices [58].

Photodiodes are devices made of semiconductors, that come in two configurations p-n and p-i-n (i=intrinsic), depletion region absorbs the light and a photocurrent is generated [58]. These devices have high quantum efficiency, exhibit highly linear behaviour and are fast and compact [58]. They need be operated in combination with suitable electronics to tap all the above mentioned benefits [58]. Avalanche photodiodes are a particularly sensitive type of photodiodes that are sometimes used to count the photons [58].

## 2.4 Principle of Photodetection

There are two basic principles for photodetection., photovoltaic detection and photoconductive detection. Both of them are briefly discussed as follows.

## 2.4.1 Photovoltaic Detection

In this type of detection, there is a junction between the region where the conductivity is due to electrons namely N-type, and a region where conductivity is due to the holes, namely P-type [59]. That is to say a P-N junction is formed and when the light photons are incident upon the such detector a voltage is generated across the junction [59]. The basic principle of photovoltaic detection is shown Figure 2.11.

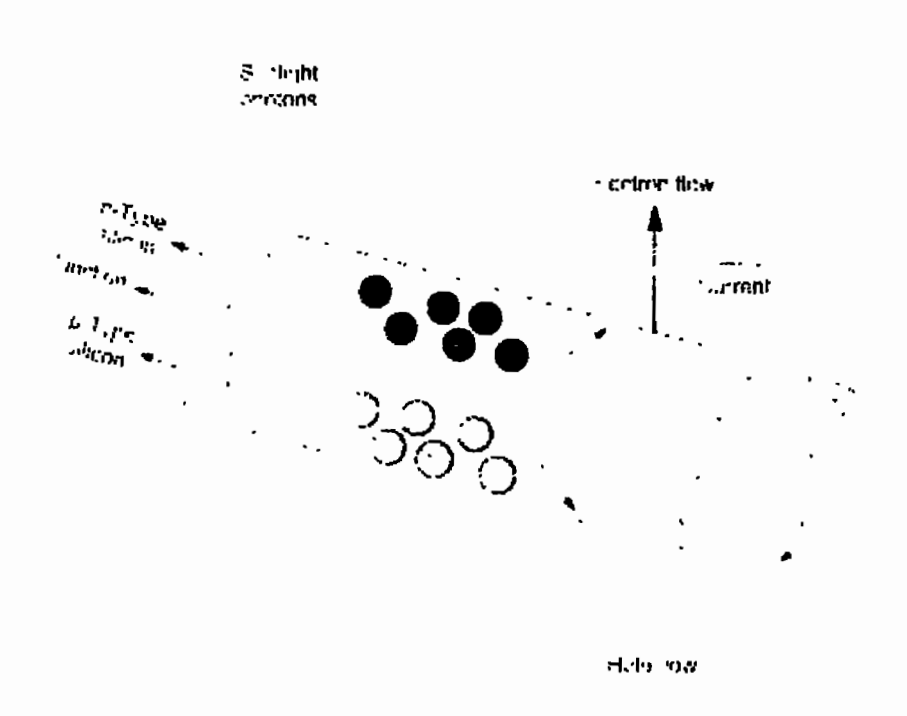


Figure. 2.11: Basic principle of Photovoltaic detection [60]

#### 2.4.2 Photoconductive Detection

In this kind of detection, the detector is made of some kind of semiconductor like Silicon and when the light photons are incident upon the detector surface, free electron are generated, which has an impact upon the conductivity of the detector [61]. The conductivity of the detector changes with the intensity of the incident light [61]. A simple photoconductive detective detector is shown in Figure 2.12.



Figure. 2.12: Photoconductive Mode [62]

## 2.5 Types of Photo-Detectors

There are many types of photo detectors. A brief discussion about a few of them is done in this section.

- PN Photo-Diode
- PIN Photo-Diode
- Avalanche Photo-Diode
- MSM Photo-Diode

During the 1940's photodiode technology came to the view as an application of the PN junction diode. When scientists came to know about the applications of the junction diode other than the rectification [63]. Photonic applications like photodiodes, solar cells, and light emission

were discovered [63]. More refinement was made in the field during the 1950's and during the latter part of that decade PIN diode was developed [63]. In 1959 Gartner wrote a research paper explaining the absorption of light by the wide depletion region [63]. Mostly Silicon and Germanium are used for making Photodiodes [63].

#### 2.5.1 PN Photo-Diode

This type of photodiode is the most basic [64]. It is simply a semiconductor with a P-N junction that converts light photon into electrical energy [64]. The P type layer has an abundance of holes while the N-type layer has an abundance of electrons [64]. Photodiodes are manufactured using various materials, some of them being Silicon, Germanium, and Indium Gallium Arsenide [64]. Each material has different advantages in terms of cost benefit, response time, sensitivity, wavelength range and low noise level [64]. The PN junction diodes comes in various varieties like PIN and APD diodes [64]. Fewer free charge carriers are contained in the depletion region, and its width can be manipulated by changing the applied bias [64]. There is only one direction for the flow of the current based on the position of the P an N type material [64]. In case of reverse bias, no current flows as long as the incident light creates the photo current [64]. A cross section of a basic PN Junction photodiode along with the symbol is shown in Figure 2.13.

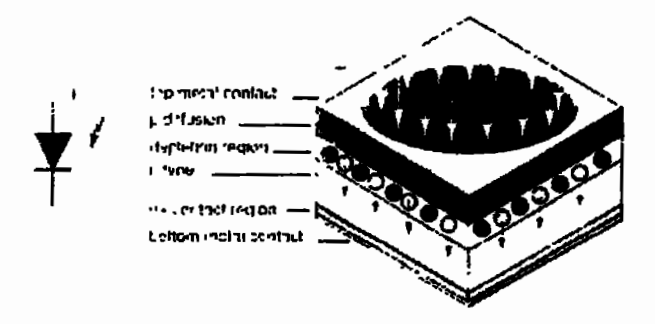


Figure. 2.13: Cross section of a P-N Junction Photodiode [65]

#### 2.5.2 PIN Photo-Diode

There is only one major difference in the PN and PIN photodiodes [66]. In PIN photodiode an intrinsic material is placed between the P an N type material as shown in the Figure. The intrinsic layer introduced in the structure is highly resistive and increases the strength of electric field in the diode [67]. The intrinsic layer increases the depletion region which is an added benefit [67]. The introduction of the intrinsic layer reduces the capacitance of the junction thereby increasing the speed of the diode [67]. The increased layer results in larger volume of conversion from photon to electron hole pair, causing an increase in the quantum efficiency [67]. A cross section of a PIN diode is shown in Figure 2.14.

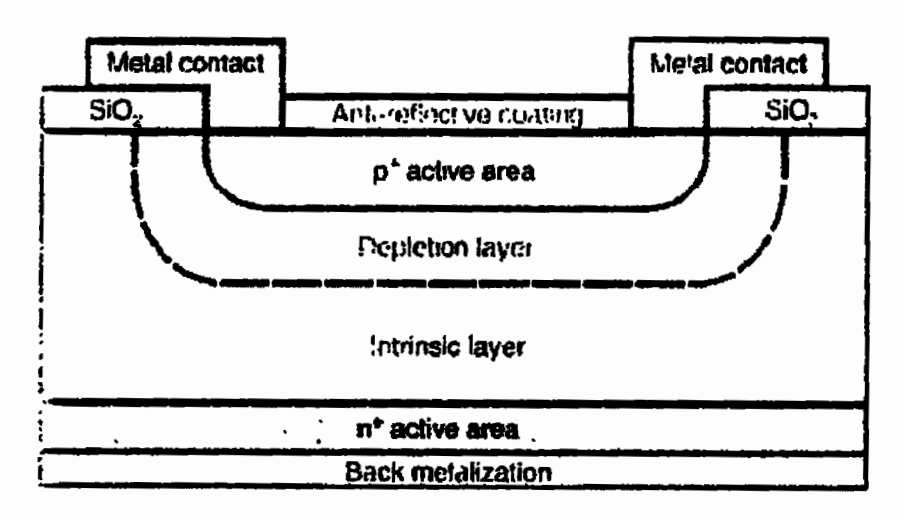


Figure. 2.14: Cross section of a PIN Diode [68]

PIN photodiode has no gain [69]. It can be of disadvantage for many applications, still it finds many applications like audio CD players DVD drives and many optical communication equipment [69]. One of the application of the PIN diode is that it is able to detect the nuclear radiations [69].

#### 2.5.3 Avalanche Photo-Diode

Avalanche photodiodes (APD) uses the phenomenon called impact ionization or the avalanche effect in order to create an internal gain in the material [70]. High reverse bias operation near

to the reverse breakdown voltage is required for the APD [70]. More electron hole pairs are created by each photo-generated carrier and so is multiplied by avalanche breakdown [70]. An internal gain in the photodiode is created by this, resulting in an increase in the effective responsivity of the diode, that is to say that larger current is generated per photon [70]. A cross section of the APD is shown in the figure. 300 – 1100 nm is the typical response range [37]. A higher value of current noise is observed in APD [70]. The increased signal gain is high enough to achieve high signal to noise ratio [70]. The response time of APD is much fast and it shows a higher capability to detect and measure light at lower levels [70]. Basic working principle of an Avalanche Photodiode is shown in Figure 2.15.

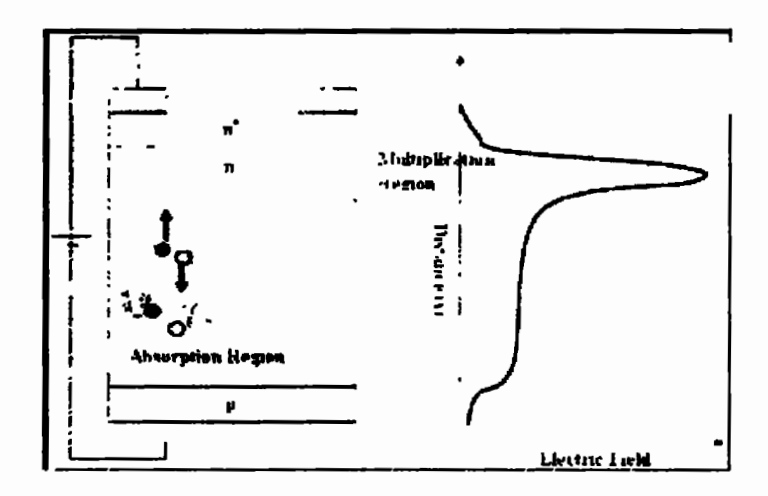


Figure. 2.15: Cross Section of an Avalanche Photodetector [71]

A relatively high reverse voltage, which ranges from tens to hundreds of volts, to the level of just below the breakdown voltage is required to operate an avalanche photodiode [72]. The electrons and holes excited by the photons are strongly accelerated by the strong electric field [72]. These accelerated electrons and holes generate secondary carriers [72]. All this avalanche process may take place over a few micrometres cause a significant amplification in the photocurrent [72]. It is therefore mostly used in the sensitive detectors where a strong amplification is required [72]. Typical applications of the avalanche photodiodes include the

fibre communication receivers, high speed laser scanners, laser microscopy, and optical time domain reflectometer (OTDR) [72].

#### 2.5.4 MSM Photodetectors

A couple of metal electrodes on semiconductor, make two Schottky contacts in a Metal-Semiconductor-Metal (MSM) photodetector [73]. This is contrary to a P-N junction as found in a photodiode [73]. MSM detectors have two Schottky junctions and can be categorised as a Schottky barrier detector [73]. Electrodes are subject to some applied voltage during the operation, when the light photons are incident upon the semiconductor in between the electrodes, Electrons and holes are generated [73]. A photo current is formed under the influence of electric field from these charged carriers (Electrons and holes) [73].

The finger spacing can be as small as 1µm can be observed in the interdigited configuration of electrode structure [73]. Ring shaped structure of electrodes can also be found that covers approximately a circular area [73]. The quantum efficiency is reduced due to the fact that electrodes partially block the light that hit the device from the side of the electrodes [73]. This drawback is removed by introduction of so called back illuminated devices [73]. In these devices the light avoids the blocking by electrodes by impinging from the other side [73]. A partially transparent gold contact with extremely thin dimensions can be used in combination with top illumination can also be used as a possible solution for the above stated problem of electrodes blocking the light [73]. The detection bandwidth achieved in case of top illumination is usually much higher [73]. The reason for this high achievement level is that the electrons and holes are generated in close vicinity to the contacts [73]. Optical waveguide are used for sending input fight in traveling wave configuration [38]. This configuration is utilized for achieving highest level of speeds because optical waveguide contains absorbing layer [73]. To form a coplanar waveguide line for the generated microwave signals, the electrodes are mounted on top of the waveguide [73]. The performance of the MSM detectors can even be

faster than the photodiodes [73]. Their detection can range up to hundreds of Gigahertz [38]. This makes them fit for utilization in ultra high speed fibre communication [73]. A very pertinent, and important to the modern day technology and research needs, characteristic of the MSM photodetectors is that it has a comparatively simple planar structure, which makes it befitting for the monolithic integration with other photonic and electrical components in a photonic integrated circuit [73]. A typical MSM detector with comb structure is shown in Figure 2.16.

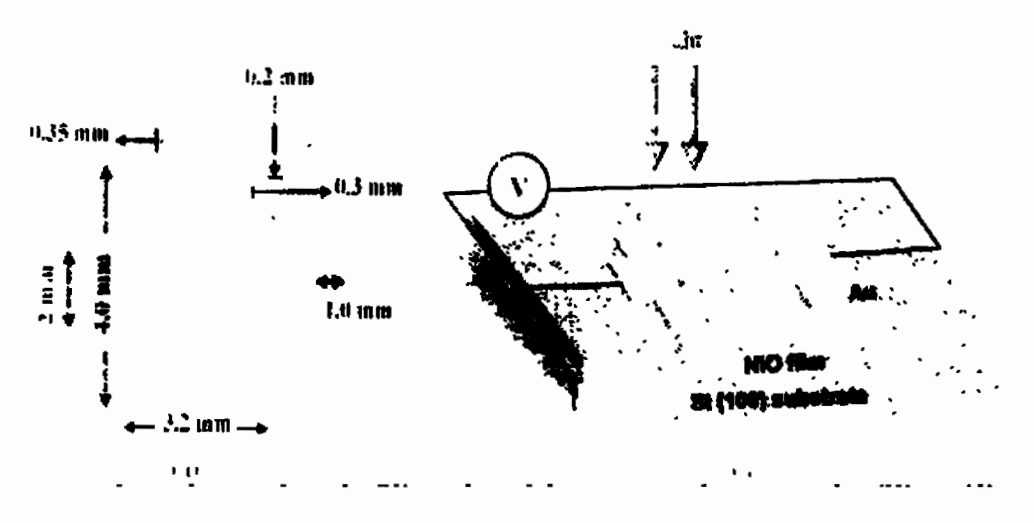


Fig. 2.16: Typical MSM detector [74]

### 2.6 Summary

This chapter reviews the background theory of the problem and introduces the reader the basic information required to grasp the complexities to be tackled during the course of this thesis. It introduces the basic concepts of the electromagnetics like Electromagnetic spectrum and its constituent components like gamma rays which are at the top of the spectrum in terms of the highest frequency. With its capability to kill germs it can play useful role in many ways. This is followed by a description of X-rays and its ability to penetrate in to the human body. This followed by a description of ultraviolet, Visible light, infrared, microwave and radiowave parts

of the electromagnetic spectrum. The benefits as well as the related hazards of each one is discussed. Ultraviolet being the focus of the research is discussed in some detail with its different components like UV-A UV-B and UV-C and the frequencies which are described as Deep UV. In the next section Photovoltaic and photoconductive effect and their differences are discussed. In case of the former the incident light generates the voltage while in later case electrons are ejected as a result of the incident photons, in the presence of external bias. This is followed by the description of Photodetectors and Photodiodes, where photodetectors detect light on the basis of changes observed as a result of incident light in voltage, current, and conductivity, Photodiode are kind of Phototransistors. Photodetection is based on two principles, one is called the Photovoltaic detection and photoconductive detection, in case of the former the incident light produces sufficient voltage to be detected, and in the case of later the incident light enhances conductivity. At the end some types of photodetectors are discussed, a summary of which is given in the table 2.1.

Table 2.1: Summary of the different devices discussed in the chapter

Sr.	Device Type	Working Principle	Major Advantage	Drawback(If any)
no 1	PN Photodiode	PN Junction	Simple,	Limited scope
•	1 14 1 Howarde	diode	Unidirectional	Emma scope
2	PIN Photodiode	Intrinsic material placed between P-type and N-type material	Reduced capacitance, Fast speed.	No gain
3	Avalanche Photodiode	Avalanche effect	Increased responsivity	Higher Noise
4	MSM Photodiode	Two Schottky contacts	Better integration in photo integrated circuits	Reduced quantum effeciency

# Chapter 3

## Literature Review

Literature regarding the Ultraviolet band and the use of Aluminium Nitride and related materials is thoroughly searched, understood, and revised during this research. A large amount of literature is available online regarding the use of Aluminium Nitride and various other Nitrides for UV detection and generation. Boron Nitride and Aluminium Gallium Nitride have been widely used for these purposes. A new research interest in the Aluminium Nitride due to its wide direct band gap has swept the academia lately. A few of the publication read have been reviewed in this chapter

Ababneh et al. investigated the piezoelectric characteristics of Aluminium Nitride, Aluminium Nitride is known for it's piezoelectric characteristics and high Complementary Metal Oxide Semiconductor (CMOS) compatibility [75]. It is also known for its high acoustic wave velocity, chemical inertness, good electrical isolation and a wide bandgap [75]. Many sensors, actuators, LED's exploit these properties of Aluminium Nitride for the efficiency and effectiveness of their function. In optoelectronics, its functions are especially well pronounced due to the wide bandgap and the consequential utilization in the fields of UV and deep UV [75].

This study focuses on the optical properties of the reactively sputtered AIN, investigated in relation to the physical properties namely the c-axis orientation, using the spectroscopic ellipsometry [75]. The results establish a direct relationship between the optical properties of the sample, like refractive index, in relation to its c-axis orientation, keeping the thickness of the sample constant [75]. That is to say that sample with high c-axis orientation yielded higher values of the refractive index compared with those with lower c-axis orientation or amorphous structures [75]. A comparative relationship between (002), peak intensity measured with x-ray diffractometry and refractive index showed that at a wave length of 546nm, the refractive index

showed a fall from 2.15 to 2.11 for films having half peak intensity [75]. For films with out preferred orientation it further plunged to 1.9. The study also showed that, if the sputtering conditions are remained constant than refractive index is not a function of the thickness of the sample [75]. It is also seen that the results remained consistent for Aluminium Nitride thin films using the X-ray reflectivity measurements, and the refractive index measurements [75]. Mass density for those high c-axis orientation, Aluminium Nitride thin films, which reported higher values of refractive index was observed to be 2.99g/cm<sup>-3</sup>, while it was observed to be 3.23g/cm<sup>-3</sup>, and 2.82g/cm<sup>-3</sup> for epitaxially grown and poor c-axis orientation samples respectively [75].

This study can be helpful in reaching an estimate regarding the piezoelectric coefficient of a Aluminium Nitride thin film sample [75]. It can reduce the burden of pre-processing of samples for an experiment [75]. The sputtering technique, the c-axis orientation, and the refractive index of the sample can give a reasonably good estimate it's piezoelectric coefficient [75]. This procedure can save cost both in terms of time and money and can be to the benefit of R&D as well as the industry [75]. A schematic representation of optical model for ellipsometry analysis is shown in Figure 3.1.

C-Si

Figure. 3.1: Schematic representation of optical model for SE analysis [75]

Mondal et al. take a dip in to the use of AlN and AlGaN in manufacturing of the UV LED.

LED industry is an ever growing with its low power consumption and environment friendly properties [76]. Recently the demand for the UV LED has seen a spike due to the numerous benefits of the UV light in sterilization [76]. The mercury based UV lamps, that are being currently used to extract the UV light are not environment friendly, and many countries in the

developed world have signed conventions banning the usage of mercury for its antienvironmental properties [76]. This dilemma can only be resolved by replacing the mercurybased UV lamps with the environment friendly UV based LEDs [76]. But the problem faced here is the lower efficiency of the UV LED's. Different categories of UV along with their potential benefits are shown in Figure 3.2.

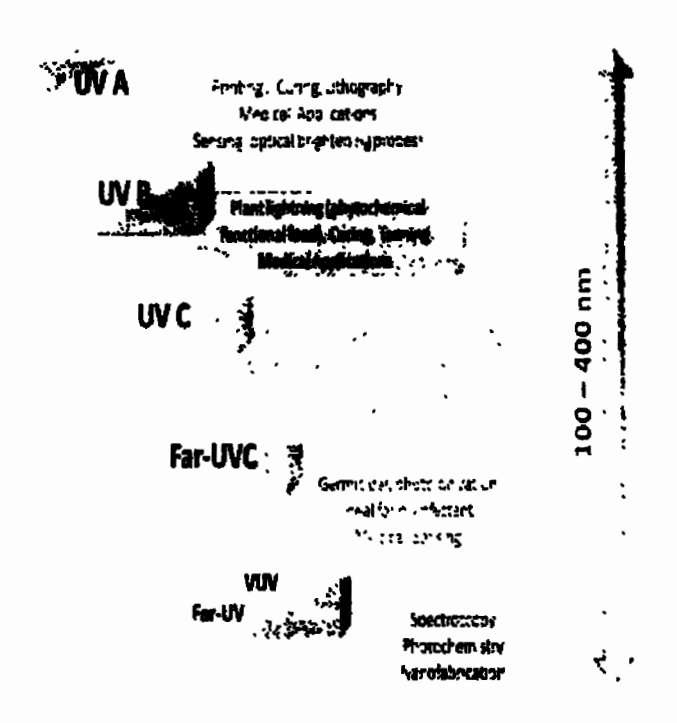


Figure 3.2: Different categories of UV and their benefits [76]

The efficiency of a UV LED can be measured in numerous ways. Among them the most critical is the external quantum efficiency of the (EQE) [76]. It is the ratio of incident photon to converted photons. Numerous studies show a huge decline in this figure in case of the UV LED as compared to the blue LED [76]. The possible reasons are, Higher threading dislocation density for high Al composition AlGaN epilayer. Low hole concentration due to higher activation energy of Mg in high Al concentration AlGaN alloy [76]. It also suffers from low light extraction efficiency (LEE) due to TM-mode dominant emission from Al alloy [76].

This paper concludes that there is a huge potential in III-nitrides based UV LED's for medical, defence and sanitation purposes [76]. A lot of focussed research is required to bridge the efficiency gap between the blue LED and the UV LED [76]. A lot of research work still needs to be done to tap the potential of the UV LED on commercial level [76].

Porcela et al. aim to integrate a complex photo integrated circuit over a monolithic substrate with various benefits, like volume reduction, increase in scalability factor, and physical stability [77]. Now that the IC fabrication technology has advanced many folds, many of these techniques are being applied to the photo integrated circuits [77]. Photo Integrated Circuits (PIC) have just matured enough to be available for the commercial use [77]. A lot of research on Silicon on Insulator(SOI) technology during the last decade has focused basically on the PIC [77].

Silicon Nitride has been of late the material of choice for the PIC [77]. It has a lower refractive index and is amorphous and CMOS compatible, which makes it tolerant to fabrication imperfection and waveguide side wall roughness, resulting in propagation losses [77]. These afore mentioned properties of the Silicon Nitride also make it a fit case for monolithic cointegration with Silicon diodes and C-MOS based electronic circuitry [77]. For biochemical and medical sensing, the properties of interest for Silicon Nitride are chemical and thermal stability, as well as transparency range which covers from 400nm(UV) to mid infrared [77].

The review paper has discussed the role of Silicon Nitride in building Photonic waveguides and circuits with all its potential benefits and with a clear focus of visible light band and biophotonic applications [77]. An SiN based gas sensor PIC manufactured by Lionix Intl is shown in Figure 3.3.



Figure. 3.3: A SiN based gas sensor PIC, manufactured by Lionix Intl [77]

Ma et al. studied in depth the point defects in the AlGaN based DUV LED based on the fact that, AlGaN based deep ultraviolet LEDs, with higher Al composition have many lucrative applications like, water purification, and fluorescence sensing [78]. It is worth it to focus the research in to studying the impact of point defects in such LED's. For this publication, a 265nm Deep Ultraviolet LED is observed using various analytical techniques like, Cathodoluminescence, Deep Level Transient Spectroscopy, and Transmission Electron Microscope, for point defects before and after degradation [78]. The results show that point defects increase after degradation [78]. Generated defects lead to carrier redistribution in the active region. Induced point defects were found to be located inside the Multi Quantum Well (MQW), especially the first quantum well near the P-side of the LED. Dislocation lines were also observed in MQW region after degradation [78]. Which consequently can lead to Mg diffusion along dislocation lines [78]. These finding are important in understanding the role of Point defects in AlGaN Quantum Well, both before and after the degradation [78]. This information can be of great importance for improving the performance of AlGaN based Deep Ultraviolet LED [78]. Cross sectional aberration-corrected stem image of the fresh UVC-LED chip is shown in Figure 3.4.

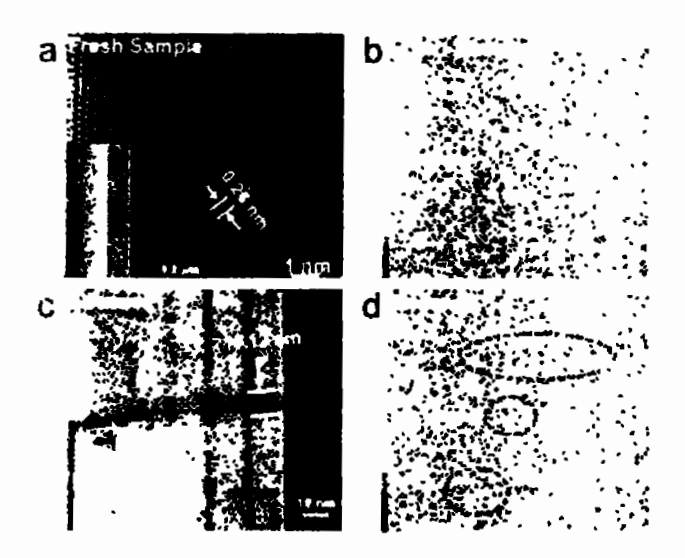


Figure. 3.4: Cross sectional aberration-corrected stem image of the fresh UVC-LED chip [78]

Taniyasu et al. worked with Aluminium Nitride, and doped it with N-type with Silicon (Si) and P-type with Magnesium (Mg) [79]. The doping pattern are then studied at various temperatures [79]. After the removal of the dislocation density, a value of 426 cm²/VS was achieved [79]. Electron mobility with respect to the variation of temperature and the doping concentration was studied [79]. It was observed, for N-type doping of Si, that between the doping concentration of 10<sup>18</sup> and 7×10<sup>19</sup>cm<sup>-3</sup>, the N-type conductivity of the and the carrier concentration increased with the increase in doping concentration [79]. Increasing the value of doping concentration from this threshold value the electron mobility decreases and the conductivity drops [79]. A schematic of vertical and lateral Aluminium Nitride grown on Silicon Carbide substrate is shown in Figure 3.5.

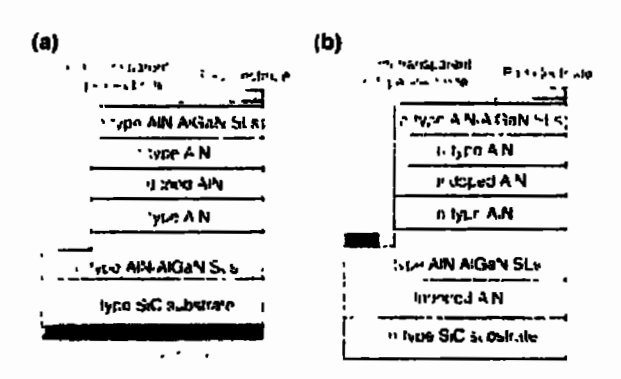


Figure 3.5: Schematic of (a) Vertical (b) lateral AIN LEDs grown on n-type SiC(001) substrate [79]

Conductivity and electron mobility was also studied for P-type doping with Mg ion [79]. It was found out that at a doping concentration 2 × 10<sup>19</sup>, as the temperature was increased the hole concentration increased exponentially and did not saturate even at a temperature as high as 1000K. Finally the lateral and vertical AIN UV LED were fabricated [79]. Electroluminiscence (EL) was observed [79]. A deep UV light emission of 209.8nm was observed for the vertical LED, while that of 208.9nm was observed for the lateral LED [79]. The EL was attributed to the near band edge emission of AIN. The temperature coefficient of EL was dound out to 0.67 meV/C [79]. The vertical LED was found out to be better than the lateral LED because of the lower operating voltage and hence a lesser chance of self heating [79].

Legesse et al. in this paper experiment with Al concentration in the Boron Nitride. The result found was a significant fall in the value of Band gap [80]. Boron Nitride is a promising material for possible usage in optoelectronics devices, multifunction composites, and biological materials [80]. It was found out that at the concentration of 12.5% of Al, the band gap of Boron Nitride falls from 5.95eV to 4.1eV, which is a major fall in the value [80]. This engineering of the bandgap is desirable for the possible usage in optoelectronics devices [80]. Moreover it was found that distance between the substitutional Al atoms had an effect on the defect related intermediated bands which in turned effects the bandgap of the structure overall [80]. Another significant finding is that increasing the Al concentration will make the two-dimensional BN

structure thermodynamically stable [80]. All these finding can have a desirable effect on the UV optoelectronics industry and for and deep of BN in usage UV optoelectronics applications [80]. As the band gap engineering is important for efficiency enhancement and power ratings of the device which is the area of interest in the latest research. A higher thermal stability means, strong endurance of longer life of the device [80]. The honey comb structure of 2D h-BN supercell is shown in Figure 3.6

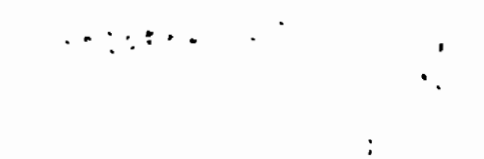


Figure. 3.6: (a) The honeycomb structure of the 2D h-BN supercell B atoms shown in green N in gray (b)

Calculated electronic band structure of the 2D h-Bn supercell [80]

Naderi et al. designed a high performance UV detector using a porous Silicon Carbide (SiC) thin film on a n-type (100) Silicon Substrate [81]. A thin film of Silicon Carbide was epitaxially grown on the Silicon substrate [81]. In order make the thin film porous, a two-electrode photo assisted electrochemical etching process was carried out using an integrated circuit [81]. It was found out that tuning of anodization current density resulted in the improvement of the optical properties [81]. It was also found out that current density is an important parameter for controlling the morphology of the porous SiC sample [81]. Optical properties were studied using Photoluminescence [81]. It was established that optimizing the amount of etching current density, results in the lessening of the light reflectivity [81]. Which is because of the specific elevated areas of porous region, which captures the light in short term by internal reflection and reduces overall reflectivity [81]. The UV sensing capability of the MSM structure was also investigated, and it was found out that, UV sensitivity was enhanced in optimized porous sample [81]. This enhancement was found out to be the result of enhanced photogenerated

current [81]. Enhanced photosensitivity means an enhancement in the performance in photo detection [81]. Ultra-fast detection of the UV light was also observed in the sample, which also points out toward a better performance of the device [81]. Surface morphology of the porous Silicon Carbide on Silicon Substrate using UV assisted electrochemical anodization technique for synthesis is shown in Figure 3.7 [81].



Figure. 3.7: Surface morphology of porous silicon carbide on Si substrate synthesized using UV assisted electrochemical anodization technique with different etching current densities (a) 5 (b) 10 and (c) 15 A/cm<sup>2</sup> for 10 mins [81]

Zhang et al. resolve a standing technical problem, that of environment friendly synthesis of nanostructural Aluminum Nitride, that is both pure up to 97% and has good disparity [82]. A arc discharge with assistance of direct Nitridation has been used and suggested in this research article [82]. An average particle size of 99.1nm has been achieved, while the specific area of was found out to be 60.8 m²/g [82]. The proposed procedure can avoid agglomeration and coalescence of Aluminium Nitride for the next Nitridation cycle [82]. The direct Nitridation process required a very high temperature of 600 C, for a longer time period of two hours [82]. The nitridation temperature can be reduced using arc discharge [82]. This research provides a new opening in technological advancements towards creating metal nitrides with high levels of purity and disparity [82]. The diagram for process of AlN synthesis using arc discharge with the assistance of direct nitridation is shown in Figure 3.8 [82]. The synthesis mechanism of high purity AlN by arc discharge with the assistance of direct nitridation is shown in Figure 3.9 [82].

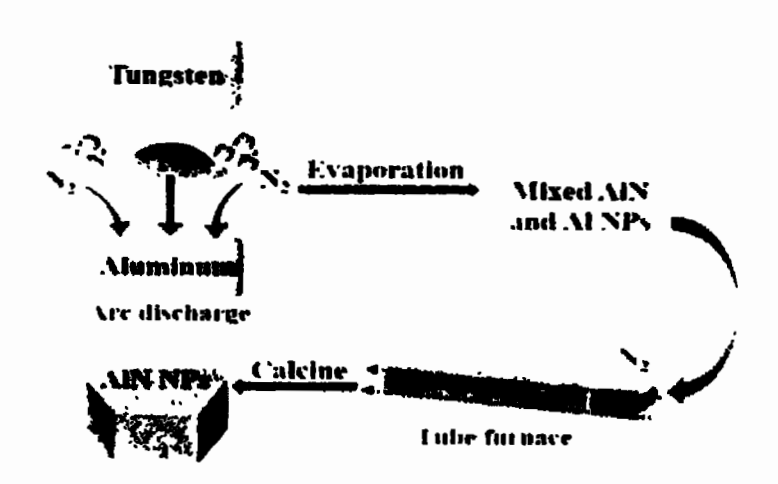


Figure. 3.8: The process diagram of AIN synthesis by arc discharge with assistance of direct nitridation [82]

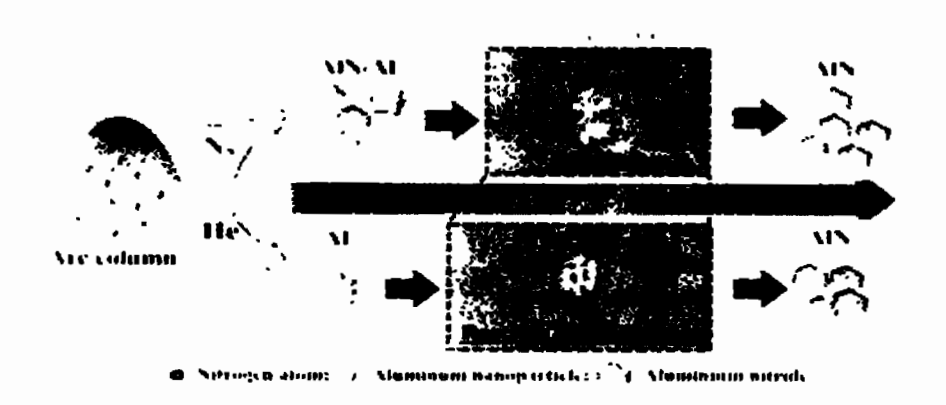


Figure. 3.9: The synthesis mechanism of high purity AIN by arc discharge with assistance of direct nitridation [82]

Asghar et al. conducted deep level transient spectroscopy on boron-nitrogen co-doped 6H-SiC, exhibiting p-type characteristics and conductivity having hole concentration  $3\times10^7$  cm<sup>-3</sup> [83]. 6H-SiC doped with Al is an area of deep interest for the LED industry. LED industry is lucrative due its possible benefits in the form of low power consumption, environment friendliness [83]. Although the LED industry has grown pretty rapidly since its inception in the 1980's, and SiC based LED's have the capability to cover the entire visible light spectrum, White LED still suffers in terms of the quantum efficiency [83]. Al doping of SiC further enhances the performance [83]. It was found in the literature that one of major contributor to the degradation of the efficiency is the thermally induced emission of carriers from donor or

acceptor to the respective band [83]. The DLTS results reveal the presence of majority carriers holes(H<sub>1</sub>) and minority carriers electrons (E<sub>1</sub>), at trap level of +0.24eV and -0.42eV [83]. According to the literature these defects were found out to be Al-acceptor and N-donor defects [83]. Representative spectrum for DLTS of 6H-SiC exhibiting majority and minority carriers is shown in Figure 3.10 [83].



Figure 3.10: Representative DLTS spectrum of 6H-SiC exhibits the minority and majority carriers [83]

Lee et al. developed a new sort of photodiode by combining a commercially available photodiode with layer of Quantum Dots (QD) [84]. Normally the Silicon based photodiodes are mostly preferred in the industry due to the abundance of the Silicon and the commercially viable, but lately Silicon Carbide based devices with Aluminium and other useful dopants have been in business [84]. A layer thickness of the Quantum Dot layer was managed between 0.3 and 2.7um using simple spraying and drying process, for a better UV detection [84]. The results showed a 2.2 to 5.9 times better photocurrents, than the normal photodiodes [84]. The responsivity of the QD deposited photodiodes was found out to be 300% as compared to the normal Si based photodiode and 150% as compared to the Galium Phosphide based photodiode [84]. The effect of thickness of the QD layer, and the wavelength of the incident light for detection were also investigated in accordance with the surface morphology and optical and photoluminescence characteristics of the deposited QD layer [84]. The research can go a long way in dealing with challenges in the visible and UV photonic devices industry [84]. A

schematic of fabrication of the quantum dot coated silicon photodiode, and the photograph of the quantum dot layer deposited, is shown in Figure 3.11 and 3.12 respectively [84].



Figure 3.11: Fabrication schematic of the quantum dot (QD)-coated silicon(Si) photodiodes (SIPDs), featuring spraying and drying of nanocrystals QDs, and photograph of spray coating using an airbrush noozle[84]

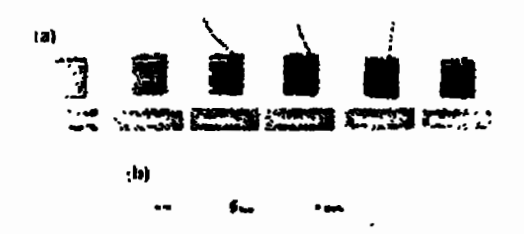


Figure 3.12: Photographs of QD layers deposited on SIPD (a) quartz substrate (b) by spraying the drawing process wrt number of spray steps[84]

Ahmad et al. proposed a combined Boron Nitride/Graphene Oxide composite photodetector, using a drop cast method for photodetection both in visible and UV ranges [85]. Morphology of the Graphene Oxide and the distribution of the BN nanoparticles and the alignment of B, N and O particles were confirmed using field emission scanning electron microscope (FSEM) and the "Energy dispersive X-Ray [85]. Excellent conduction of UV in the range of 380nm to 405nm, was seen and that of red light at 650nm [85]. These results show independency of conduction from wavelength and dependency on the power of the laser [85]. The device sensitivity was found out to be a direct function of the DC bias voltage [85]. By increasing or decreasing the DC bias voltage we can fine tune the sensitivity of the device [85]. One of the

most important findings of this research the self-powering capability of the device. Powering up the device using external bias involves various drawbacks including the heating up of the device and the consequent depreciation of its performance, and lesser life time [85]. Device in this research shows an enhancement of 3450% at zero bias. Which can be set as a baseline for future in the research for self-powered devices [85]. Schematic diagram of preparation of BN/GO composite layer on Silicon dioxide or Silicon substrate and their experimental setup for I-V and temporal measurements is shown in Figure 3.13 [85].

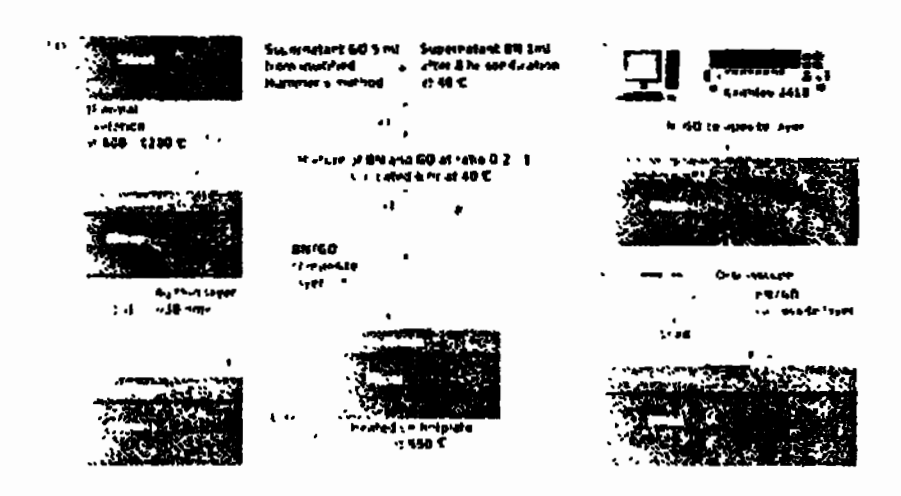


Figure 3.13: Schematic diagram showing (a) preparation of BN/GO composite layer on Sio<sub>2</sub>/Si substrate and experimental setup (b) I-V and (c) temporal measurement [85]

Zielony et al. investigated acceptor doped ZnO for defects. Investigation was carried out for ZnO:As/N-GaN hetrojunction for various electrical characteristics using procedures for Current-Voltage I-V and Capacitance-Voltage C-V analysis [86]. Deep level transient spectroscopy was also applied to study deep level defects. In addition to that Photoluminescence and secondary ion mass spectroscopy was also applied to gether information bout the physical attributes of the hetrojunction [86]. The I-V analysis confirmed the formation of trap centers in the heterojunction [86]. C-V analysis gave us the information that the depletion region of ZnO is formed in the heterojunction region [86]. The DLTS analysis

told us about the presence of three hole trap related signals in the junction [86]. Their respective activation energies were also found out [86]. All this data gave a good insight about the various electrical and morphological dynamics of the said hetro-junction, which could contribute to better understanding of one of the most useful material of modern times i.e. ZnO [86]. Measured and simulated DLTS spectra of the ZnO at different lock frequencies is shown in Figure 3.14.

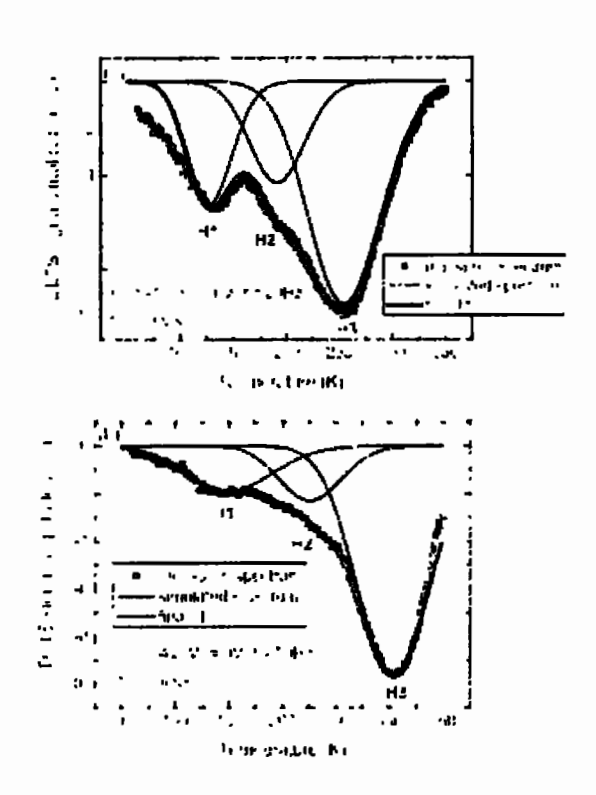


Figure 3.14: Measured and simulated DLTS spectra of the ZnO: As/n-GaN diode (a) for lock in frequency of 20Hz (b) 50Hz [86]

Jiang et al. developed a two step sintering process for AlN, s with Yb2O3 and YbF3, which yields a sample that achieves full density and limited grain size in comparison with the one step sintering process [87]. Aluminium Nitride with its unique properties like, higher insulation. higher thermal conductivity, lower thermal expansion coefficients, chemical stability and low dielectric constant, has become a focus of research for high power integrated

circuits [87]. The above mentioned properties make Aluminium Nitride more durable a suitable for the devices with higher power ratings [87]. In this research in addition to the higher density and lower grain size, as mentioned above, higher flexural strength and higher thermal conductivity were also observed [87]. The electrochemical impedance spectroscopy revealed, lower concentration of aluminium vacancy in the two steps sintered AlN ceramics, as compared to the one step sintered one, which resulted in higher thermal conductivity [87]. The research proved that the two steps sintering process has a desirable effect on the electrical mechanical and thermal properties of the processed AlN, which could be used to our advantage [87]. Figure 3.15 shows the SEM results of the fracture surfces of AlN ceramics.

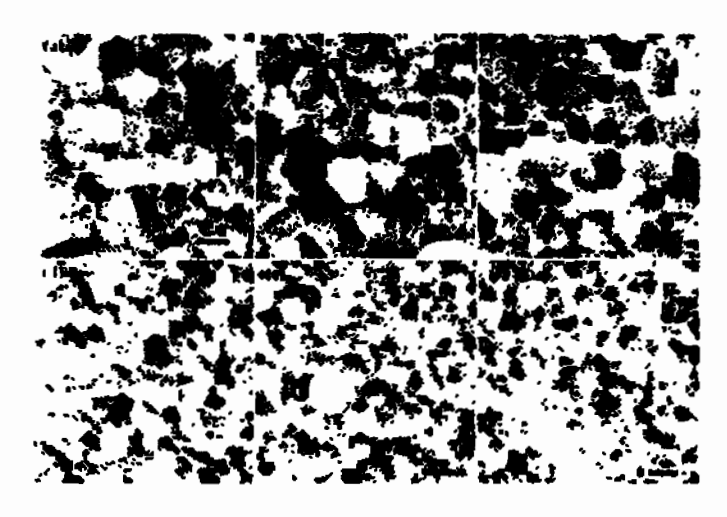


Figure 3.15: SEM of the fracture surfaces for AlN ceramics [87]

Fahad et al. probed in to Cadmium Telluride (CdTe) based solar cell, which has lately created some ripples in the research world by reporting an efficiency as high as 22%, theoretically this can further be enhanced to 25% and above [88]. Device fabrication and cleaning process is shown in Figure 3.16. One of the limiting factor of the efficiency of the solar cell is the open circuit voltage V<sub>oc</sub>. The highest value of the open circuit voltage reported until now is 600mV [88]. During this research the value external voltage was exceeded from this value to 700mV, 800mV, 900mV and 1000mV. QDLTS was also applied to at different temperature regimes and in dark and luminous conditions [88]. QDLTS charging and discharging cycle is shown in

Figure 3.17. High recombination trap centres were found at 0.448ev, 0.383eV, 0.366eV and 0.341eV. These trap centres are an impediment enhancing the value of open circuit voltage [88].



Figure 3.16: Device Fabrication and cleaning process [88]

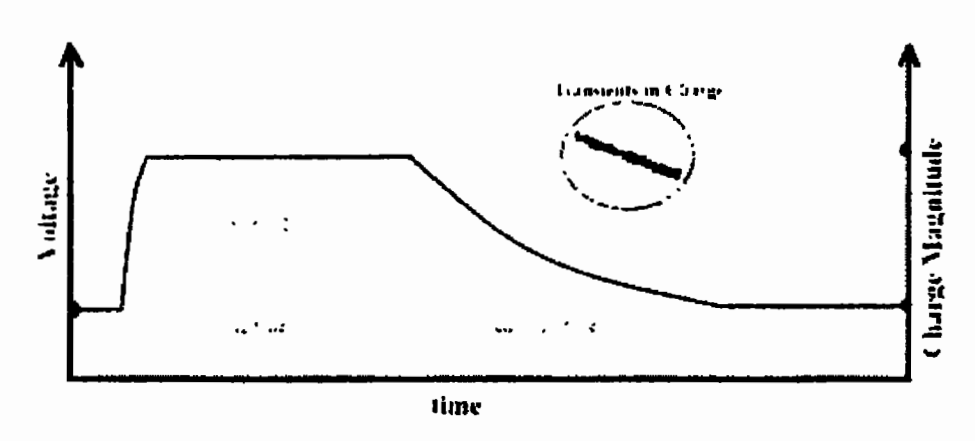


Figure 3.17: Q-DLTS approach of charge and discharge events for localized traps of CdTe lattice [88]

We aim to detect visible as well as the UV light spectrum by doping AlN with N-type Silicon. The resultant device has band gap reduced to such a level that, a detectable amount of current is produced by the incident light in visible as well as UV light spectra. Bandgap engineering of the Aluminium Nitride is a very crucial area in UV and DUV research and development. Further research in this area will refine the detection and the amount of doping required to optimize the detection process. The detailed analysis has been given in Chapter 5 at length.

# 3.2 Summary

Different research articles were reviewed from the related available literature, with a focus on Aluminium Nitride for UV and DUV applications. Some literature regarding the experimental techniques used in this specific research was also reviewed. Ababneh et al. established a direct relationship between optical properties and c-axis orientation by focussing on optical properties of reactively sputtered AlN [75]. Mandal et al. reviewed the use of Aluminium Nitride and Aluminium Galium Nitride in the manufacturing of UV LED. A higher value of threading dislocation density and lower light emission efficiency was found with TM mode dominant emission of Al alloy being the possible reason [76]. Porcela et al. achieved volume reduction, increased scalability and physical stability by integrating a complex photo-integrated circuit over monolithic substrate [77]. Ma et al. applied cathodoluminescence and QDLTS on 265 nm deep UV LED and studied point defects before and after degradation inside the quantum well. An increase in the number of defects was observed after the degradation [78]. Taniyasu et al. doped Aluminium Nitride with N-type Silicon and P-type Magnesium [79]. Increasing the value of doping from a certain threshold resulted in decrease in electron mobility and conductivity [79]. Legesse et al. engineered the bandgap of Boron Nitride with variation in Al concentration in it(BN) [80]. Naderi et al designed a high performance UV detector using porous Silicon Carbide [81]. Zhang et al. recommended arc discharge synthesis of nanostructural Aluminium Nitride for eco-friendly purposes [82]. Asghar et al. applied QDLTS technique on Boron-Nitrogen co-doped 6H-SiC, and observed that Aluminium and Nitrogen provide acceptor and Donor defects respectively [83]. Lee et al. developed a new photodiode by combining a commercially available photodiode with quantum dots [84]. Ahmada et al. proposes a combined Boron Nitride/ Graphene oxide photo detectors using a drop cast method for photodetection both in visible and UV ranges [85]. Zielony et al. investigated ZnO:As/N-GaN hetrojunction for various IV and CV characteristics developing a good insight about electrical and morphological dynamics of the said hetrojunction [86]. Jiangra et al. developed two level sintering process for AIN with YbF3 and Yb2O3 yielding a sample with better density and limited grain size in comparison to the on step sintering process [87]. Fahad et al. reported an efficiency enhanced to 25% by identifying and fixing traps impeding the efficiency [88].

# Chapter 4

# Fabrication and Characterization Techniques

In this Chapter, different fabrication and characterization techniques used during the course of this research will be identified and discussed in some detail.

## 4.1 Fabrication Techniques

The thin film Aluminium Nitride was grown on the Silicon substrate using various fabrication techniques like, Epitaxial growth and physical vapor deposition (PVD) [89]. A brief account of these techniques is given as follows.

## 4.2 Epitaxial Growth

Epitaxial growth is basically a condensation process, of the liquid state or vapor form gas to form a thin film on a substrate [89]. Molecular beam is also sometimes used in the process. Several Epitaxy techniques are available, like, Molecular Beam Epitaxy (MBE), and Atomic Layer Epitaxy (ALE), It is important to ensure that the deposition process is slow enough to let the deposited layer atoms to adjust to the lattice structure of the substrate [89]. The layer grown through epitaxy is called the epitaxial layer [89].

## 4.3 Types of Epitaxy

There are various types of Epitaxial growths or epitaxies, that are currently in use in the industry, some of the names were mentioned above [89]. Following are the major types of epitaxial growth. They are described in some detail below.

- Molecular Beam Epitaxy [89]
- Microchannel Epitaxy [89]
- Hydride Vapor Phase Epitaxy [89]

### 4.3.1 Molecular Beam Epitaxy (MBE)

This technique is suitable for the profile having composition and doping dimensions in Nanometre scale. MBE growth has two dominant traits [89]. One being that, their interfaces are smooth in two dimensional structures and the other that, in three dimension there will be found nano islands which completely confine the carriers [89]. A schematic drawing of generic MBE system and its typical effusion cell is shown in Figure 4.1 and 4.2 respectively.

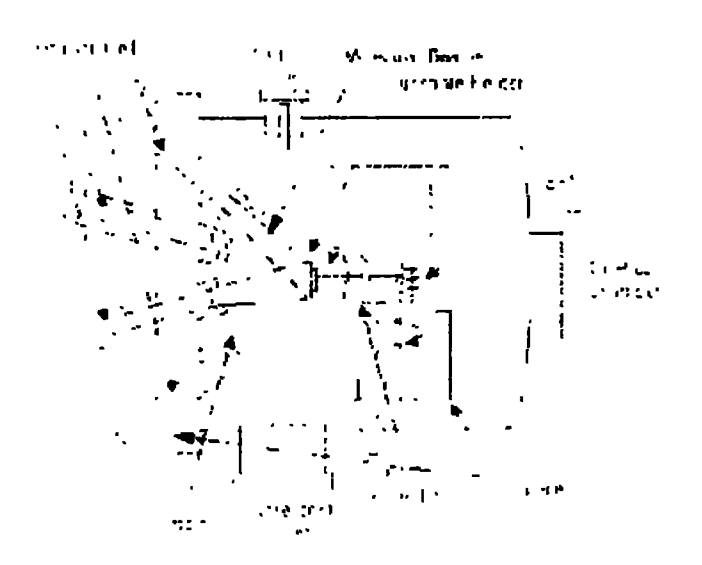


Figure. 4.1: Schematic Drawing of a generic MBE system [89]



Figure 4.2: Schematic drawing of a typical MBE effusion cell [90]

The underlying principle of MBE growth is quite simple: it essentially consists of atoms or clusters of atoms, that are produced by heating up a solid source [90]. They then migrate in an Ultra High Viscosity (UHV) environment and stick on the surface of hot substrate, where

diffusion takes place and eventually incorporate into the growing film [90]. Despite the conceptual simplicity, a great amount of technology is required to produce systems that produces the desired quality of material purity, uniformity and interface control. [90].

#### 4.3.2 Microchannel Epitaxy

Epitaxial Lateral Overgrowth (ELO) and Selective Area Epitaxy (SAE) are combined in Microchannel Epitaxy (MCE) [91]. ELO is an old school technique in semiconductor epitaxy [91]. Jastzebski proposed the name for ELO [4]. Both ELO and MCE use mask manufactured according to a set template [91]. These masks can be amorphous or of matal films [91]. Tsaur et al in the year 1982 first reported the dislocation density of 104 cm<sup>2</sup> in the layer grown through epitaxy by hetroepitaxy of Galium Arsenide on Germanium or Silicon substrate [91], 110

In case of MCE, the propagation of dislocation networks is deliberately stopped in the epitaxial layer at the time of transference of lattice information [91]. This is achieved because of the property of amorphous films to stop the propagation of information regarding lattice defects and deliver the information regarding lattice structure [91]. Nishinaga et al and Ujiie et al reported that a dislocation free area of significant width can be formed using MCE, over the seed outside of dislocation area [91].

Two methods can be used for doing MCE [91]. Horizontal MCE & Vertical MCE [91]. There occurs a simultaneous transmission of defect related information and lattice information on the epitaxial layer in case of conventional epitaxy [91]. This can be seen in the figure[] below. MCE accomplishes the main purpose of transferring the complete information regarding the lattice structure through small openings while blocking the defect related information from being transferred to the epitaxial layer [91]. In horizontal MCE, amorphous layer blocks the propagation of defect information to the epitaxial layer, while lattice related information is transferred through small openings [91]. That's why a defect free layer is realized using ELO

[91]. In case of vertical MCE, epitaxial layer is constructed vertically as shown in the figure below. This method not only stops the propagation of dislocations, but also move such dislocations out of the side surface by choosing proper orientation of the substrate [91]. The type of the MCE that is vertical relates to using Selective Area Growth (SAG) for shaping up the growth [91]. In the process flow of MCE an amorphous mask is deposited on the epitaxial substrate with small openings and small openings called microchannels are formed in the mask [91]. Then the epitaxial growth takes place in the openings in the form of seeds and in the direction of the lateral growth [91]. The region over the seed restricts the area dislocation and an area free of dislocation is formed [91]. Stepwise process of epitaxy is shown in Figure 4.3.

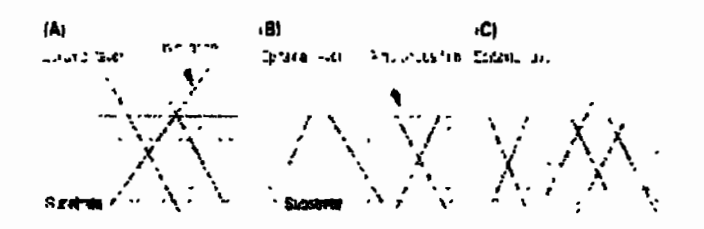


Figure 4.3: Epitaxy Stepwise [91]

#### 4.3.3. Hydride Vapor Phase Epitaxy

One of the most used methods of epitaxial growth is Hydride Vapour Phase Epitaxy or so called HVPE [92]. It is frequently applied in production of semiconductors like Galium Nitride, Indium Phosphide, Galium Arsenide or in making of their related compounds [92]. In the afore mentioned compound making process, a reaction between hydrogen chloride and group III metals occur at a high temperature, which results in the formation of metal chlorides, which are in gaseous form [92]. These gaseous metal chlorides then react with ammonia to form nitrides belonging to group III [92]. Various types of hydrogen and ammonia are some types of carrier gases that are used in the process [92].

Hydride Vapor Phase Epitaxy can limit the production cost in comparison with the method that is commonly used for organometallic compounds (MOCVD) [92]. Reduction in the consumption of Amonia is the major factor in cost reduction [92]. The use of a cheaper material as source material in comparison with the MOCVD reduces the capital cost on equipment due to the higher rate of growth [92]. This technique is the very first technique used for the epitaxial growth and was first adopted in 1960's [42]. A single crystal of GaN was fabricated then using this technique [92].

Hydride Vapour Phase Epitaxy (HVPE) works only in close equilibrium with two groups namely III-V and III-N semiconductor during the process of crystal growth [92]. That is to say that condensation is a reaction with fast kinetics. One observes a reactivity that is almost immediate, and an enhanced level of supersaturation of the vapor phase during the condensation process [92]. This is a unique property and the reason behind it is the use of Galium Chloride and Indium Chloride as chloride vapour precursor [92]. The dichlorination frequency of the vapour precursor is high enough to avoid the kinetics delay [92]. Growth can then be set ranging from 1 micron to 100 microns per hour, depending upon the vapour phase supersaturation [92]. Surface kinetics govern the HVPE growth [92]. This governing kinetics include gaseous precursor adsorption, decomposition of the ad-species, decomposition products adsorption, and the surface diffusion towards so called kink sits [92]. This is a beneficial property in the context of selective growth on substrates that are patterned to synthesize the objects and structures having 3D morphologies [92]. Variation in different growth parameters e.g., temperature and vapour phase composition, can be done to control the Anisotropy [92]. These variations can be pretty large in magnitude as growth rate can be varied [92]. Hence the structures are formed with novel aspect ratio [92]. The conceptual framework of vertical HVPE reactor is shown in Figure 4.4.

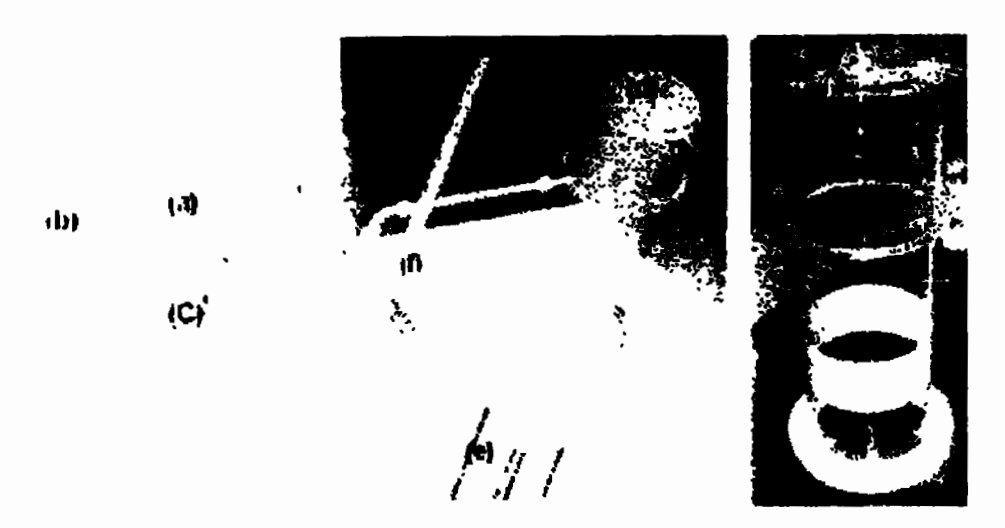


Figure 4.4: The concept of vertical HVPE reactor [92]

## 4.4 Physical Vapor Deposition (PVD)

Physical Vapour deposition (PVD) is a layer deposition technique on a substrate surface [93, 94]. Normally Thin films are deposited using this technique. Vacuum condition is used in this procedure [93,94]. There are many types of PVD, namely sputtering, magnetron sputtering, ion plating and electron beam sputtering [93, 94]. The deposited layer can vary in thickness from a few angstroms to millimetres [93, 94].

During the step one of the PVD, atoms are removed from the target material using a high energy ion source in vacuum, along with an inert gas that is usually Argon is used to knock off the atoms from the target material [93, 94]. A high energy source is provided to the target material [93, 94]. This source provided vaporize the atoms from the target surface [93, 94]. The substrate surface is placed in the chamber, and the vaporized atoms move towards it [93, 94]. If the deposited layer is metal oxide, carbide, or Nitride, the reaction occurs [93, 94]. The vaporized atoms reach the substrate are deposited there as a thin film [93, 94].

The layer generated by PVD is uniform [93, 94]. The layer generated by this technique may range from a few nanometres to the visible range [93,94]. Layers for all inorganic materials and some organic materials can be generated using this technique [93, 94]. Resistance of a low dimension is induced in PVD [93, 44]. Through a nucleation process that is heterogenous, layer

formation becomes tight [43, 94]. Consequently, it exhibits better mechanical properties e.g., hardness and wear resistance [93, 94]. The Fig. below shows the general mechanism and chamber of the PVD. The process of PVD is shown with help of a diagram in Figure 4.5 and 4.6.

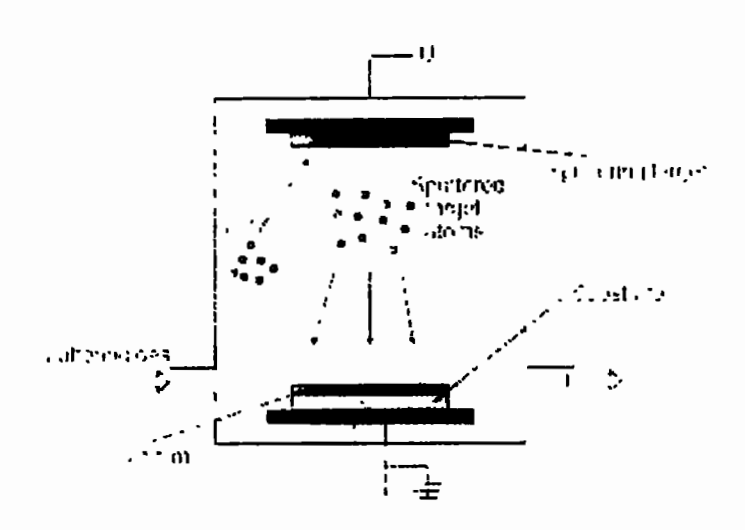


Figure 4.5: Physical vapor deposition [95]



Figure 4.6: General Mechanism of PVD [96]

# 4.5 Spin Coating

Uniform coating is done for organic materials on surfaces that are flat using spin coating [97]. Spin coating is accomplished in four steps, first one of them being deposition, the second one is spin up, spin off, and evaporation are third and fourth steps respectively, as shown in Fig.

First of all, deposition of the material on the turntable, takes place, and then is subjected to the subsequent spin up and spin off procedures in sequence while the evaporation stage occurs concurrently [97]. The applied solution is distributed on the turntable by the centrifugal force. Thinning of the layer is helped by the high spinning speed [97]. The drying of the applied layer follows. Rapid rotation makes possible the evaporation of the solvent uniformly [97]. Evaporation removes the highly volatile components from the substrate [97]. Coating solution's viscosity and the rotation speed controls deposited layer's thickness [97]. Different stages of spin coation are shown in Figure 4.7.

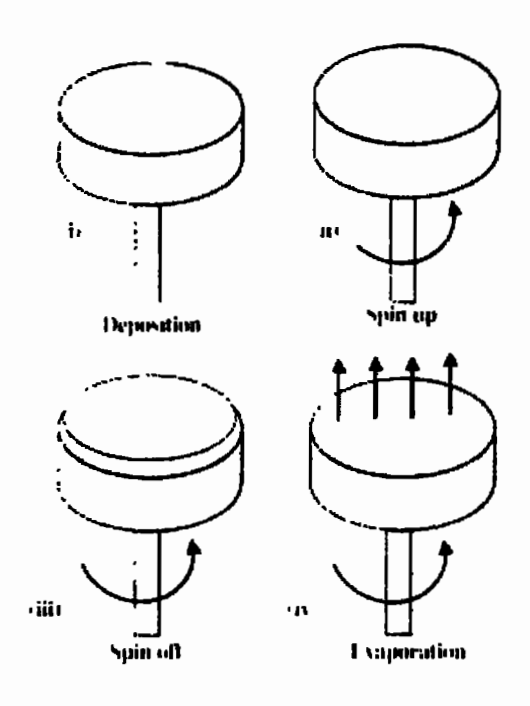


Figure 4.7: Different stages of spin coating [97]

The size of the substrate is one of the main disadvantages of spin coating. The high-speed spinning becomes difficult, with the increase in the size of the substrate the spinning at high speed becomes difficult [97]. The spin coating suffers with low efficiency of the material [97].

In general, 95%-98% of material is wasted off during the process and only 2%-5% of material is used onto the substrate [97].

# 4.6 Characterization Techniques

The characterization techniques used in this work have been discussed in this section.

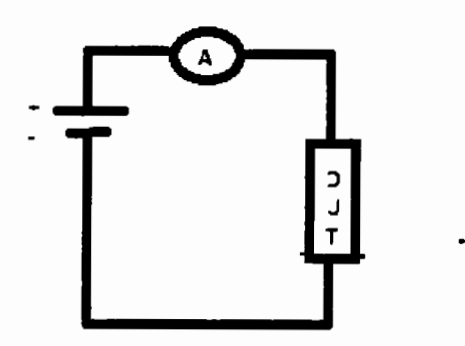
# 4.6.1 Current-Voltage Analysis

In this method, a voltage V is applied across the sample, the resulting current which can have as small value as pico ampere is sensed [98]. Activation Energies can be estimated by incorporating the effect of temperature [98]. Displacement emission or leakage could the possible reason for the resulting current [98].

The current voltage characteristics at varying temperatures reveals the activation energy, which is the energy at which is the energy at which the electrons are emitted [98]. The equation for Arrhenius Law for conductivity of the dielectric is as follows.

$$\sigma = \sigma_0 \exp\left(-\frac{E_a}{k_B T}\right)$$
 Eq 4.1 [98]

 $\sigma_0$  is the pre-exponential factor.  $E_a$  is the activation energy.  $K_B$  is the Boltzmann constant and T is the temperature.



a)



b)

Figure 4.8: a) A typical IV circuitry b) A typical IV curve

# 4.6.2 Capacitance-Voltage Analysis

In CV analysis, the capacitance is checked at various voltages and at varying temperatures, the results give an idea about the different traps present in the sample and the energy required to overcome those traps [99]. A diagram explaining the basic CV analysis is given in Figure 4.8a and b. The equation for CV is as follows.

$$C_{g_d} = \frac{\delta Q_T}{\delta v_{g_d}}$$
 Eq 4.2

Where  $C_{gd}$  is the gate to drain capacitance,  $Q_T$  is the total charge and  $V_{gd}$  is gate to drain voltage. According to this equation if gate to drain voltage  $V_{gd}$  is increased, more charge will overcome trap energy to become free carriers and the capacitance will decrease. On the other hand it will also give an idea of the trap energy or the voltage required to overcome a trap.

a)

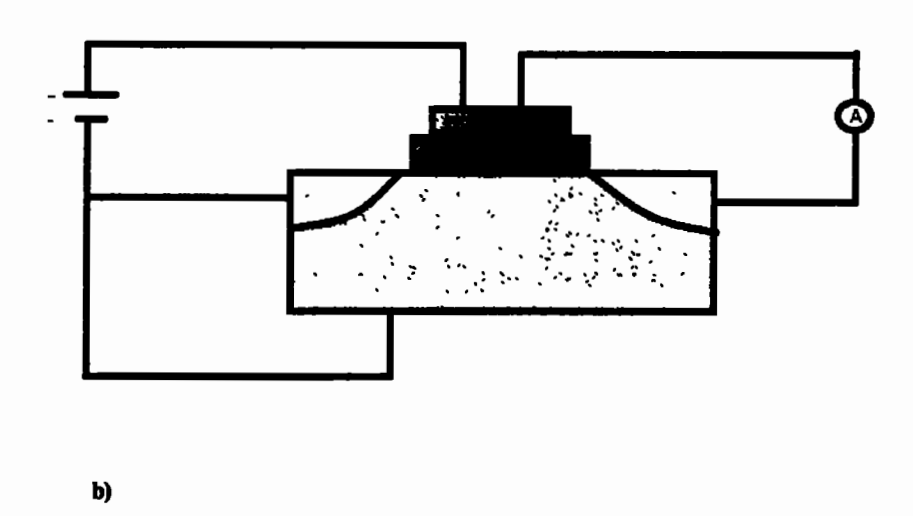


Figure 4.9: a) A CV curve b) A typical circuitry for CV [100]

# 4.6.3 Transient of Photo-Voltage (TPV)

Transient photovoltage (TPV) is a technique used to determine charge carrier lifetimes in thinfilm, and solar cells [101]. As this lifetime is often incident light intensity-dependent, its relevance to understanding the intrinsic properties of a photoactive material system as a material or device figure of merit has been questioned [101]. To extract complete information on recombination dynamics, TPV measurements are often performed in combination with charge extraction (CE) measurements, to find out the photogenerated charge carrier density and hence the recombination rate constant [101]. Figure 4.9 shows TPV and CE regimes.

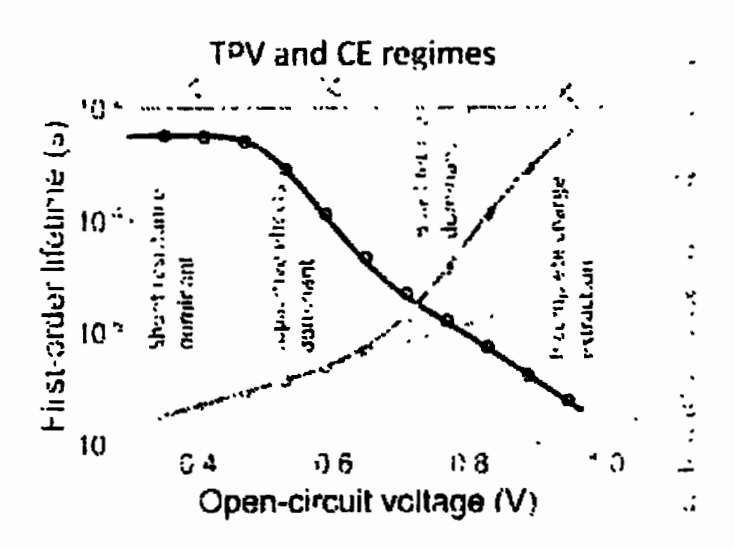


Figure 4.10: TPV and CE regimes [101]

## 4.6.4 Kinetics of Photo (Ultraviolet) and Dark Currents

In dark conditions, there is no light being shown on the sample, under these conditions, there is no light or so-called photo generated current [102]. The current will flow only when the external bias is provided [102]. This is called the dark current [102]. When the light or UV light as in our case is shown on the sample many electrons become free under the influence of incident photons and contribute towards the photo current [102]. This current may be large or small depending upon the band gap of the sample material [102]. When the light shines upon the sample, it causes some of the electrons to surmount their bandgap and jump into the conduction band [102]. If the current only flows under the influence of the incident light, it is called the photovoltaic mode [102]. But if the external bias is also provided and the incident light only contributes towards the beefing up the resultant current, then its photo-conductive mode [102]. Vacuum Ultraviolet photon detection is shown in Figure 4.10.

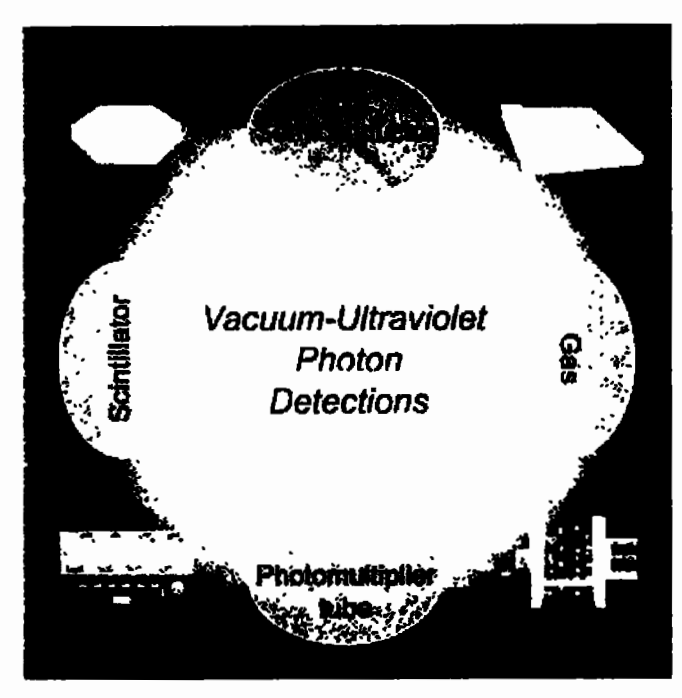


Figure 4.11: Vacuum-Ultraviolet Photon Detection [103]

## 4.6.5 Rectification Ratio (Responsivity)

The responsivity in case of a photodetector is defined as a ratio between the current generated by the light and the incident or the absorbed optical power, neglecting the noise [104]. The responsivity is determined in the linear region of response. In photodiodes, when the photon energy is above the bandgap energy, the responsivity is typically highest in that wavelength region [104]. The responsivity sharply declines in the region of bandgap due to decrease in absorption. The mathematical equation for the calculation of responsivity is given below [104].

## 4.6.6 Spectroscopic Ellipsometry (SE)

Spectroscopic Ellipsometry (SE) is a technique that is neither destructive nor interfering or invasive [105]. It bases its reading on the change in polarization state of the light obliquely reflected from a thin film [105]. Ellipsometry uses mathematical models and equations to extract the parameters like surface thickness, roughness, and many other optical parameters, like refractive index, for a thin film, from a few Angstrom to tens of microns [105]. SE can performed in two modes in-situ and ex-situ, or in satatic or dynamic mode depending upon the need of the application [105].

One of the most powerful tool for characterising the thin film systems is called spectroscopic ellipsometry (SE) [105]. SE has the capability to determine thickness of the thin film more than

any other known technique under appropriate circumstances. SE can also provide information regarding the optical parameters like surface roughness, and film's interface layer [105]. SE is resourceful tool in the investigation of optical functions of the bulk materials [105]. It performs the best for the measurement of bulk optical functions when the photon energies are greater than the band edge of the semiconductor or the insulator [105]. The useful information does not come from the measured data from SE [105]. One has to model the near surface region of the sample and then model and then fit the SE data in to the mathematical model to know the critical parameters like film thickness and optical functions[105]. The data analysis part is of great importance as if it is not performed properly, erroneous and worthless results can surface [105]. The principle of SE is shown in Figure 4.11.

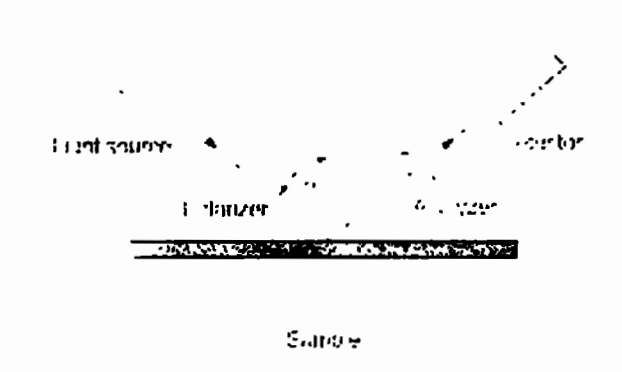


Figure 4.12: Spectroscopic Ellipsometry [106]

## 4.6.7 Scanning Electron Microscopy (SEM)

A sharply focussed beam having high level of energy of electrons is used by Scanning Electron Microscope (SEM), consequently getting a spectrum of signals at the surface of the specimen, which is solid [107]. The signals hence reflected from the sample contains information about external morphology (texture), chemical texture, structure of the crystal and orientation of materials making up the sample [107]. The data is collected from a selected part of the sample

for most of the applications [107]. An image in two-dimension is generated for the sample that contains information about the spatial dimensions of the sample. The SEM technique in conventional mode can image areas in the range of 1cm to 5 microns in width [107]. A magnification in the range of 20X to an approximate estimate of 30,000X can be achieved with spatial resolution ranging from 50 to 100 nm [107]. Selected points of the sample can also be analysed using the SEM [52]. The SEM machine works on the incident electron's energy that directly interact with the sample which ranges from 0-30keV. However the frequency component is zero because only DC voltages are applied from the cathode terminal with respect to anode ones. Chemical composition can be analysed quantitatively or semi quantitatively using this technique (using EDS) [107]. Crystalline Structure, and crystal orientations can also be found out (using EBSD) [107]. Typical process of SEM is shown in Figure 4.12.

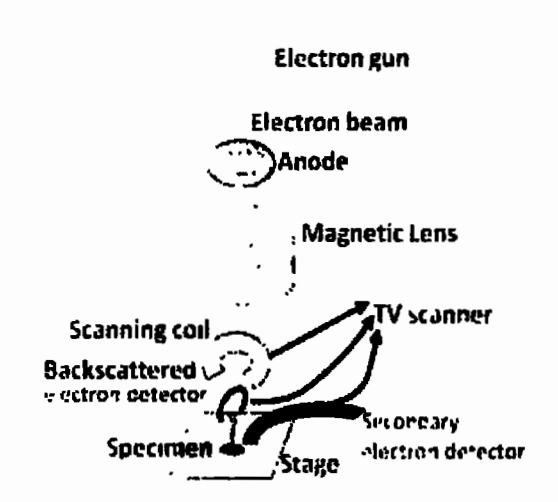


Figure 4.13: Scanning Electron Microscope [108]

# 4.6.8 Electron-Dispersive X-Ray Analysis (EDX)

The SEM-EDX and EDXRF techniques get together with each other well, for a non-destructive analysis but not all the elements that are useful can be detected [109]. Most recent developments in the field of EDXRF spectrometry, that Including the capability to alter the

geometric propertied of the instrument in accordance with the need of the excitation source and the properties of the sample, have opened up a new horizon of growth in power of this technique [109].

The standard method for the identification and quantification of elemental composition in case of very small material sample usually in the range of a few cubic micrometres. In the proper working of SEM, an electron beam excites the surface atoms such that they emit X-rays characteristic of the structure of atom of that specific element [109]. A device that discriminates among different X-ray energies or the so called energy dispersive detector is then used to analyse and discriminate between the different X-ray emissions [109]. Elements are identified from their characteristic X-rays emission and the elemental composition of the sample is known. The procedure is known as the dispersive X-ray spectroscopy or the EDS [109]. The block diagram of EDX is shown in Figure 4.13.

Figure 4.14: Electron Dispersive X-Ray spectroscopy [109]

# 4.6.9 Charge Deep Level Transient Spectroscopy (Q-DLTS)

Q-DLTS technique, which is a charge relaxation technique based on the measurements of charge transients to analyze the quantity and quality of the traps. The quantity of the traps may be of two attributes i.e. the number of trap centers (either the recombination or the generation

one) and the density of traps. The quality of the traps can be attributed towards the ability of physical attraction of the free carriers towards the said energy level energy. In Q-DLTS, initially the voltage is sustained at Vo for a particular interval to just synchronize the power supply with the device under test [110]. After this time span (charging time) the voltage bias is been drifted at some specific magnitude and this particular time span is more enough in order to perfectly charge the internal deep levels [111].

# 4.7 Summary

In this chapter different fabrication and characterization techniques have been reviewed that are mostly used in this work. Starting from epitiaxial growth and its different types, PVD and spin coating. Various characterization techniques are then reviewed such as Current voltage analysis, and the capacitance voltage analysis, Transients of photovoltage, Kinetics of photo and dark current and various other techniques including the QDLTS

Epitaxial growth basically involves a condensation of liquid gas to vapor form gas to form thin layer on a substrate. Molecular beam epitaxy is suitable for profiles having composition and doping dimension in nano-meter scale. Microchannel epitaxy involves the use of a mask to stop the propagation of dislocations in the epitaxial layer at the time of transference of lattice information. Hydride vapor epitaxy is used in the production of semiconductors like Gallium Nitride, Indium Phosphide, Gallium Arsenide or related compounds. Physical vapor deposition has many types like magnetron sputtering ion plating etc. It deposits a few Angstroms to a few mm of layer under a vacuum condition. Spin coating is a four step process for uniform coating of organic material on flat surfaces.

Characterization techniques include the current voltage analysis, which involves the introduction of a bias voltage and observing the resulting current at different temperatures to calculate different activation energies. In capacitance voltage analysis capacitance is checked

at different voltages to have an idea about the different trap centres and the energy required to overcome them. Transient of photovoltages is used to determine the charge carriers lifetime in thin films and solar cells. In kinetics of photo and dark current, current produced under zero external bias and solely under the effect of incident photons is observed under the dark and luminous conditions and when the external bias is provided the effect of dark condition and luminescent condition is observed. Rectification ratio is the ratio of current generated by incident light and incident or absorbed optical power. Spectroscopic Ellipsometry estimates morphology of a surface by analysing the change in polarization of light obliquely reflected from a thin film. In SEM a high energy electron beam reflects back from a target surface to estimate its morphology. In EDX elemental composition of a sample is estimated by observing the X-Ray emission. QDLTS is a charge relaxation technique to know about different trap centres.

# Chapter 5

## Result and Discussion

In this chapter we will discuss the details about the fabrication and characterization of the viability of atomistic scaled AlN thin films deposited over Silicon substrate. This study may provide an insight for the detection of narrow length photons for sensing purposes. The subject chapter detailed with AlN/Si matrix for photon sensing with multi-wavelength photon-detection specifically in ultra-violet regimes. The main hierarchy of this chapter has been highlighted in Figure 5.1.

#### - Main Hierarchy -

- 1- Fabrication and Characterization of AIN over Silicon Wafer
- 2- Development of Metal-Semiconductor-Metal (MSM) Structure on AIN'S for UV Sensing
- 3- Ion Implicatation of Silicon on AlN region and Development of Metal-Semiconductor-Metal (MSM) Structure on implanted AlN Si for multi-wavelength detection

Figure 5.1: Main hierarchy of Aluminum Nitride growth and characterization for UV sensing

The Semiconductor devices operate under the influence of light as phototransistor, photosensor, photo diode, photo detector and solar cell which plays a major role in the Nano/microelectronics and optoelectronic applications [113]. They have properties that can be fine-tuned for the fast-optical response, switching speed, low level of leakage current, stability and durability during the physical operation [114]. Therefore photonically oriented devices have become one of the major focus area of the scientific community. Aluminum nitride (AlN) is a direct-bandgap semiconductor with a bandgap energy of approximately ~ 6 eV, the largest among semiconductors [115]. Hence, the promise of AlN for Deep Ultra Violet (DUV) sensing applications is formidable on such level application domain [116]. AlN can also be merited for the most suitable dielectric properties, a desirable thermal expansion coefficient and for being non-reactive with the normal semiconductors [117]. Typical uses of AlN includes its use as a substrate for electronic packages, because of its good thermal conductivity, it is also used as a heat sink. Other applications include its usage as power transistor base, use in IC packages. It

is also used in microwave device packages, but the area of interest in our study would be the optical and the optoelectronic usage of the AlN [118]. As stated earlier high band gap and the high reflective index of the Aluminum Nitride makes it a suitable candidate for the optical and the optoelectronics sensing applications, with a special emphasis on the ultraviolet and the deep ultraviolet spectra [119]. In our study, a thin film of AlN was deposited on a silicon substrate. This can be done using various methods namely, pulsed laser deposition, reactive molecular beam epitaxy, vacuum arc or cathodic arc deposition, DC/RF reactive sputtering, ion beam sputtering, Metal organic chemical vapor deposition (MOCVD), and miscellaneous other techniques. Magnetron sputtering [120] and epitaxial based techniques [121] are the most commonly used techniques due to reproducibility, simplicity, ease of scaling up and low cost. The properties of the deposited AlN are a function of crystal orientation, crystal structure, microstructure and chemical composition [122] which in turn is a function of deposition condition such as sputtering power, frequency of the pulse, its duty cycle, temperature at which the growth was undertaken [123]. For applications in integrated photonics especially in Deep UV sensing modes, the AIN/Si interface plays a unique role. Thus, there is a need to extravagate this Heterogeneous junction in a more systematic manner. Thus, in this work, positive-negative potentials has been employed at AlN and Si boundaries to evaluate the polarity dependence of the subject stack. In order to do so; a series of electrical characterization experiments have been performed, to evaluate and analyze the extent of junction formation and its direct device level utilizing in terms of physical performance.

## 5.1 Fabrication and Characterization of AlN over Silicon Wafer

In this section AlN/Si based heterogeneous junction will be investigated for photonic applications. A hyperfine layer of AlN onto the n-type Silicon substrate has to be fabricated, and a detailed analysis of subject stack has been carried out by variety of techniques such as Scanning Electron Microscope (SEM), Current-Voltage (I-V), Capacitance-Voltage (C-V),

Charge Deep Level Transient Spectroscopy (Q-DLTS), Transient of Photo-voltages (TPV) and Kinetics of Dark and Luminous Currents. The occurrence of Si<sub>3</sub>N<sub>4</sub> layer at the interface of AlN and Si has been extensively studied by the electrical diagnostic approaches to identify a crucial role of the trapped charges, which may directly affect the properties and operation of whole AlN/Si stack. The optical measurements have also been performed and evidence of Si<sub>3</sub>N<sub>4</sub> layer formation at the AlN and Silicon interface, which plays pivotal role to the overall AlN/Si stack. Furthermore, the defect levels and their respective qualitative as well as quantitative analysis near the valance and conduction band edges of AlN has also been reported. The given stack has been investigated by multi-bias and switched voltage (positive/negative) routines at different active areas of subject AlN device matrix for their potential usage in Deep ultra-violet (DUV) and other photonic application.

#### 5.1.1 Fabrication of AlN over n-Silicon

In this section, we will develop a hyperfine layer onto the pre-fabricated n-type Silicon substrate. Initially the silicon wafer <111> orientation was cleaned by the standard cleaning protocols i.e., the splash of Acetone and Iso-Propyl Alcohol (IPA) followed by the deionized water. After the standard chemical cleanings, the silicon wafer was treated with the Nitrogen gas (99.99%) splash and placed into the deposition chamber using the Epitaxial technique of hydride vapor phase epitaxy (HVPE). HVPE was equipped with a horizontal open-flow hot wall reactor and resistively heated furnace as a two-zone heating system. Substrate temperature was limited to a narrow range from 800°C to 1200°C with Argon as carrier gas. The AlN was deposited at the thickness set point of about 200 nm using a reaction between aluminum chloride (formed by the reaction between Aluminum metal and HCl gas) and ammonia. The film thickness and the deposition rate were monitored (about ~0.6nm/seconds) by the Quartz crystal thickness monitor. The surface roughness of AlN was ~ <1nm RMS and the crystal orientation was 002 confirmed by XRD. Step wise schematic and cross-sectional view of

AlN/Si device is shown in Figure 5.2. This shows the complete hierarchy of the fabrication of AlN over Silicon substrate.

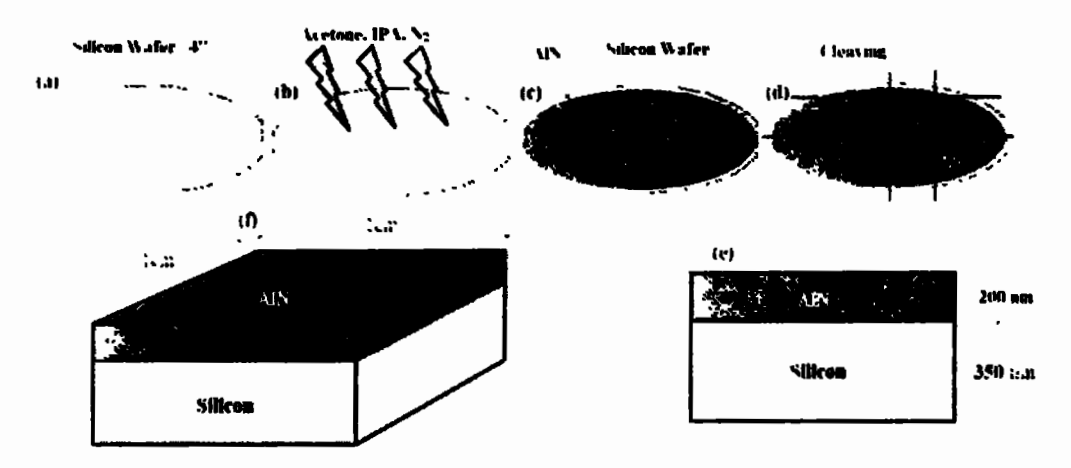


Figure 5.2: Fabrication processes of AIN/Silicon substrate; (a) Silicon Wafer, (b) Cleaning protocols for Silicon Wafer, (c) Deposition of AIN on Silicon Wafer, (d) Cleaving of AIN/Silicon Wafer, (e) 2D-view of cleaved sample, (f) 3D-view of cleaved sample

After the deposition, the portion of the device is cleaved and is first imaged through SEM to see the cross-section of the sample. The sample is mounted vertically on to the chuck using carbon tape and the images were taken using KYKY-EM6900 SEM machine as shown in Figure 5.3.

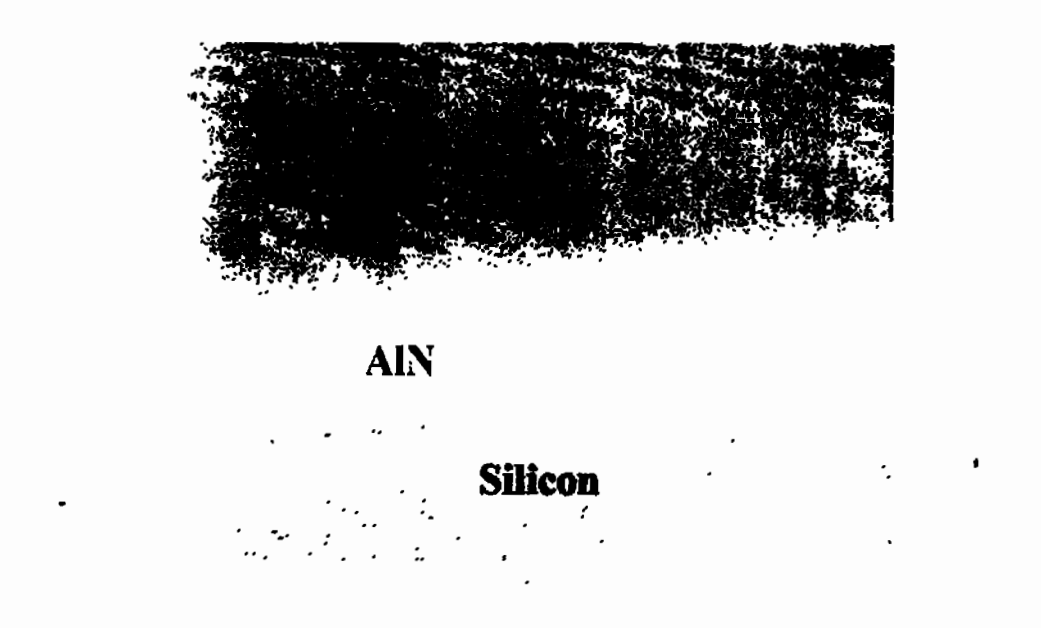


Figure 5.3: SEM image of the AIN layers on Silicon substrate

Figure 5.3 clearly shows the formation of AlN over Silicon substrate. This has also been clarified from Figure 5.3 that the fine multi-layers of AlN has been deposited on subject surface.

Existing of Si<sub>3</sub>N<sub>4</sub> layer at AlN/Si interface: When the AlN was deposited on silicon wafer, diffusion of Silicon occurs into the thin AlN layer formed and new type of interfacial layer called the Si<sub>3</sub>N<sub>4</sub> is likely to be formed with some thermo-dynamical instabilities due to the presence of defects at the AlN/Si interface [124]. Also, the lattice mismatch is about 19% between Si and AlN which is much different from each other which as a result usually produces a misfit array of dangling bonds at the interface of Si<sub>3</sub>N<sub>4</sub> and Si substrate [124, 125]. These dangling bonds act as a point defects capturing most of free carriers either photonically induced or produced through drift pump mechanism by applying input bias.

### 5.1.2 Characterization of deposited AIN

After the stack fabrication, morphological and electrical techniques such as Scanning Electron Microscopy (SEM), Current-Voltage (I-V), Capacitance-Voltage (CV), Charge Deep Level Transient Spectroscopy (Q-DLTS), Transient of Photo-voltages (TPV) and Kinetics of Dark and Luminous Currents are employed. These experimental techniques are used to study the physical dynamics of the AlN/Si junction and the role of charges/defects with within the structure for their potential utilization and exfoliation in photonic devices & systems and their subsequent performance. The electrical characterizations such as I-V, C-V, Q-DLTS, TPV and Kinetics of Dark and Luminous currents have been measured using the Automatic System for Material Electro-physical Characterization (ASMEC) system. The spectroscopic ellipsometry of the devices was performed with SENTECH-800.

One of the cleaved samples from the parent wafer as shown in Figure 5.2(f) has been further treated for the detailed examination of overall AIN stack. The subject device has been

investigated by multi-bias routines at different active areas/positions of AlN device matrix. The possible variants of different physical layers of device's matrix which were investigated are summarized in Figure 5.4.

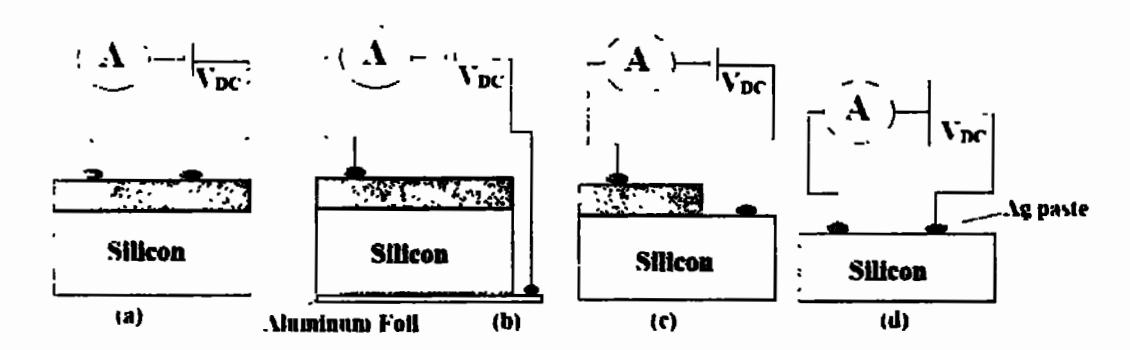


Figure 5.4: Physical schemes of electrical characterizations: (a) Top surface, (b) Top-Bottom, (c) Etched Surface and (d) Rare side (backside) Silicon

Figure 5.4 shows the overall charge based dimensional analysis from which charge is captured and sensed. Two special approaches i.e. as shown in Figure 3b and 3c, are considered to study the interface analysis of so called Si<sub>3</sub>N<sub>4</sub> layer produced during AlN and Silicon interaction. The surface area of each contact shown in Figure 5.4 was 1mm<sup>2</sup> whereas the distance between silver contacts of Figure 5.4a, 4.4c and 5.4d was ~0.25cm and for Figure 5.4b is 350.2μm.

The main origin of "charge" and "incoming photons" interaction with the AIN is mainly traced with three possible routes, as pointed out in Figure 5.4 (a, b and c). Thus, all these possible routes have to be examined in a more practical way to ascertain the device behavior at charge level. Also, the defects inside the AIN, Si substrate and the interface i.e. Si<sub>3</sub>N<sub>4</sub> [124-125] may also play a crucial role and directly affect the properties and operation of whole stack.

# 5.1.2.1 Current-Voltage Characterization

The current-voltage (I-V) characteristics of all the five given physical schemes (shown in Figure 5.4) are presented in Figure 5.5.

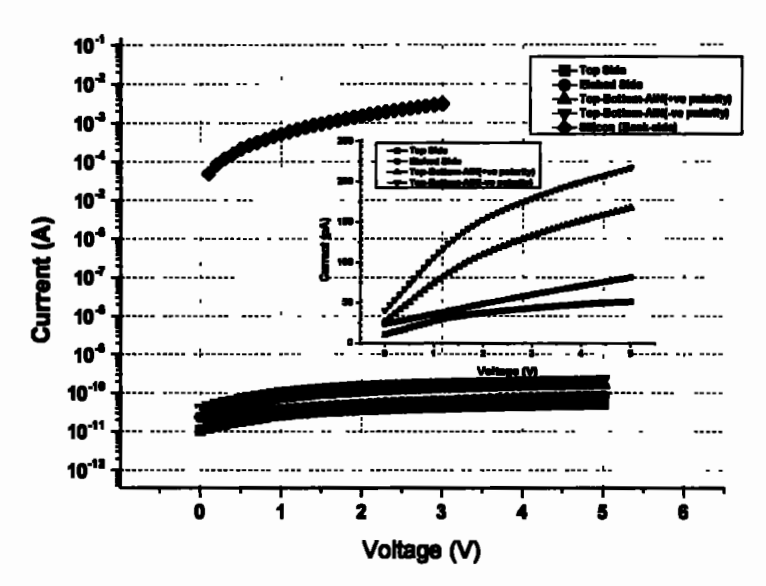


Figure 5.5: Current-Voltage characteristics of AIN stack

Figure 5.5 shows the overall response of current magnitudes as a function of applied voltage bias. This is evident from this voltage driven current technique that the maximum charges are present within the highly doped silicon side of the matrix, which is also confirmed by the Hall measurements. On contrary; only few carriers are available for all other schemes under consideration. The front window of AIN is far less conductive and provides very minute amount of free charges when sensed (shown within the inset of Figure 5.5 i.e. ~ 50pA). For the etched case (as highlighted in Figure 5.4c), the free carriers are translated from the applied bias potential and drive slightly higher current when compared with pure AlN case (Top side). From the Hall Effect analysis (Initially the silicon substrate was characterized using standard Hall Effect technique and electrical parameters required for the functionality of the device were evaluated. The sheet resistance, carrier concentration and mobility has around 11.1  $\Omega/\Box$ , 1.39x10<sup>17</sup> cm<sup>-3</sup> and 1.14 x10<sup>2</sup> cm<sup>2</sup>/Vs, respectively), this has been witnessed that the Silicon is of n-type and doped with high concentration. Thus, to properly examine the stack one needs to apply the negative and positive potentials at the top AlN layer in order to envisage the path of the charge translations, which is responsible to provide different amount of currents. Figure 5.5 shows that AlN with negative potential with respect to the bottom Silicon substrate provides

relatively larger current magnitudes possibly due to drift mechanism. The positive voltage of AlN drives relatively lesser amount of charge when compared with negatively biased approach. Although, the Silicon is heavily n-type doped; when this region is subjected to the negative voltage (positive voltage of AlN) then the so called forward bias consideration becomes dominated and may provide larger current when compared with positively charge Silicon (negative voltage of AlN). For negative polarity of Silicon (and positive voltage of AlN), lesser current is measured when compared with other counterpart. This unusual behavior is mainly due to the formation of an extra sandwich layer between the AlN and Silicon interface and the earlier studies have predicted this layer as Si<sub>3</sub>N<sub>4</sub> [124-125]. This special boundary layer is responsible for an additional charge translation between AlN and Silicon boundaries.

This behavior is further examined at the energy level scales to understand as to how much energy is needed to transfer the electronic charge within the cycle i.e. migration of charge from positive voltage to the negative voltage of drift bias source. This behavior depends on the formation of the physical junction For the purpose of this work, this behavior has been studied using Arrhenius analysis using Equation 5.1 below [126]:

$$\sigma_{s} = \sigma_{0} e^{E_{a}/KT} \qquad Eq. 5.1$$

Where, ' $\sigma_s$ ' is the conductivity at given temperature 'T', ' $\sigma_o$ ' is the conductivity at absolute temperature, ' $E_a$ ' is activation energy, 'K' is the Boltzmann constant and 'T' is the temperature in Kelvin. The Eq. 5.2 is the more detailed approach of Eq. 5.1 and from the linear approximation of Eq. 5.2 one can actually examine the activation energy 'Ea'.

$$Ln(\sigma_s) = (\frac{E_0}{K \cdot 1000}) \frac{1000}{T} + Ln(\sigma_0)$$
 Eq. 5.2

To properly evaluate the 'Ea' magnitude, one needs to calculate the conductivity magnitudes at multiple temperatures. To do so, one has chosen 300K-350K temperatures and performed

current-voltage technique on all subject cases. The current-voltage (I-V) at different temperature window of Silicon side (as represented in Figure 5.4d) is shown in Figure 5.6a.

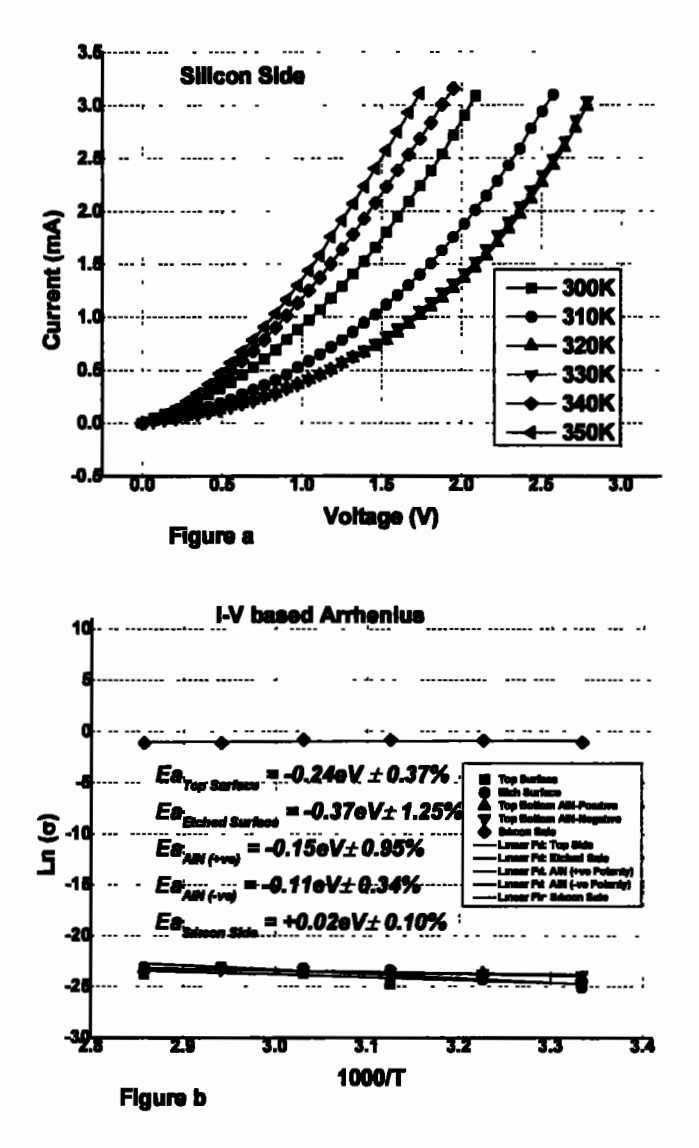


Figure 5.6: Temperature wise current-voltage analysis; (a) Silicon side Temperature wise IV analysis, (b)

Arrhenius analysis of all said cases

Figure 5.6b reveals that the highest magnitude of activation energy is of Etched surface which is  $\sim$  -0.37eV whereas the lower value is of Silicon side  $\sim$ 0.02eV. Higher the activation energy magnitude higher will be the energy needed for the conduction through subject probed points.

# 5.1.2.2 Capacitance-Voltage (C-V) Characterization

In order to sort out the reason behind the higher magnitude of current flow in positively charged Silicon side, another electrical diagnostic approach is utilized, namely the Capacitance Voltage for all the cases as shown in Figure 5.7. The voltage range of -5V to +5V have been affixed for all said cases.

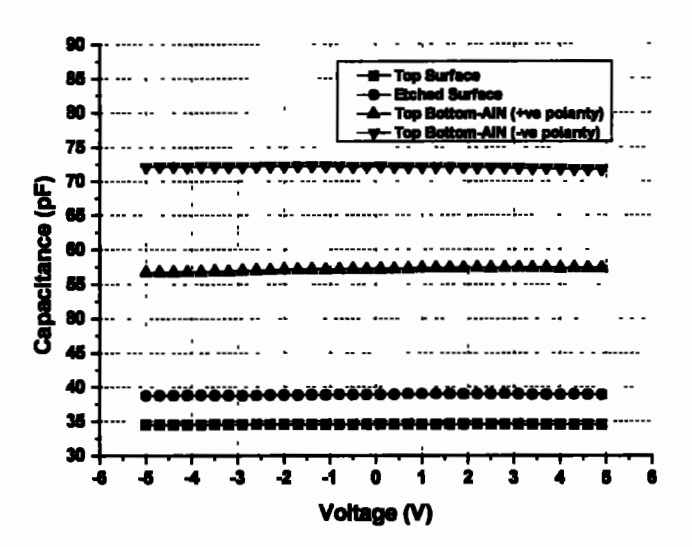


Figure 5.7: Capacitance voltage analysis of AIN stack

One can clearly observe from Figure 5.7 that the larger value of capacitance is observed from Top-Bottom cases that may be because of larger extent of physical area of subject stack. More specifically, the larger capacitance magnitude is observed for negative biased AlN. When the AlN is directed to operate more negatively bias, large number of minority carriers (positive) are subjected to move at the AlN/Silicon interface and originate a depletion region which tend to act like an insulator between negatively charged AlN and the n-type Silicon and hence large value of capacitance is observed. This is the reason with which the higher value of current was observed when silicon is operated under positive bias. Thus, the interface that has been formed at AlN and Silicon is very unique and becomes crucial for the incoming charge and photon interaction, which subsequently affects the device performance.

Xi et al. have fabricated the AlN on p-Si grown by low pressure MO-CVD technique and studied the interface of AlN/p-Si using same Capacitance-Voltage (C-V) technique. During their analysis the thickness of AlN was just 15nm and the contact diameter was ~0.25mm, under the frequency and voltage range of 50Hz-1MHz and -3V/+3V, respectively. The maximum capacitance magnitude was ~ 403pF @50Hz frequency [127]. In our scenario one has chosen an intermediate frequency of ~25kHz and the contact area was ~1mm<sup>2</sup> and the capacitance was monitored to see the columbic interaction of charge carriers at AlN/n-Si Interface and the maximum capacitance has been observed for +ve polarity i.e. ~72pF. The less value of capacitance has been observed due to thicker AIN layer compared to just 15nm AIN as reported by Xi et al.[127], i.e. thicker insulator boundaries provide lesser capacitance magnitude. As per ideal capacitance-voltage technique of Metal Insulator Semiconductor (MIS) structure, there are three fundamental regions that would be related to the charge state i.e. Accumulation, Depletion and Inversion. However, these states are merely possible for the proper impulsion of charges when they are aparted by some physical distance. For our particular cases, the silver contact acted as a metal layer, AlN acted as an insulator layer and the silicon acted like a semiconductor, thus, the structure is confined in the MIS geometry. However, proper Accumulation, Depletion and Inversion modes didn't clarified from said range of voltage. One could only examine the depletion state because for proper examination of all said charges states, the insulator (AIN) layer should be totally surrounded by the metal (Ag.). Topology in our case of miniaturized contact area is limited because one needs photonic detectivity from the AlN layer, thus, one needs larger bare AlN layer instead of total coverage by metal layer (because in that scenario, no light would interact with AIN region and photonic detectivity would not be possible). \*

## 5.1.2.3 Charge Deep Level Transient Spectroscopy (Q-DLTS) of AIN/Si

The inert behavior at AlN/Si interface has keenly been envisaged under a very powerful charge based technique named Charge-Deep Level Transient Spectroscopy (Q-DLTS). In order to map the defects at the interface, Q-DLTS technique has been utilized,, which is a charge relaxation technique based on the measurements of charge transients to analyze the quantity and quality of the traps. The quantity of the traps may be of two attributes i.e. the number of trap centers (either the recombination or the generation one) and the density of traps. The quality of the traps can be attributed towards the ability of physical attraction of the free carriers towards the said energy level energy. In Q-DLTS, initially the voltage is sustained at Vo for a particular interval in order to just synchronize the power supply with the device under test [128]. After this time span (charging time) the voltage bias is been drifted at some specific magnitude and this particular time span is more enough in order to perfectly charge the internal deep levels. For all said cases the charging time and voltage are ~ 100ms and 2500mV, respectively which is aligned with the device operational requirements generally used in DUV and other photonic applications. After passing through the charging window, the bias was suddenly removed and discharge events were monitored from the powerful integrator circuitry which recorded each discharge interval. The time based Voltage-Charge (V-Q) [129] diagram is shown in Figure **5.8.** 

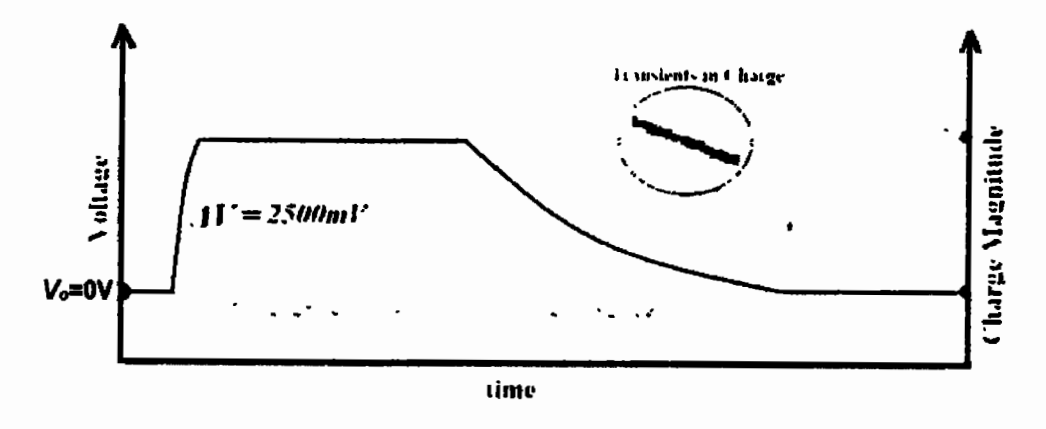


Figure 5.8: Time based voltage-charge (V-Q) diagram for Q-DLTS

During these discharge intervals time  $t_1$  and  $t_2$  are the initial and final discharge intervals. The time between these discharge intervals are kept fixed and mapped over the rate window ' $\tau$ ' and can be related as by Eq. 5.3 [128, 129, 130].

$$\tau_{\rm m} = (t_2 - t_1)/\ln(t_2/t_1)$$
 Eq. 5.3 [128, 129]

The change in these charge intervals would be related as;

$$\Delta Q = Q_2 - Q_1$$
 Eq. 5.4 [128, 129]

And,

$$\Delta Q = Q_0[\exp(-e_n t_2) - \exp(-e_n t_1)]$$
 Eq. 5.5 [128, 129]

Where  $e_n$  is the emission rate would be related as;

$$e_n = \sigma \Gamma_n T^2 \exp\left(-\frac{E_T}{kT}\right)$$
 Eq. 5.6 [128, 129]

Where, ' $\sigma$ ' is the capture cross-section, 'T' is the temperature in Kelvin, ' $E_T$ ' is the trap energy, 'k' is the Boltzmann constant, and ' $\Gamma_n$ ' is defined as:

$$\Gamma_n = 2(\sqrt{3})(\frac{2\pi}{h^2})k^2m_{\bullet}$$
 Eq. 5.7 [128, 129]

Where, 'h' is the Planck's constant and 'm.' is the effective mass of electron.

The surface trap concentration may evaluated from the highest magnitude of change in charge magnitude and can be derived from the relation below [16]:

$$N_T = \frac{4\Delta Q_{max}}{qA}$$
 Eq. 5.8 [128, 129]

Where, ' $\Delta Q_{max}$ ' is the maximum change in charge, 'q' is the universal charge constant (1.6x10<sup>-19</sup> C) and 'A' is the surface area upon which charge carriers have to be accumulated. Figure 5.9 shows the Q-DLTS spectra of each subject case.

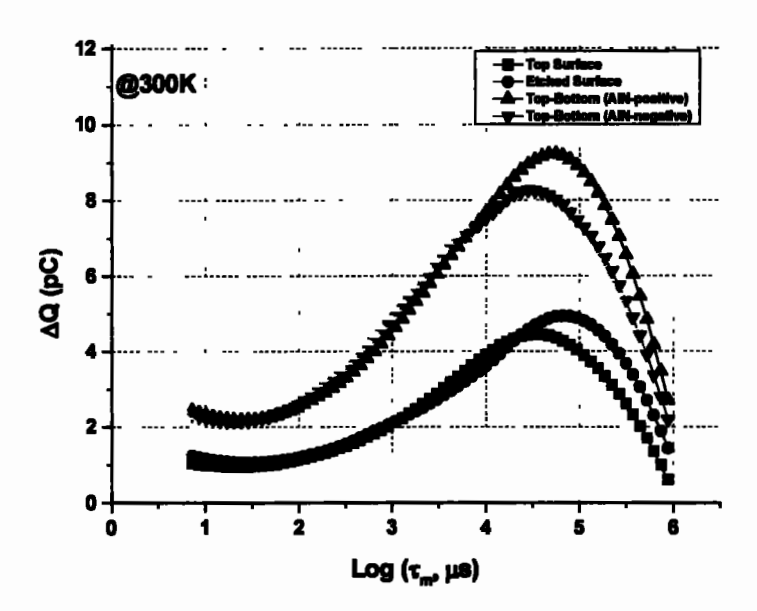


Figure 5.9: Q-DLTS analysis of AIN-Si stack

From this analysis, it becomes obvious that the Top Side of AlN has less trap densities and can be categorized as less defective due to its hyperfine crystalline nature. Whereas the trap concentration are almost double for both top-bottom stack on which AlN and Silicon makes an interface. Likewise current-voltage and capacitance-voltage analysis the Q-DLTS investigation provides an insight about the existence of depletion layer at AlN and Silicon interface (and  $Si_3N_4$ ) and the process of trap level energy scales. For the quantitative perspectives of the defects as described earlier, for higher magnitudes of  $\Delta Q$  peaks higher will be the defects densities available for the said region. AlN with positive voltage shows rather higher defect densities when compared with negative voltage schemes. This is exactly in confirmation with the results obtained from I-V (section 5.1.2.1) and C-V (section 5.1.2.2) analysis.

In order to map both of the quantitative and qualitative approaches of overall defect state, there is a dire need to characterize the subject stack under different ambient temperatures in relation to Eq. 5.6. Therefore; all cases of this stack are measured while subjected to 300K-350K temperatures. Figure 5.10 shows the Q-DLTS spectra of Top AIN surface.

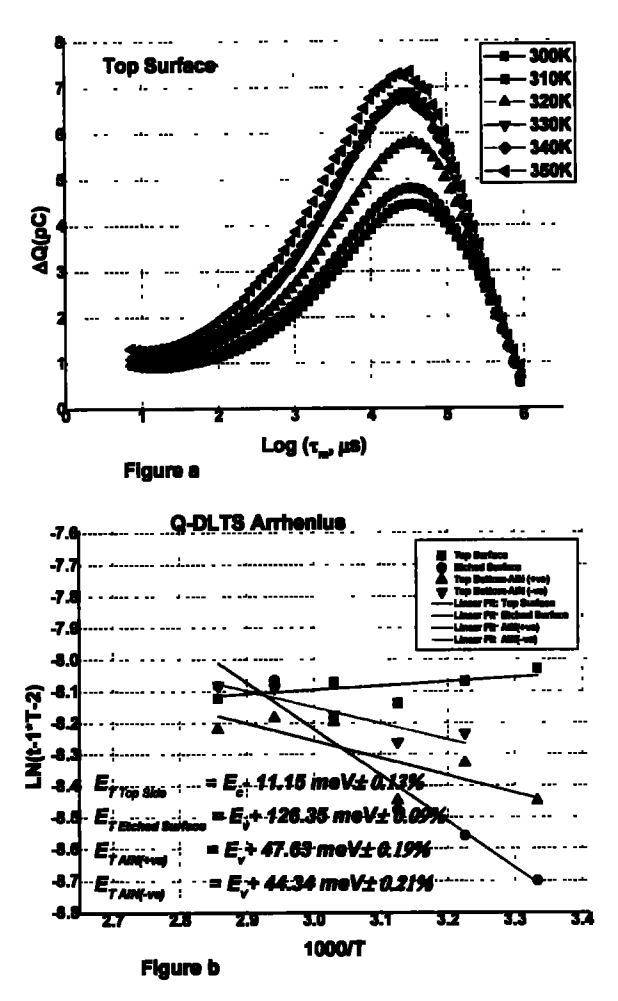


Figure 5.10: Q-DLTS analysis, (a) Q-DLTS of Top AIN surface under different temperatures. (b) Arrhenius analysis of AIN/Si stacks

From the linear approximation of Eq. 5.6 the trap energies and capture cross-section may be evaluated from the slope and intercepts. Figure 5.10b shows the Arrhenius analysis of each AlN stack and the slopes of linearly fitted lines provides the trap energies. The band picture of each aforementioned AlN stack is shown in Figure 5.11.

Figure 5.11 provides an insight of the spread of trap energies alongside the overall band gap of AlN. This has clearly been identified that Top Surface of AlN provides the generation centers because the trap location in near the conduction band edge. Thus, the top surface may play a vital role for the charge pumped to the device for a photonic activity. Whereas, all other cases are mainly recombination in nature i.e. their trap centers are located near the valance band edge. Table 5.1 provide an overall insight of each defect parameter associated with the device stack.

Table 5.1: Trap analysis of AIN-Si Stack

Condition	Temp. (K)	N <sub>T</sub> (cm <sup>-2</sup> )	Ea/ET (meV)	σ (cm <sup>-2</sup> )	
Top Side	300	1.33 x10 <sup>11</sup>			
	310	310 1.41 x10 <sup>11</sup>			
	320	1.65 x10 <sup>11</sup>	Ec-11.15	4.4 x 10 <sup>-26</sup>	
	330	1.91 x10 <sup>11</sup>			
	340 1.90 x10 <sup>11</sup>				
	350	2.12 x10 <sup>11</sup>			
	300	1.16 x10°		47 x 10-24	
Etched Side	310	1.34 x 10°	Ev+126.345		
	320	1.73 x 10 <sup>9</sup>	Ev+120.343		
	330	2.27 x10°			
	340	2.54 x10°			

	350	2.58 x10 <sup>9</sup>		
Top-Bottom AlN+ve	300	2.30 x10°		2.9 x 10 <sup>-25</sup>
	310	2.39 x 10°		
	320	3.01 x10°	Ev+47.629	
	330	3.78 x10°		
	340	4.18 x10 <sup>9</sup>		
	350 4.50 x10°			
Top-Bottom AlN <sup>-ve</sup>	300	2.16 x10 <sup>9</sup>		
	310	2.33 x10°		
	320	2.90 x10 <sup>9</sup>	Ev+44.343	2.88 x 10 <sup>-25</sup>
	330	3.55 x10°		
	340	3.98 x10 <sup>9</sup>		
	350	4.18 x 10°		

It is clearly reflected from the Table 5.1, that for AlN- $^{\text{ve}}$  case; there is comparatively lesser capture cross section ~2.88 x  $10^{-25}$  cm $^{-2}$ , which means there is lesser tendency available to capture the free carrier for its respective trap level i.e. Ev+44.343meV. Thus, incoming charge carriers can directly be collected at the nearby anode (+ve) and cathode (-ve) terminals rather than their own trap energy levels. Utilizing this approach, the cathode terminal (-ve) has already been connected with AlN surface, thus, AlN layer may also contribute into the entire band picture i.e. the trap parameters associated with AlN may also be considered for device operation. From this background one can visualize that instead of only recombination center, the generation center i.e.  $Ec-11.15 \ meV$  may also been considered when the device stack may get biased in top-bottom scheme.

## 5.1.2.4 Transient of Photo-voltage (TPV) of AlN/Si stack

To properly envisage the impact for photonic activity of the AlN/Si stack; transient of photovoltages (TPV) analysis is performed. In this analysis, a very sharp pulse of light is incident on the device for a very short time interval [131] and the decay of charge carriers are observed as function of time. During this time the transient in voltage scale occurs and rises to some steady state value and then decay of the carriers are observed. In TPV approach, the photo voltage transient at the end of light pulse consists of rapid drop followed by the slower decay. The

initial drop is due to electron hole pair recombination and the slower decay is due to carrier emission [131]. Thus, both of the centers i.e. recombination and generation are activated and contribute to their respective impact in the device operation. Figure 5.12 shows the TPV analysis of each AlN based stack.

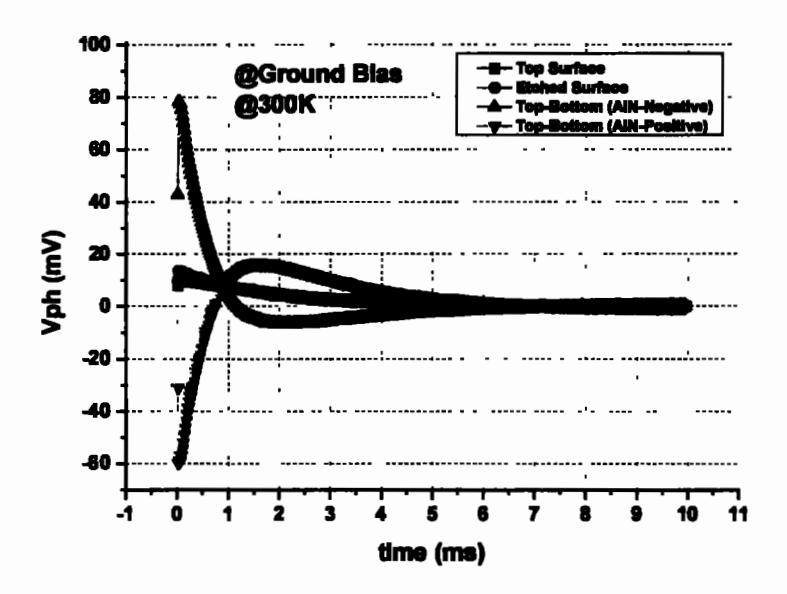


Figure 5.12: TPV measurements of AIN stack

Figure 5.12 shows the TPV analysis which also adhere that AlN-we shows larger photo voltage transients ~80mV because of higher available carrier at the AlN's associated trap center. When the decay of carriers produces the significant potential, a shift may be seen i.e. the positive voltages may get shifted to negative ones and then sustain after they fully recombine at the ground level.

For our case, the energy of the light pulse is far below the band gap of AlN, thus, only few carriers that are present only at the generation center would be activated because only 11.15meV energy is needed for their conduction. Upon conduction; recombination center may also be activated in order to nullify the impact of generated carriers from AlN. Thus, in order to nullify the impact of generation center's associated trap carriers (N<sub>T</sub>), there must be an equal amount of carriers which would recombine at other end of the probe. To do so, N<sub>T</sub> for

generation center is ~1.33x10<sup>11</sup> cm<sup>-2</sup> and nearest recombination center's trap density is about ~2.16x10<sup>9</sup> cm<sup>-2</sup> at 300K. This means that, more trap densities are required to nullify this impact which may be shared by the next available trap center. Jason B. Rothenberger et al. have worked on the surface termination of AlN under Helium Atmosphere and performed the Q-DLTS to evaluate the trap levels and capture cross sections. They have observed that Helium atmosphere localized the trap centers at 0.31 eV, 0.61 eV, 0.52 eV, 0.19 eV, and 0.40 eV and capture cross sections  $4.9 \times 10^{-21}$ ,  $1.3 \times 10^{-16}$ ,  $2.9 \times 10^{-19}$ ,  $3.1 \times 10^{-19}$ , and  $4.7 \times 10^{-19}$  cm<sup>2</sup>. respectively [132]. Y. Taniyasu et al. have been fabricated the AlN based p-n junction Deep UV LEDs (210nm), the n- and p-type region was developed by silicon and magnesium doping, respectively. The ionization energy was estimated ~630meV that was acceptor in nature [133]. In another study B. Neuschl et al. have reported the donor ionization energy of silicon into the AlN lattice of the magnitude of  $63.5 \pm 1.5$  meV [134]. The ionization energies are reported in the suggested literature [134] which were inspected by the temperature variant Photo-Luminisense (PL) spectroscopy. Whereas a charge based technique, has been applied, to evaluate the deep level donor and acceptor traps on different geometrical planes and the bias polarities (positions within the bandgap). Further; Q-DLTS in our case has utilized the temperature window ranging from 300K-350K; whereas they used temperature dependent PL in the ranges from 4K to 278K.

## 5.1.2.5 Kinetics of Dark and Photo Current on AIN/Si stack

The final approach to map the carriers for their utilization in photonic activity is the investigation of kinetics of current under two modes of operation i.e. only light is used as pumping source to the carriers and the other is the external drift voltages, respectively. This is an important feature for the photonic application particularly for the devices utilizing the UV to DUV phenomena.

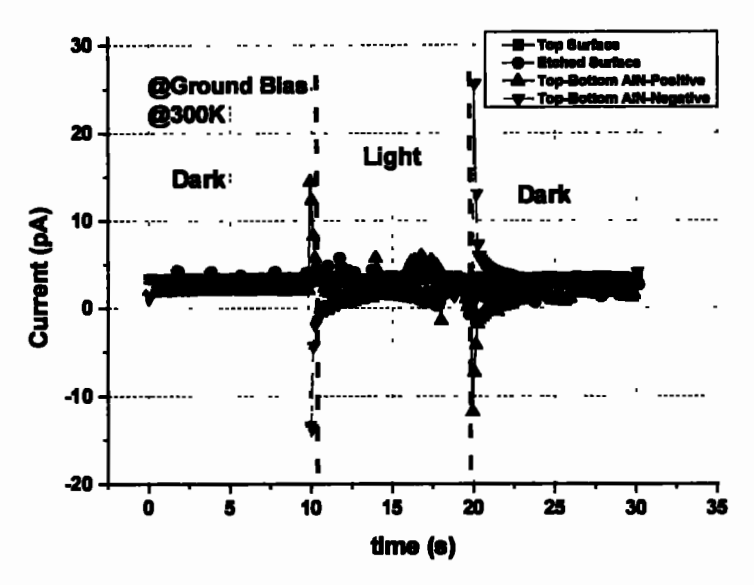


Figure 5.13: Kinetics of Current under ground biased Dark and luminous condition of AlN stack

Figure 5.13 shows two operational windows i.e. Dark and Light: in the Dark mode the AlN stack is covered by an opaque object whereas in Light mode the Ultra Violet (UV) filtered Halogen's Lamp is shone onto the device stack for ~10 seconds. However the energy of the transmitted light has been filtered by an optical filter of UV light. Thus, the output light is completely free from UV wavelengths. The highest energy that can transmit through optical source is 380nm which points out to the maximum band gap of ~3.26eV where the Silicon band gap is just ~1.12eV. Thus, these energy profiles could easily be detected by the silicon material. The UV optical filter is deliberately utilized in order to see the impact of low energy photon quanta that may only interact with the respective deep levels. This is observed that when there is a transition between Dark to the luminous mode and the vice versa, the abrupt peak in an electronic current is recorded. This is the signature that when light of sufficient energy strikes to the AlN lattice, the electron-hole pair gets generated but this pair diminishes because of the powerful recombination centers that recombine the free carriers. This is why only abrupt peak is observed rather than continuous emission of carriers from the probed region.

While in a Photoconductive mode of operation, the subject AlN stack is influenced by an external electric field and subjected to Dark and Light modes as mentioned in previous case. The kinetics of current under photoconductive mode is shown in Figure 5.14.

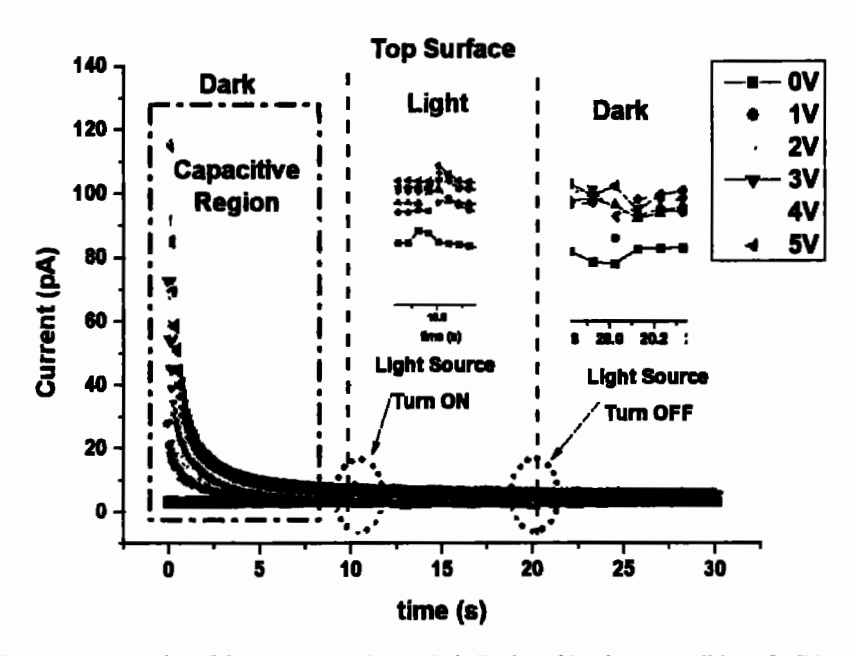


Figure 5.14: Kinetics of Current under photovoltaic Dark and luminous condition of AlN stack
Likewise the photovoltaic mode, Figure 5.14 shows the photoconductive mode of top surfaced
AlN. For all of these cases 1-5V onto the subject AlN stack are applied and current kinetics are
observed. As soon as the external bias is applied, the subject stack is accumulated by the
carriers at a certain level which is due to the capacitive nature of the stack by which the charge
has been sensed. When the Light shines and turns it into the OFF state, the same peak is
observed and during this mode the magnitude is much lesser when compared with the
photovoltaic part and can be shown within the inset of Figure 5.14. The kinetics of current
under Dark and Light mode are reported case-wise in Table 5.2.

Table 5.2: Kinetics of Dark and Photocurrent of AlN stack

Condition	Top Surface		Etched Surface		Top Bottom-AlN (+ve voltage)		Top Bottom-AlN (-ve voltage)	
	Dark	Light	Dark	Light	Dark	Light	Dark	Light
Voltage	Current	Current	Current	Current	Current	Current	Current	Current
	(pA)	(pA)	(pA)	(pA)	(pA)	(pA)	(pA)	(pA)
0	3.41	4.06	2.9	3.99	2.07	14.46	2.59	-13.72
1	5.109	5.78	3.97	6.47	5.27	21.23	6.42	-7.11
2	5.52	6.27	6.12	6.54	6.16	28.07	8.40	-10.01
3	6.12	6.74	6.91	7.15	9.41	25.26	10.27	-8.01
4	6.36	7.14	7.66	8.21	11.44	29.68	12.05	-5.20
5	6.68	7.53	8.42	9.52	11.72	28.06	14.07	0.88

# 5.1.2.6 Spectroscopic Ellipsometry (SE) on AlN/Si stack

The optical technique of Spectroscopic Ellipsometry (SE) has been utilized for DUT as depicted in Figure 5.2(e). In this this technique, the sample under examination has first been modeled in a distinct way (as-fabricated) and shown in Figure 5.15.

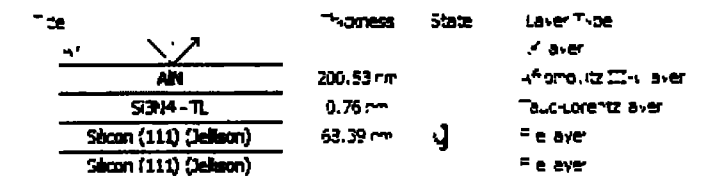


Figure 5.15: Layer wise model of the layers associated to the device under test

Numerical models associated with each respective layer provides the optical properties of said layer. For AlN,  $Si_3N_4$  and Si (111) one has chosen Afromovitz III-V layer, Tauc-Lorentz layer and standard file models, respectively. Upon choosing these standard models, it was found that the thickness of AlN,  $Si_3N_4$  and Si (111) is 200.53nm, 0.76nm and 68.39nm respectively. The thickness of AlN is cross-verified with SE as less than 1nm, which achieved in growth process. Although the thickness of Silicon (111) is mapped as ~68.39nm, however, the physical thickness of Silicon was ~350 $\mu$ m. The reason behind this abnormal reporting is the penetration of light to the actual physical layer which is limited by the larger mass of silicon i.e. the light has only penetrated at just few atomic layers of the silicon during these measurements. The

dielectric constant of each layer in a given range of wavelength has also been shown in Figure 5.16.

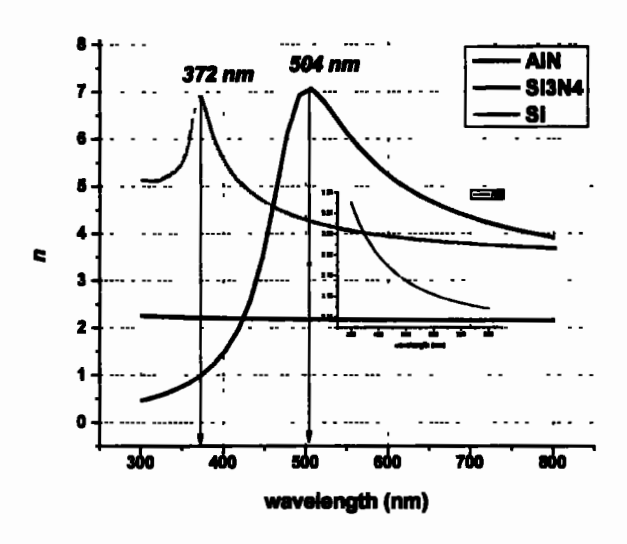


Figure 5.16: Dielectric constants of AIN, Si<sub>3</sub>N<sub>4</sub> and Si stack

Another optical constant, which is calculated by SE is the Extinction Coefficient (k) i.e. it is the measure of light lost in a given layer. Figure 5.17 shows the extinction profile of DUT in a given wavelength range. This has been observed that the extent of light lost in an AlN layer is much lesser as compared to the other layers. The in-set graph of Figure 5.17 shows that the AlN extinction coefficient linearly decreases with the increase in wavelength. Further; the maximum peak is far away (much lesser) from our given wavelength range. Within the given wavelength range utilized in these measurements, impact of the light with the matter interaction contributes to the electron-hole pair absorption in the Si<sub>3</sub>N<sub>4</sub> duly formed by AlN/Si interaction at atomic level.

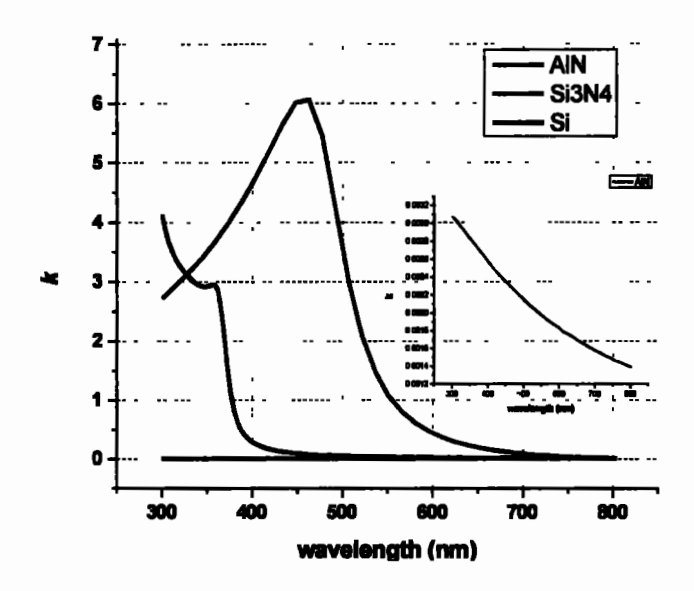


Figure 5.17: Extinction coefficients of AIN, Si3N4 and Si stack

Conclusive Remarks: In section 5.1, a fine layer of AlN has been developed onto the prefabricated n-type Silicon substrate and characterized this matrix extensively by SEM and diverse advanced electrical characterization techniques such as Hall Effect, Current-Voltage (I-V), Capacitance-Voltage (C-V), Charge Deep Level Transient Spectroscopy (O-DLTS), Transient of Photo-voltage (TPV) and Photovoltaic/Photoconductive based kinetics of photocurrent. The optical measurements have also been performed and evidence of Si<sub>3</sub>N<sub>4</sub> layer formation at the AIN and Silicon interface, which plays pivotal role to the overall AIN/Si stack. Four possible physical schemes have been developed through which the charge is pumped into the AlN stack subsequently mapped. Inspection of four trap level within the energy band picture is also presented. Effect of these traps have also been mapped on the comparatively low energy photon quanta in order to map the leakage and their physical dynamics caused by the incoming photons. The transient of photo voltage analysis shows that the AlN with negative potential is able to detect more charge carriers when compared with other charge assisted physically drift schemes. It is also concluded that photovoltaic based current kinetics are more responsive than photoconductive patterns. Whereas in photoconductive mode, the charges are first accumulated for a specific duration due to the capacitive nature of all said physical

schemes and their low energy photonic response is limited compared with photovoltaic operation. The results are important and have ramification for the potential usage of this stack for the device engineering in DUV and other photonic application.

# 5.2 Development of Metal-Semiconductor-Metal (MSM) on AlN/Si for UV Sensing

In this section we will detail the effect of 200 nm thick AIN layer fabricated by the hyperfine epitaxial growth technique of Hydride Vapor Phase Epitaxial (HVPE) onto the n-type Silicon <111> wafer. After epitaxial growth, the AlN is masked and 100 nm thick interdigitated electrodes of Silver are deposited by the atomistic scale Physical Vapor Deposition (PVD) system. These interdigitated electrodes are further examined with five possible circuit permutations with the base silicon substrate at different electric potentials. For all such cases, the Ultra-Violet (UV) light has been sensed and the extent of detection inspected by various physical parameters. Transport and Current-Voltage measurements, Arrhenius and activation energy analysis, Charge Deep Level Transient Spectroscopy (Q-DLTS) and kinetics of photo (UV) current measurements have been extensively performed to assess the suitability of the device matrix for light detection. Among all the cases; the maximum UV detection with a numerical gain of >100x has been achieved for the structure where silicon region remains at more positive potential and the respective interdigitated electrodes are placed at 0V condition. Devices subjected to a 330K temperature condition, only interdigitated configuration provides maximum UV detection with the numerical gain of ~60x at an operating potential of 60 mV. The Q-DLTS based Arrhenius analysis provides a systematic study for all device-circuit configurations under dark and illuminated conditions. Defect levels and associated capture cross sections are also identified for cases which follow the standard Arrhenius equation to map their role in the possible light detection in the device matrix.

AlN thin films can be deposited on the silicon substrate using various techniques, like CVD [135-136], molecular beam epitaxy [137], ion beam enhanced nitridation [138], laser ablation [139], and reactive sputtering [140,141, 142]. Hydride Vapor Phase Epitaxy (HVPE) has also been used for growing AlN thin films on Silicon Carbide substrate [143]. Technique used for such deposition has an impact on the properties and the utility of the device thus produced. The literature testifies that defects are produced to varying degrees using these techniques [144]. These defects can be further studied and possibly utilized. In this research, a layer of Silicon Nitride (Si<sub>3</sub>N<sub>4</sub>) was formed, at the junction layer of Silicon substrate and Aluminum Nitride thin film, and confirmed by the literature as well as the experimentation carried out on the device [145]. The device was studied using the Q-DLTS technique, with a special emphasis on the junction layer between the Silicon substrate and the AlN thin film. There were a few instances found in the literature of the application of the said technique (Q-DLTS) on the AlN thin films [146].

This study especially focuses on the possible utilization of the device for UV detection with a special emphasis on the junction layer. The device was also tested for IV analysis using different biasing configurations. Activation energies and capture cross sections were calculated for these configurations at different temperatures. This revealed the effects of temperature on different electrical properties of the device under test. The results may prove to be useful for the AlN based UV detection applications

In section 5.2, we will detail the fabrication of interdigitated electrodes by Physical Vapor Deposition (PVD) on AlN/Silicon substrate. After successful development of electrodes the said device matrix has been further investigated with a special focus of UV light detection. Current-Voltage measurements, Arrhenius analysis, activation energy analysis, charge based transient spectroscopy and kinetics of photo current measurements have been extensively performed to assess the utility of device under test for possible UV detection.

#### 5.2.1 Fabrication of Metal-Semiconductor-Metal (MSM) on AlN/Si

The interdigitated electrodes were grown using atomistic scale Physical Vapor Deposition (PVD) system (Nano Master-NTE) and used silver as a metal layer. The thinness of silver contact was fixed around ~100nm. The boat material used for contact formation was Tungsten. The electric current during deposition was ~110-115A with the ramp rate of 0.5%, whereas the pressure of the deposition chamber was ~10<sup>-5</sup> torr. The interdigitated electrodes were developed by the masking process and after successful deposition the masks were removed. The distance between two identical fringes of silver interdigitated electrodes was fixed to be ~0.5mm and the length of each fringe was about ~1.33cm. The final geometry of interdigitated electrode along with physical boundaries have been shown in Figure 5.18. After the development of silver interdigitated electrodes, the 'silver paste' was painted as the rare contact which would be used as a nominal contact for mapping the overall device structure.

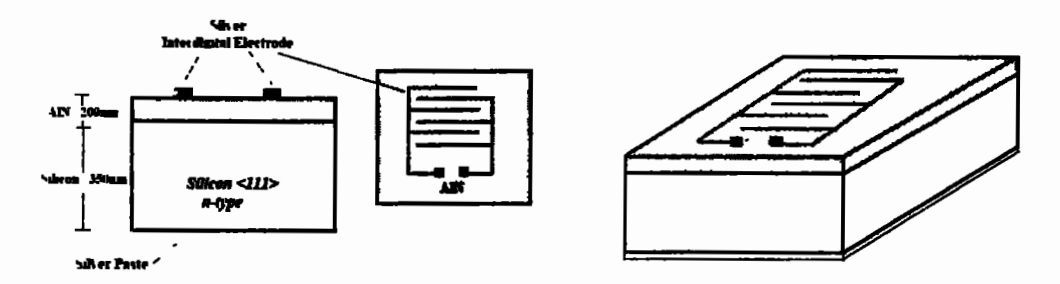


Figure 5.18: Cross-sectional view of AIN/Silicon and interdigitated electrode structure

#### 5.2.2 Characterization of MSM Structure

In order to investigate and sense the Ultra Violet (UV) light using said structure, multiple bias configurations have been developed to assess as to which configuration provides better charge collection upon the incidence of UV photons. The overall instrumental approach associated with each case has been summarized in Table 5.3.

Table 5.3: Geometrical and instrumental approach associated against each bias condition

Case	Description	Associated Geometrical Assembly
CI	Interdigitated electrodes are connected with positive and negative connection, respectively. However, the rare contact has been connected with negative supply.	
C2	Interdigitated electrodes are connected with positive and negative connection, respectively. However, the rare contact has been connected with positive supply.	
C3	One end of interdigitated electrode has been connected with positive supply, and another end is open i.e. not been connected with any supply. However, the rare contact has been connected with negative supply.	
СІ	One end of interdigitated electrode has been connected with negative supply, and another end is open i.e. not been connected with any supply. However, the rare contact has been connected with positive supply.	
C5	Interdigitated electrodes are connected with positive and negative connection, respectively. However, the rare contact has been open.	

The initial Silicon substrate was subjected to Hall Effect measurements and the values of sheet resistance, carrier concentration and mobility were found to be  $11.1 \text{ ohm/}\Box$ ,  $1.37 \times 10^{17} \text{cm}^{-3}$  and  $114 \text{ cm}^2/\text{Vs}$ , respectively. During the deposition of AlN, Silicon diffused in to the Aluminium Nitride layer and Si<sub>3</sub>N<sub>4</sub> was formed [147]. There is about 19% lattice mismatch between the silicon and the Aluminium Nitride thin films resulting in a misfit array of dangling bonds, right at the interface between the Si<sub>3</sub>N<sub>4</sub> and Si substrate as previously reported while utilizing the

same growth technique [147-148]. These dangling bonds would act as point defects, which may capture free charges during the device operation.

#### 5.2.2.1 Current-Voltage Characterization of MSM Structure

Figure 5.19 shows the I-V analysis for the five distinct configurations at room temperature i.e., 300K. One of the most salient features of this plot is the higher magnitude of the current in top/bottom case, with the polarity of silicon being positive (C4). In this particular case, UV light hinders the current flow which can be explained on the basis of polarity of the potential applied and the type of the semiconductor.

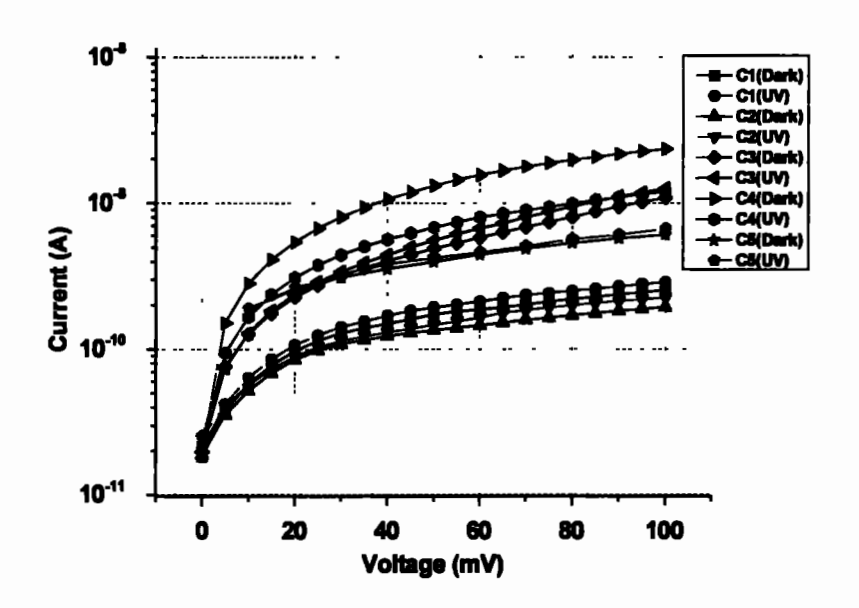
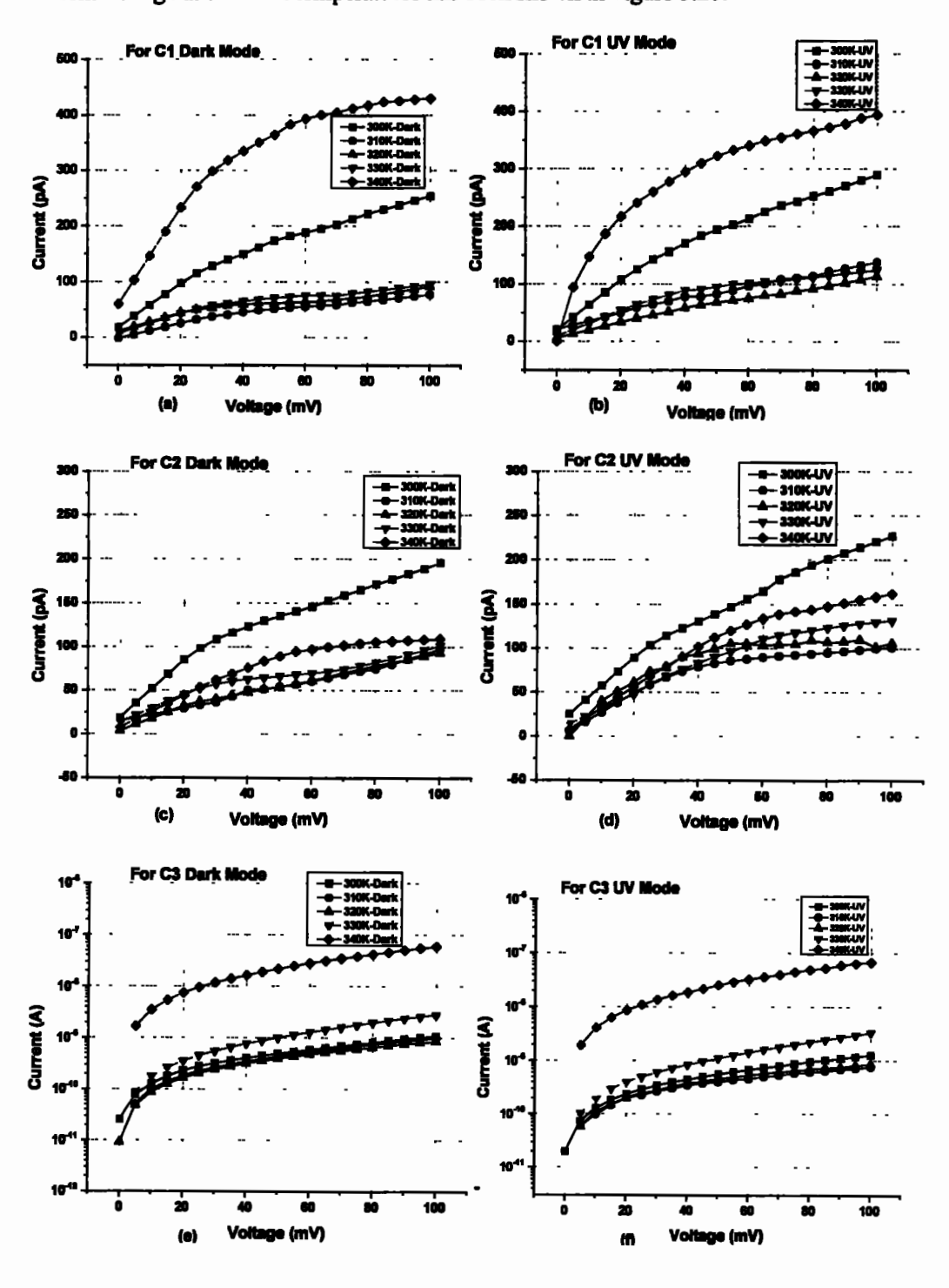


Figure 5.19: Current-Voltage analysis of AIN/Silicon structure under dark and UV-Mode

If we compare the case discussed above with the case when the Silicon's polarity is switched to negative (which constitutes a forward bias arrangement), the results are quite the contrast. In this case, namely C3, the current slightly picks up when the UV source is shone over the device. Therefore; it can be reasonably deduced that the UV light incident on the device provides additional free and mobile electrons to add additional carriers to contribute to the overall current magnitude. One of the reasons for this strange behaviour noticed in C4 and C3 is the extent of diffusion of charge carriers at the junction of Silicon and AlN as already reported in literature i.e. Si<sub>3</sub>N<sub>4</sub> formation at the interface [147-148]. To observe the extent of conduction on energy level scales, the activation energy measurements have been done using

Arrhenius analysis and shown in Figure 5.20 (k). However, the case wise representation of current-voltage at different temperatures has been shown in Figure 5.20.



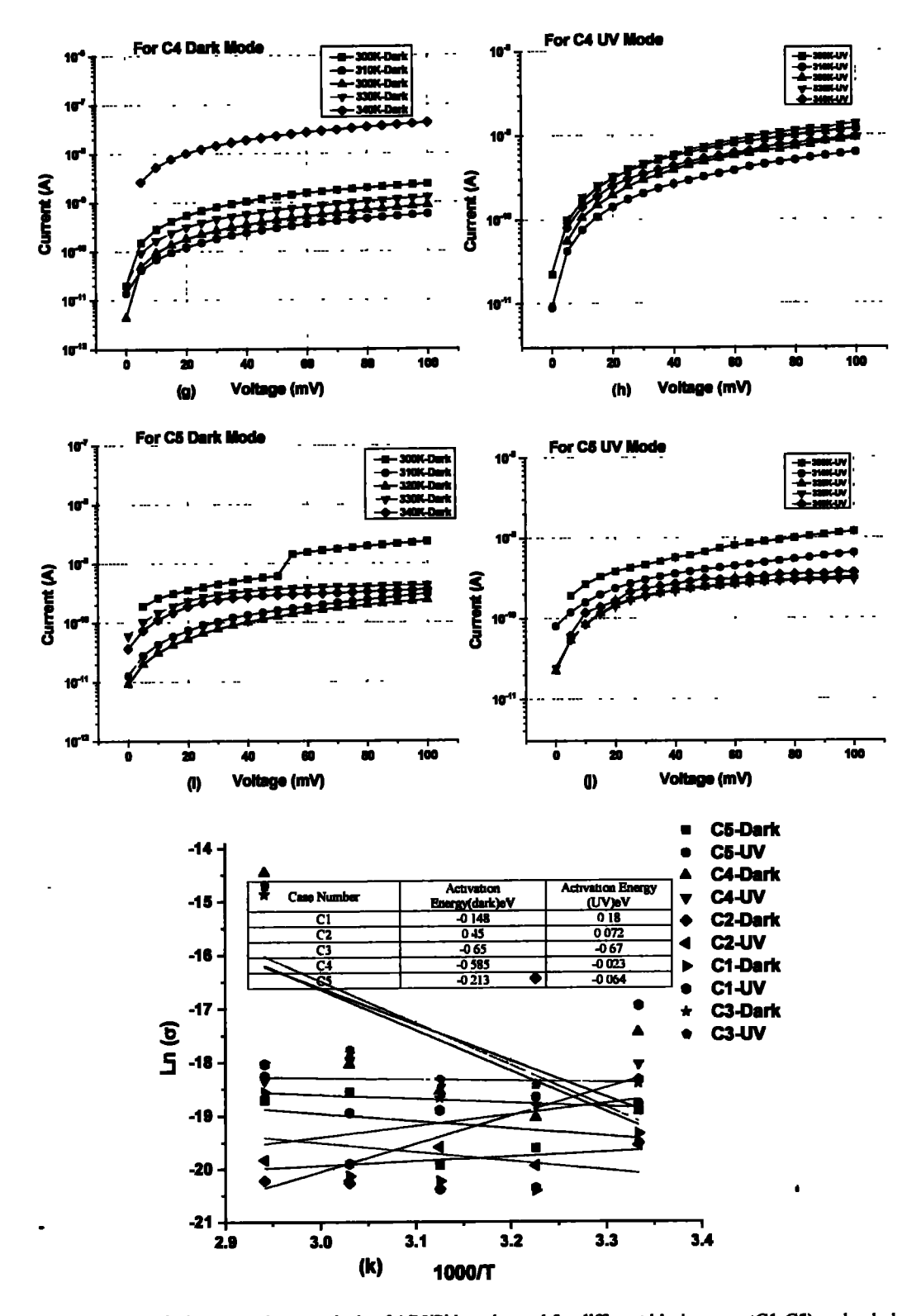


Figure 5.20: (a-j) Current-voltage analysis of AIN/Si based stated for different biasing cases(C1-C5) under dark and UV conditions (K) Arrhenius analysis based on current voltage analysis

Table 5.4: Activation Energies associated with each case

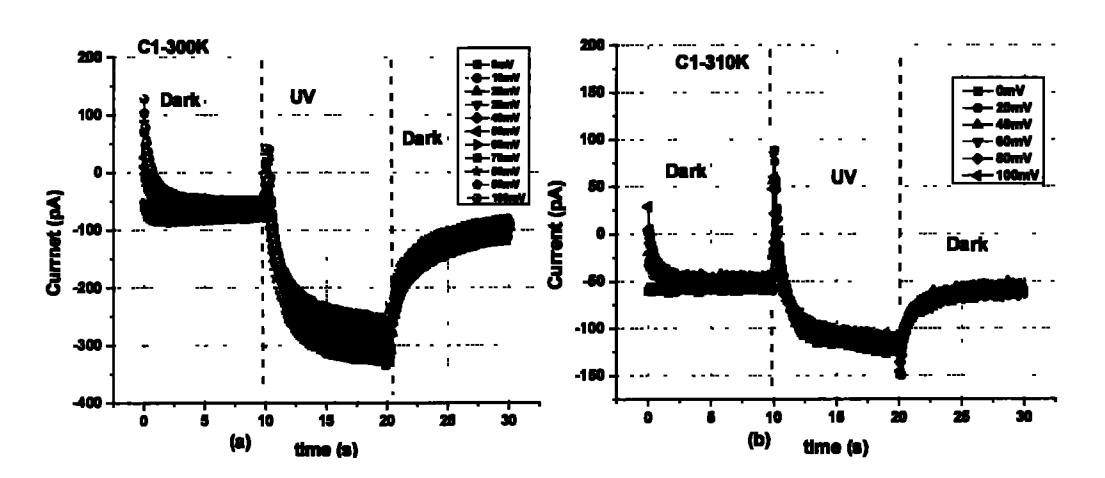
Sr.No	Case Number	Activation Energy(dark)eV	Activation Energy (UV)eV
1.	C1	-0.148	0.18
2.	C2	0.45	0.072
3.	C3	-0.65	-0.67
4.	C4	-0.585	-0.023
5.	C5	-0.213	-0.064

Table 5.4 shows the activation energies of different cases, under the dark and UV light modes. Activation energy is actually energy required to push an electron in to the conduction band. A higher value of activation energy shows that either there are traps present in the band gap and more energy is required to overcome those traps or the electron mobility is compromised due to the possible damage in the lattice. Lower values of activation energies in the light mode show that the incident photons have already energized electrons, and now lesser amount of energy will be required to push these electrons in to the conduction band. A positive sign of the activation energy shows a direct relationship between the increasing temperature and the resistance, while a negative sign shows an inverse relationship between the two. The most significant fall in the value of the Activation energy is witnessed in C4, where the value drops from -0.585eV to -0.023eV, by switching from dark to UV light mode. It means that the incident photons have considerably energized the electrons, but if already enough current is flowing in the dark mode, then additional free electrons energized by the photons might found it difficult to increase the amount of total current flow in the device. In this case, the free electrons might suffer in terms of mobility because of collisions among each other and with the host lattice. In C5, there is also a significant decrease in the value of activation energy and this specific trend shows that the sample could be useful in UV and DUV detection. In C1 and

C3, there is a nominal increase in the value of activation energy in the light mode, but that increase is negligible in comparison to the other cases.

#### 5.2.2.2 Kinetics of Dark and Photo-Current of MSM Structure

To further examine the possible extent of physical detection of the UV light, there is need to observe the said sensing mechanism under Dark and UV-Light mode of operation. In order to pursue this, one has characterized the kinetics of currents under dark and light mode of operation. The current kinetics in each case summarized in Table-5.3 have been investigated under 0-100mV at 300K-330K temperatures. In this analysis the extent of UV-detection is evaluated by the observation of current magnitudes under the specific physical condition (variation of electric potential and the ambient temperature with the calculation of the numerical gain in each case). The kinetics of dark and UV currents under 300-340K temperatures; for all said cases have been plotted and expressed in Figures 5.21-5.25 below.



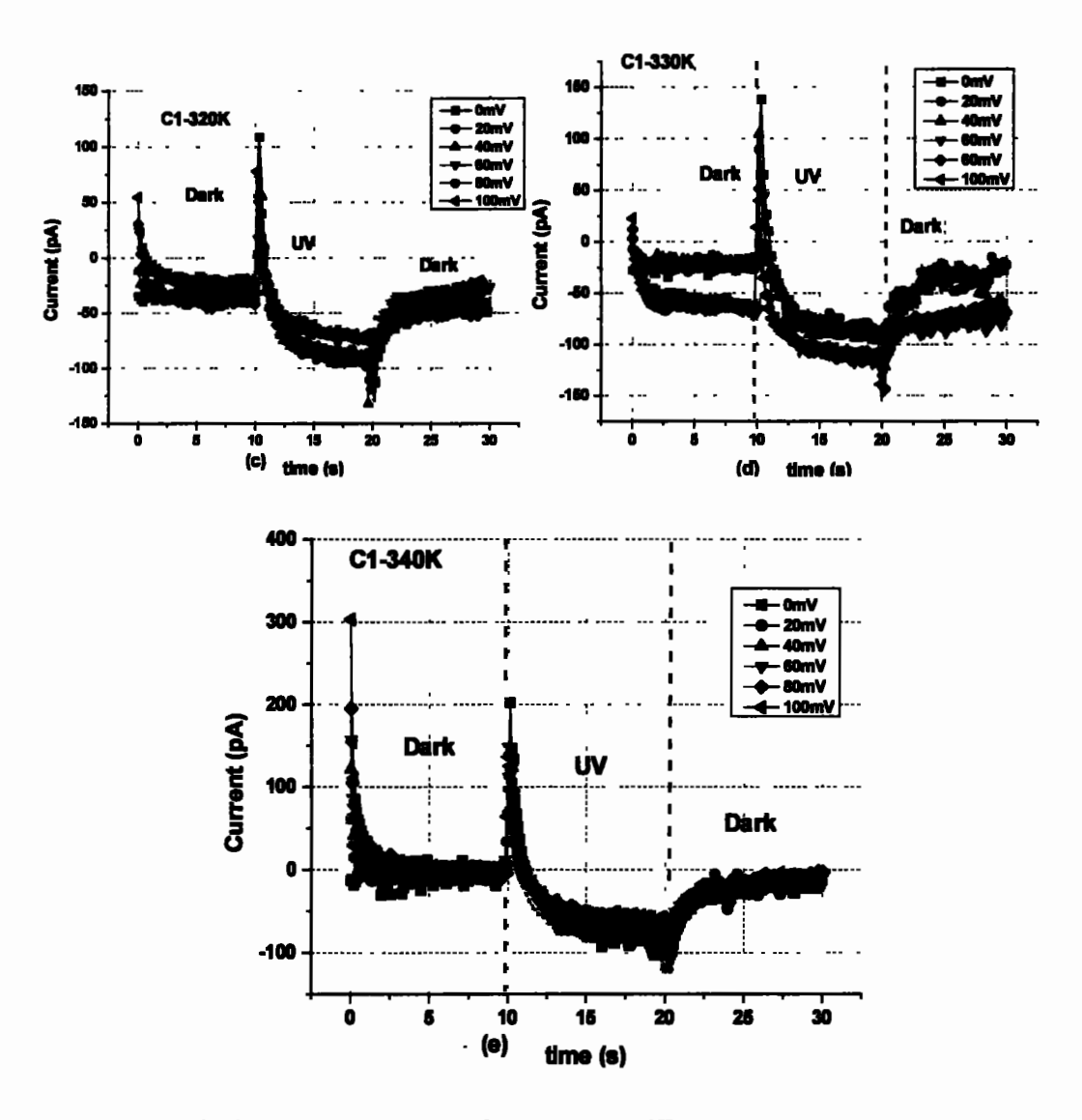
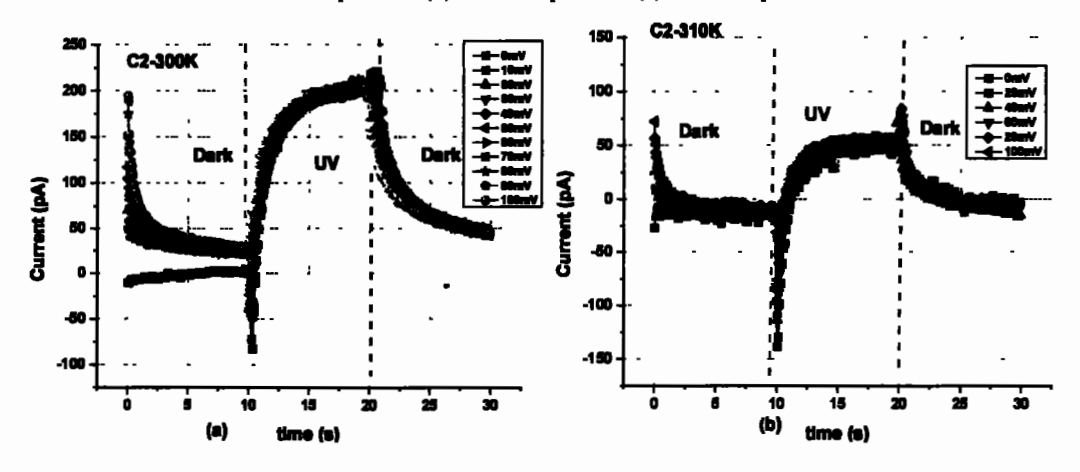


Figure 5.21: Kinetics of dark and UV current for C1 case; (a) 300K temperature, (b) 310K temperature, (c) 320K temperature, (d) 330K temperature, (e) 340K temperature



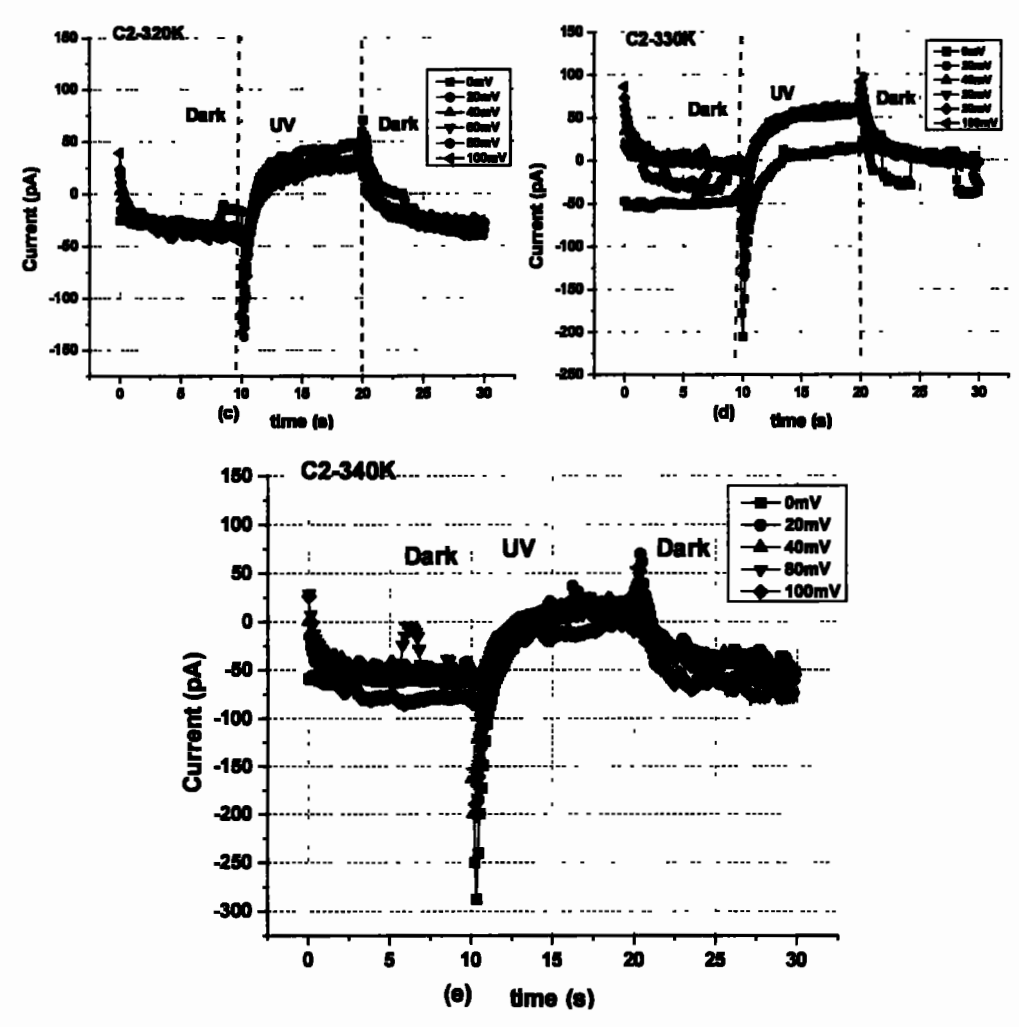
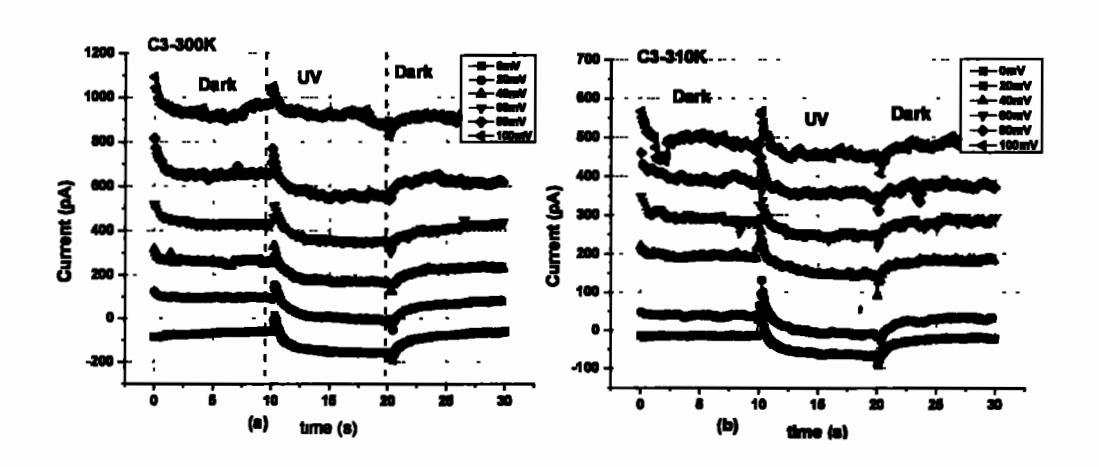


Figure 5.22: Kinetics of dark and UV current for C2 case; (a) 300K temperature, (b) 310K temperature, (c) 320K temperature, (d) 330K temperature, (e) 340K temperature



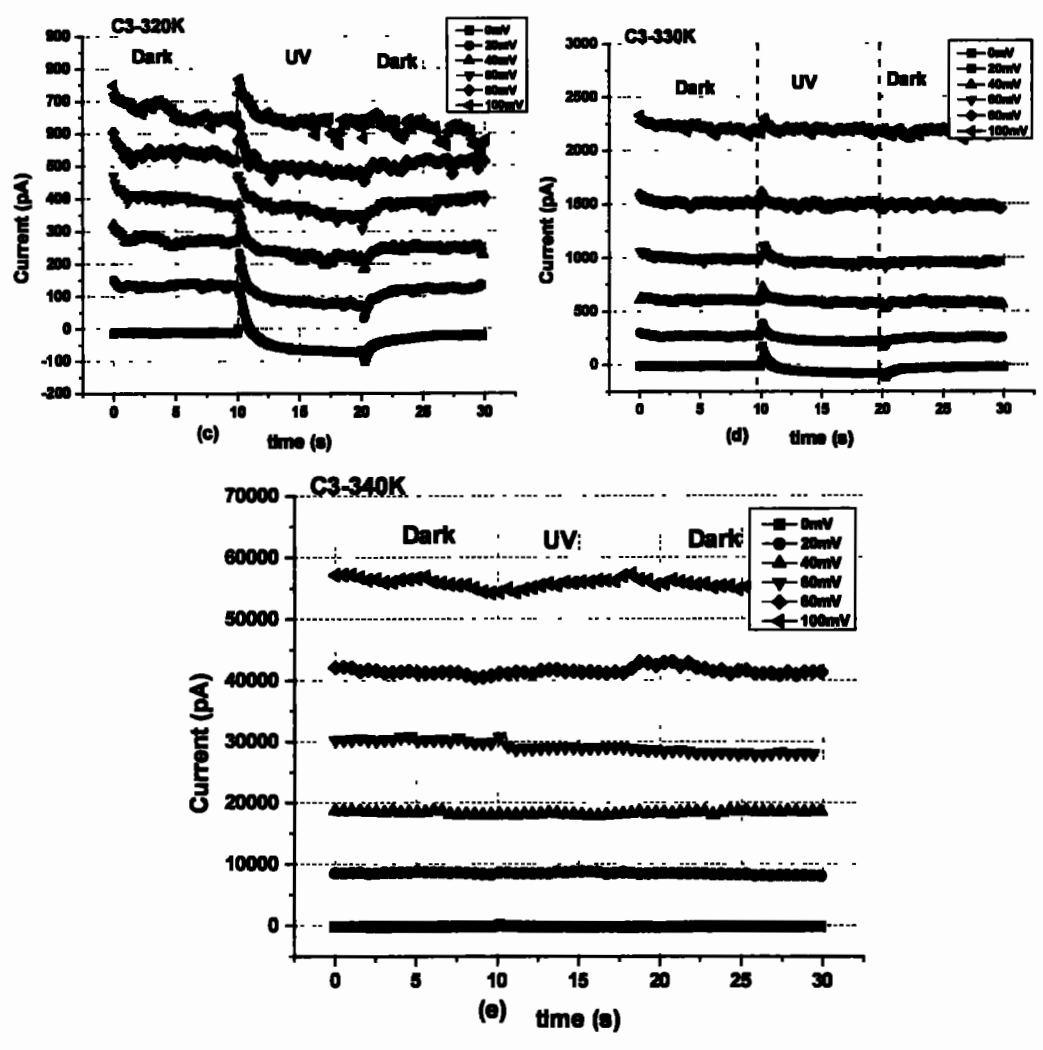
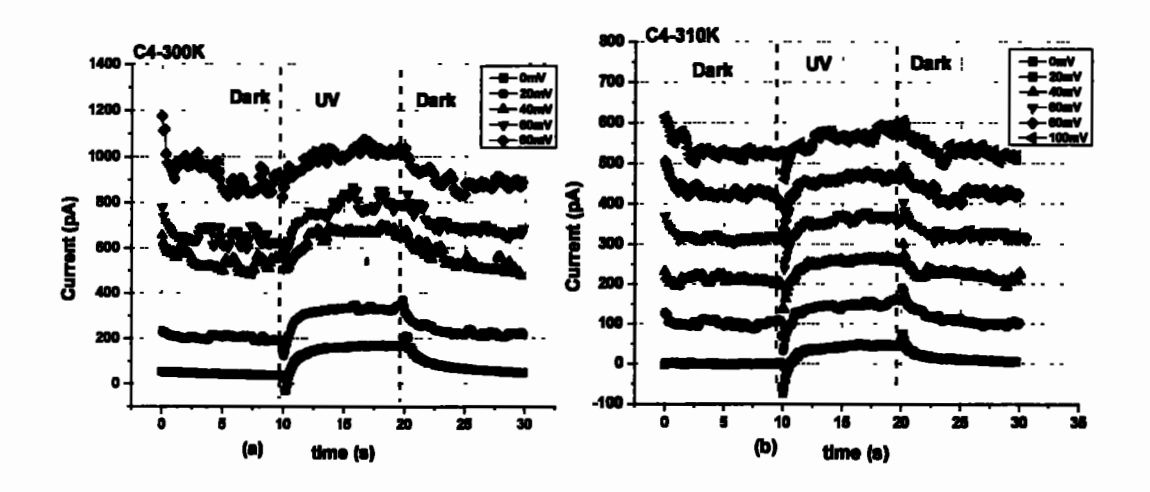


Figure 5.23: Kinetics of dark and UV current for C3 case: (a) 300K temperature, (b) 310K temperature, (c) 320K temperature, (d) 330K temperature, (e) 340K temperature



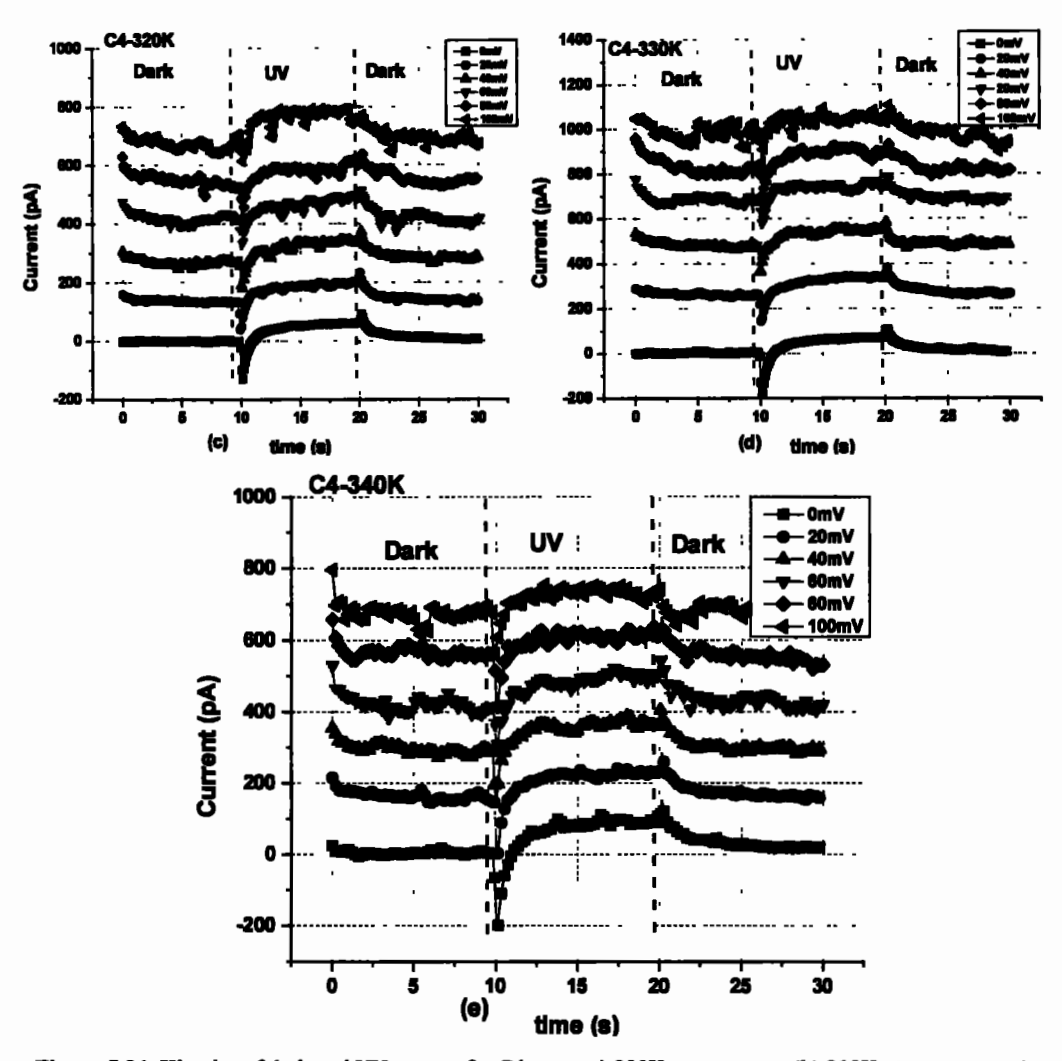
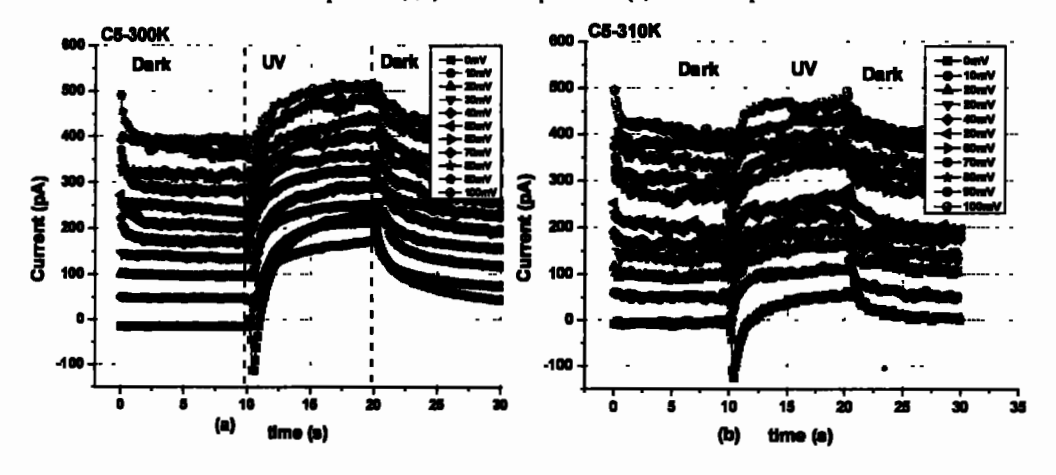


Figure 5.24: Kinetics of dark and UV current for C4 case; (a) 300K temperature, (b) 310K temperature, (c) 320K temperature, (d) 330K temperature, (e) 340K temperature



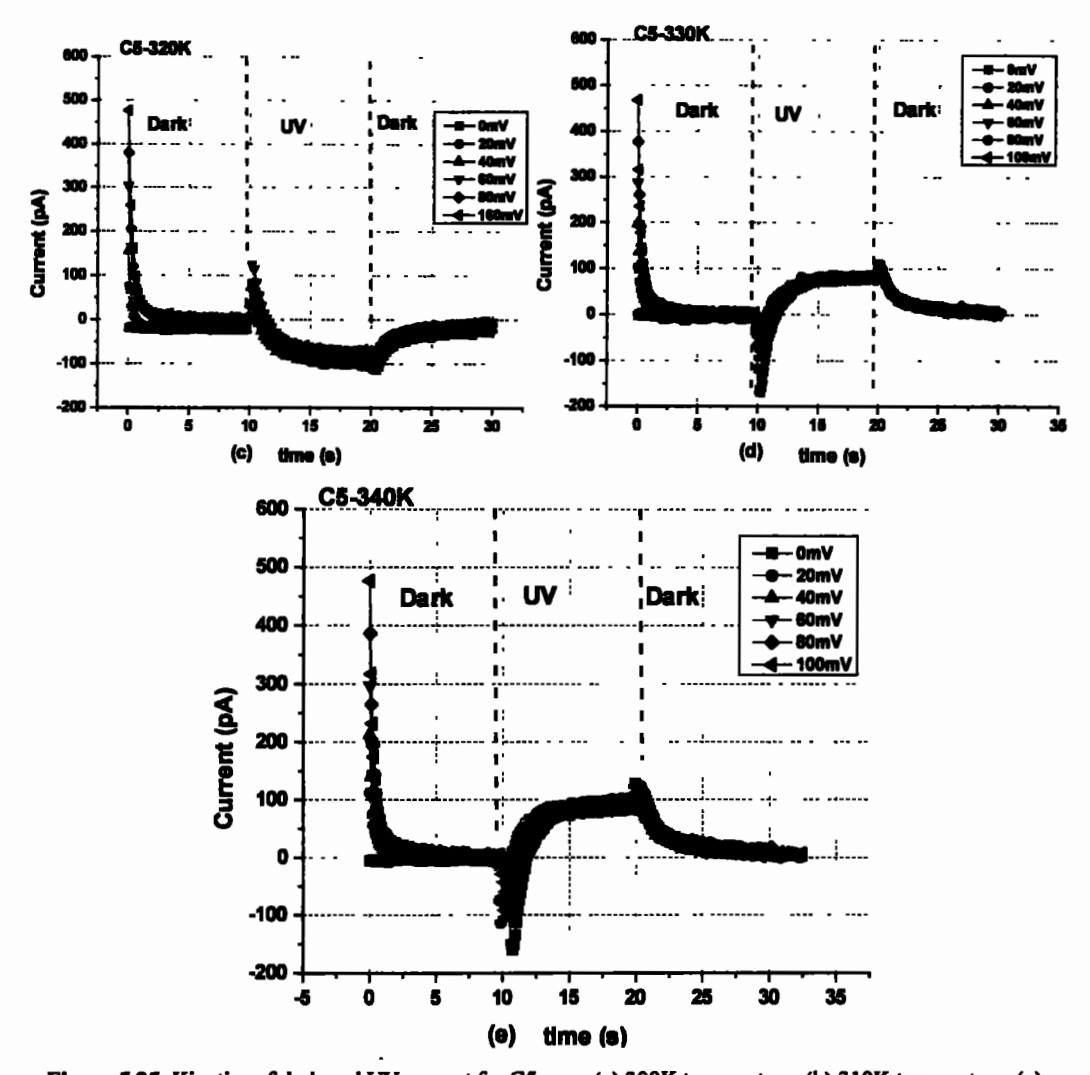


Figure 5.25: Kinetics of dark and UV current for C5 case; (a) 300K temperature, (b) 310K temperature, (c) 320K temperature, (d) 330K temperature. (e) 340K temperature

The most important kinetics of dark and UV characteristics are the 0-V conditions because in this specific case sensing circuitry needs less noise margins and said specific mode is known as 'Photovoltaic Mode'. To ensure this phenomena one have dedicatedly plotted each case against each ambient temperature. Figure 5.26 shows all said characteristics.

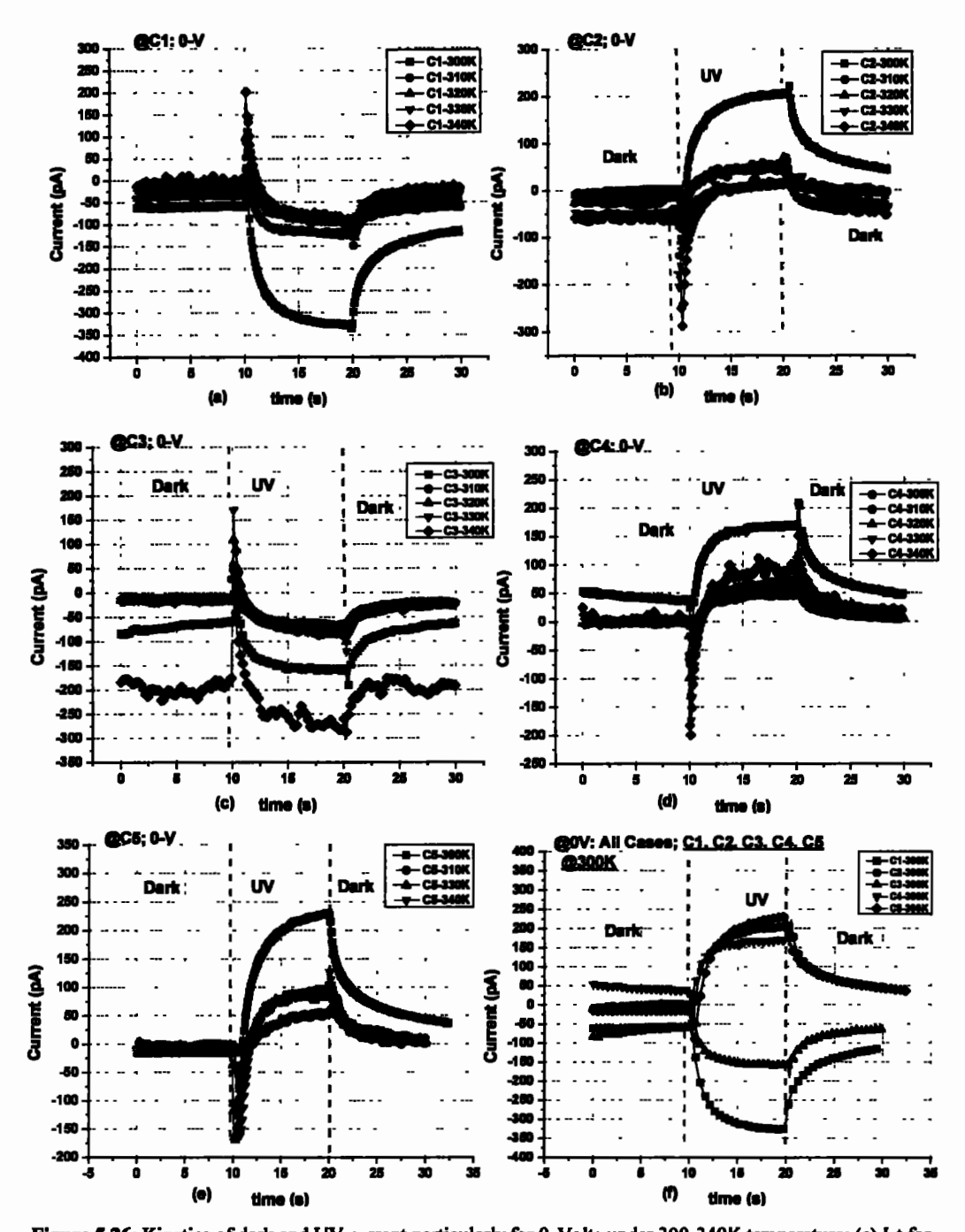


Figure 5.26: Kinetics of dark and UV current particularly for 0-Volts under 300-340K temperature; (a) I-t for C1 case at 0-Volts under 300-340K temperature, (b) I-t for C2 case at 0-Volts under 300-340K temperature, (c) I-t for C3 case at 0-Volts under 300-340K temperature, (d) I-t for C4 case at 0-Volts under 300-340K temperature, (e) I-t for C5 case at 0-Volts under 300-340K temperature, (f) I-t for C1, C2, C3, C4 and C5 cases at 0-Volts under only Room temperature (300K)

This could be analyzed from 5.26 that the room temperatures results are in more favorable patterns. For this sake one has deliberately plotted all said cases for 300K temperature and

shown in Figure 5.26 (f). From this analysis one could analyzed that Case 5 (C5) is more usable because in this mode only from AlN is monitored via MSM topology. However, other cases are also showing acceptable detection for their entire premises.

Numerical gain is the ratio of the maximum amount of current achieved in light mode to the same value in the dark mode as mentioned in Eq. 5.9.

$$Gain = \frac{UVLIght Current}{Dark Current}$$
 Eq. 5.9

Numerical gain is checked under 0V, whereby no external voltage is applied to the sample at the time when only UV-light was shone. While in photoconductive mode the device under test is exposed to the UV-light under the influence of some external bias.

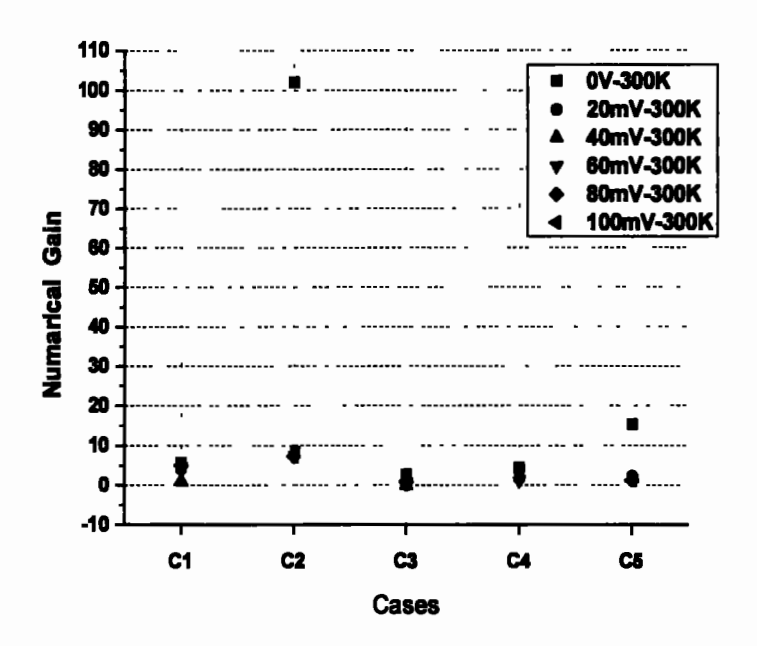


Figure 5.27: Numerical Gain of under 300K temperature

Figure 5.27 shows the value of numerical gain for all the five cases at room temperature. The value of numerical gain is much higher in C2 in the 0V condition where no external potential has been applied. The other significant gain has been observed in C5 in the same 0V mode. It can be argued that only a negligible amount of current flows at the zero bias dark condition.

Further; if a significant amount of current flows under the influence of UV-light, a significant value of current gain is observed. If we revert back to the values of the electrical activation energies i.e., Ea, we would observe that the values are the lowest in the cases discussed above i.e. C2 and C5 in the UV-light mode. The value of Ea for C2 in light mode is about |0.072eV|, while it is |0.064eV| in case of light mode of C5. This may be concluded from this analysis that the lower values of activation energies caused more electrons to be excited in the conduction band in both of these cases under UV-light source, which resulted in the higher value of current and hence higher numerical gain . It can also be observed that the value of gain remains significantly appreciable in all other cases both in the photoconductive and the 0V conditions.

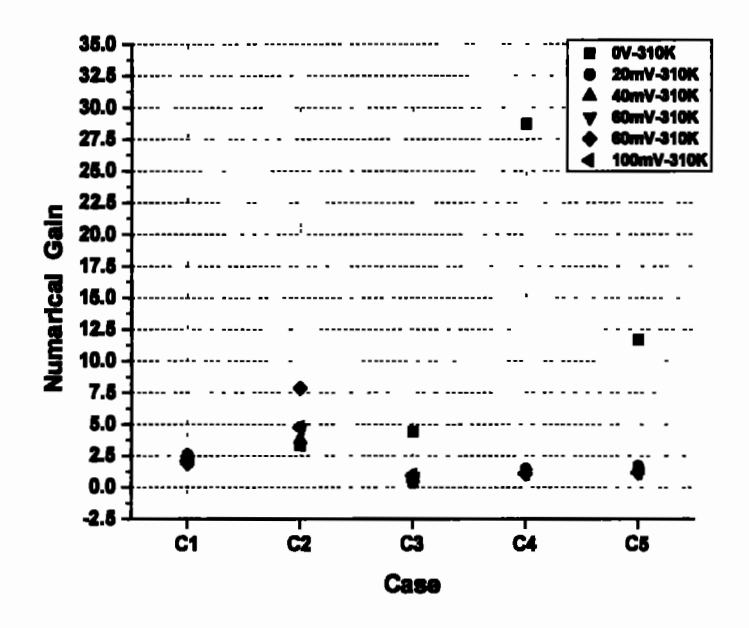


Figure 5.28: Numerical Gain of under 310K temperature

Figure 5.28 shows the response of the device under the dark and UV-light mode in 0V and photoconductive modes at a temperature of 310K. At this temperature, the highest value of numerical gain was obtained in C4 at 0V potential. The cases denoted as C3 and C5 also show large value of numerical gain in the same mode (0V). This shows that an increase in temperature has an impact on the comparative values of current in the dark and UV-light modes

in different configurations. Increase in temperature normally has an effect of increase in the current magnitude as it excites more electrons to move up to produce better conduction, but sometimes it creates damage in the lattice which could impede the flow of current. At 80mV bias potential for case C2, a significant increase in the value of numerical gain has been observed.

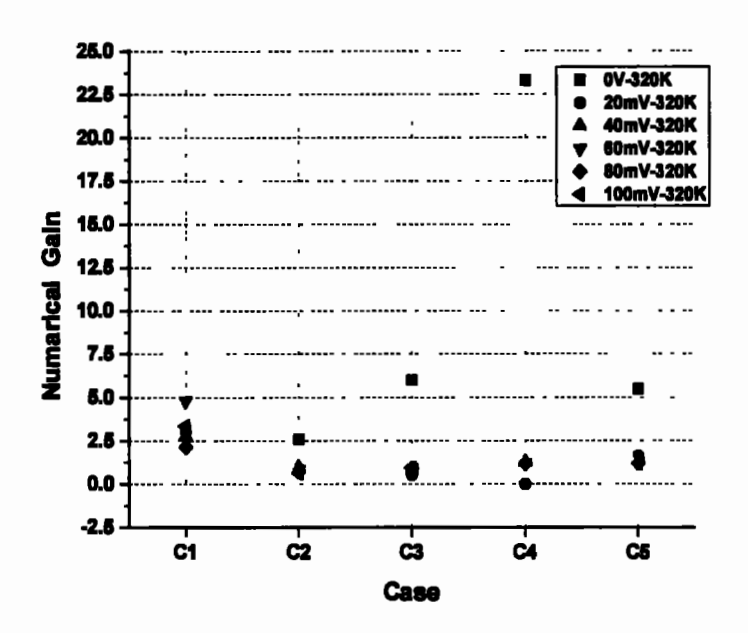


Figure 5.29: Numerical Gain of under 320K temperature

As the temperature further increases to 320K, the more damage is produced in the lattice and thus less electrons are excited. The behaviour in Figure 5.29 is almost the same as was observed in the case of 310K with the highest value of numerical gain found in C4 at the 0V while C3 and C5 showing considerable value of numerical gain in the same mode. C2 also shows a significant numerical gain in this mode. These results are somehow similar in trend with those of 310K, however, the extent of numerical gains are much lesser.

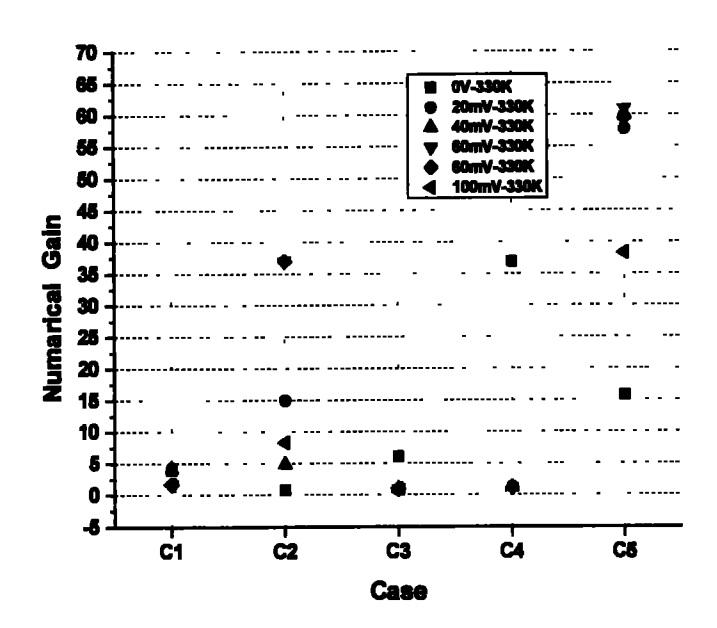


Figure 5.30: Numerical Gain of under 330K temperature

Figure 5.30 shows that the C4 again shows the largest gain in the 0V mode in comparison to other modes. We can conclude with reasonable assurance that device configuration denoted as C4 can act as an effective photo detector at temperatures above the room temperature and that too in the 0V mode. C2 can also perform the same function at the room temperature.

#### 5.2.2.3 Q-DLTS analysis of MSM Structure

In order to map the defect levels produced and their occurrence would be limited to the physical condition i.e. Dark mode, UV-Light Mode, electrical potential and the charge's physical boundary; the Charge Deep Level Transient Spectroscopy (Q-DLTS) is performed. The said technique is a charge relaxation technique that is based on the measurements of charge transients to probe the quality and the quantity of the traps. By quantity we mean the number of traps, both the recombination and the generation centres whereas the quality of traps means, its ability to attract a free carrier i.e., capture cross section. In this technique, a voltage  $V_0$  is initially sustained, for a certain time called the charging time, to acclimatize the device under test with the power supply. After the lapse of that specific time, the voltage bias is set to a

certain level for an amount of time sufficient to fully charge the internal deep levels. In our case, the charging time is 100 ms, and the voltages are varied from 10 mV to 100 mV. After the application of external bias, the charged pulse will suddenly be removed to measure the discharge events. The Voltage-Charge (V-Q) diagram against time is shown in the Figure 5.31.

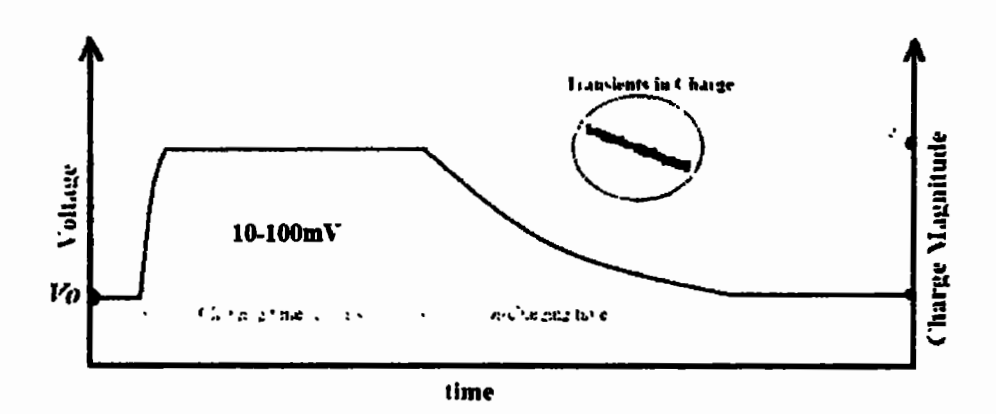


Figure 5.31: Time based voltage-charge (V-Q) diagram for Q-DLTS

The Q-DLTS analysis of each respective case at 100 mV is shown in Figure 5.31.

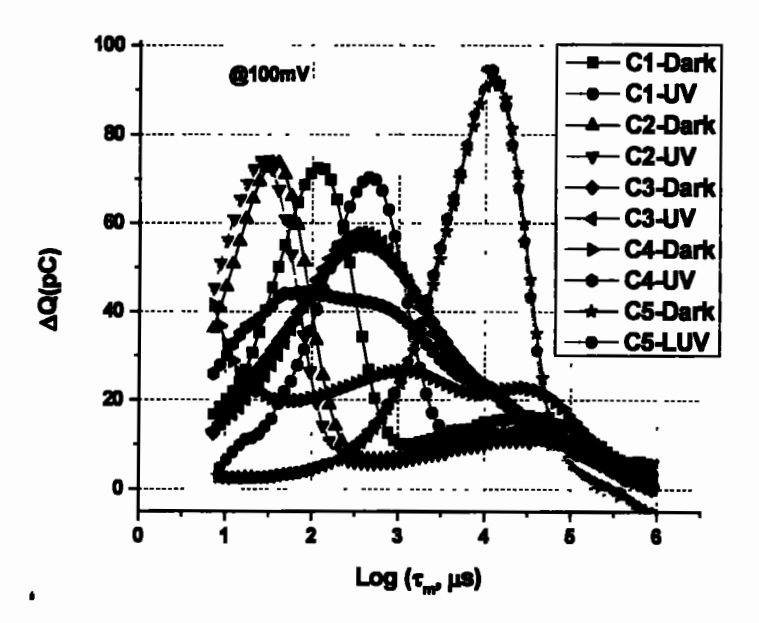
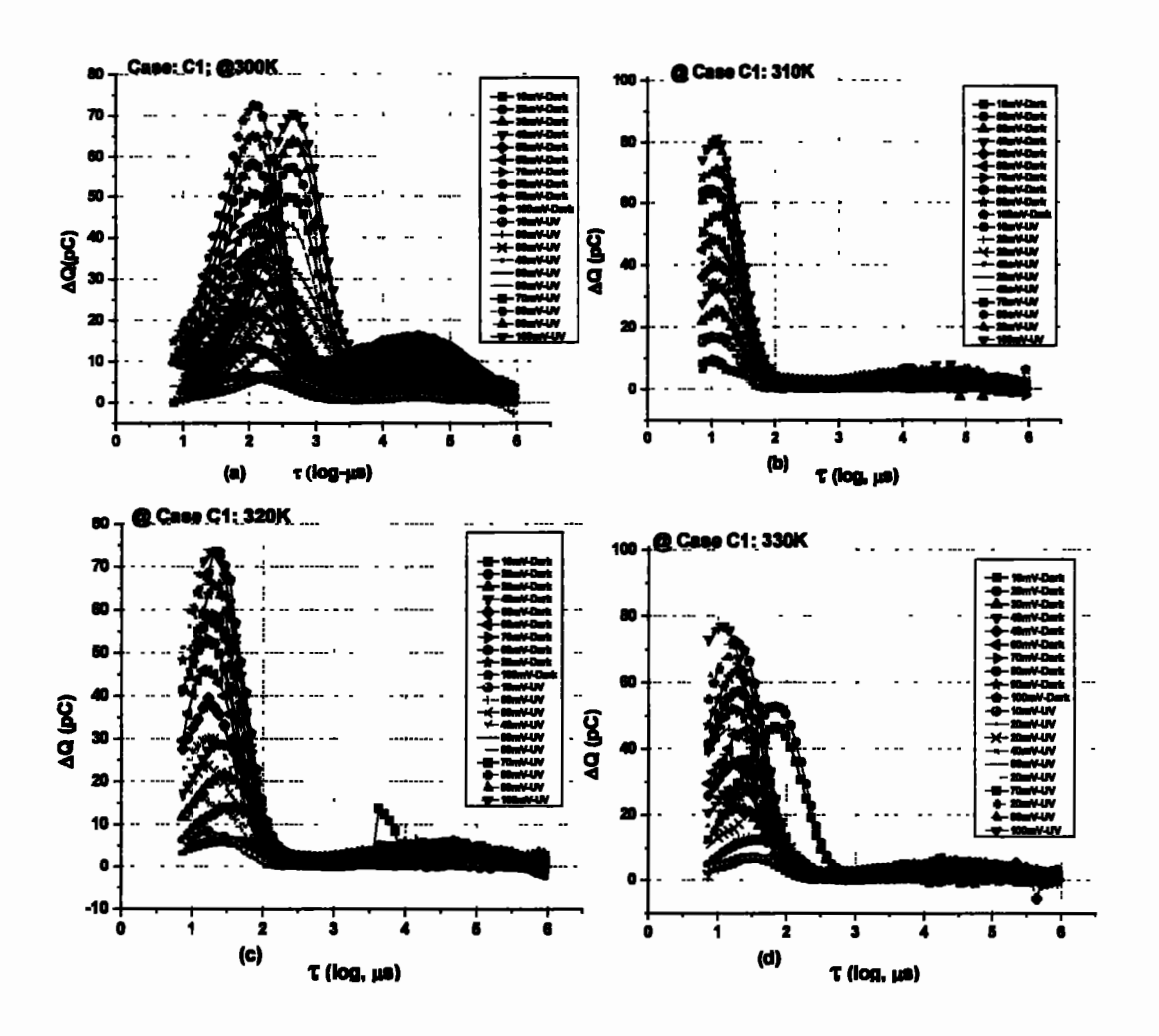


Figure 5.32: Q-DLTS analysis of AIN-Si stack against each boundary condition/configuration

Figure 5.32 shows the Q-DLTS spectra at 100 mV applied potential. This has been witnessed
that each boundary condition/configuration projects different discharge characteristics. C5,
however, is the most favorable case which affects least in change in the charge magnitude. C1

and C4 cases project maximum change in the dark and UV modes which directly points to the significant change that provides maximum UV detection under said conditions.

For Arrhenius based analysis each case would be discreetly scanned at a given temperatures and bias potential as mentioned in V-Q curve Figure 5.31. The case wise Q-DLTS analysis has been plotted in Figure 5.33-5.37 for Case\_1-Case\_5, respectively.



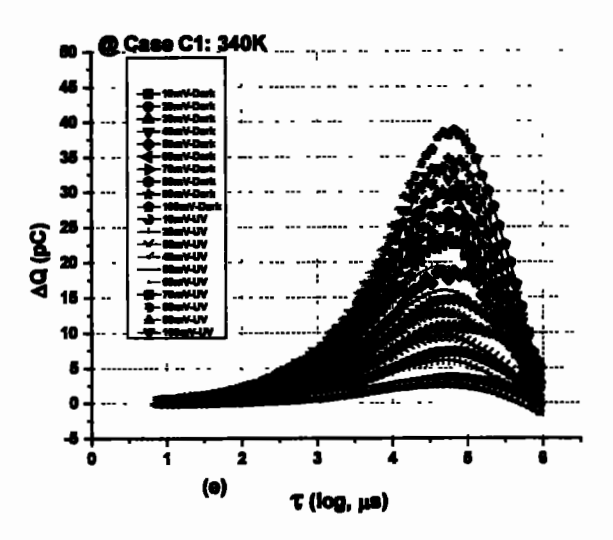
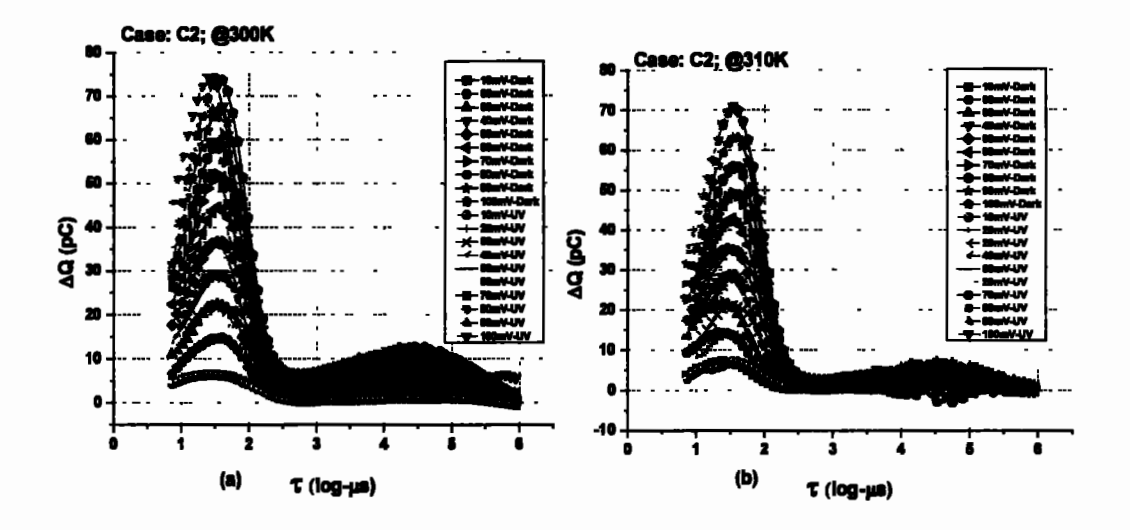


Figure 5.33: Q-DLTS analysis of Case C1 under multiple bias sequences ranging from 10-100mV (a) 300K temperature, (b) 310K temperature, (c) 320K temperature, (d) 330K temperature, (e) 340K temperature



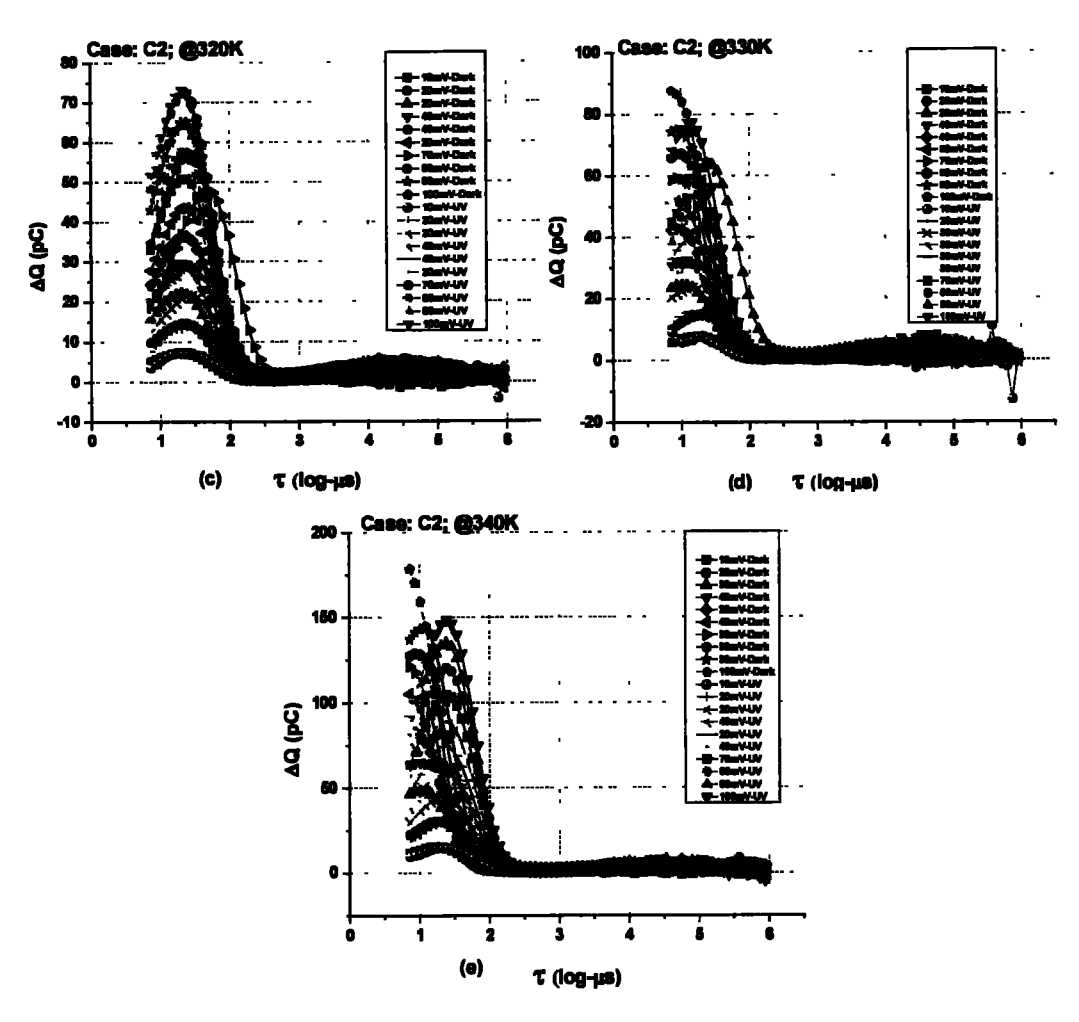
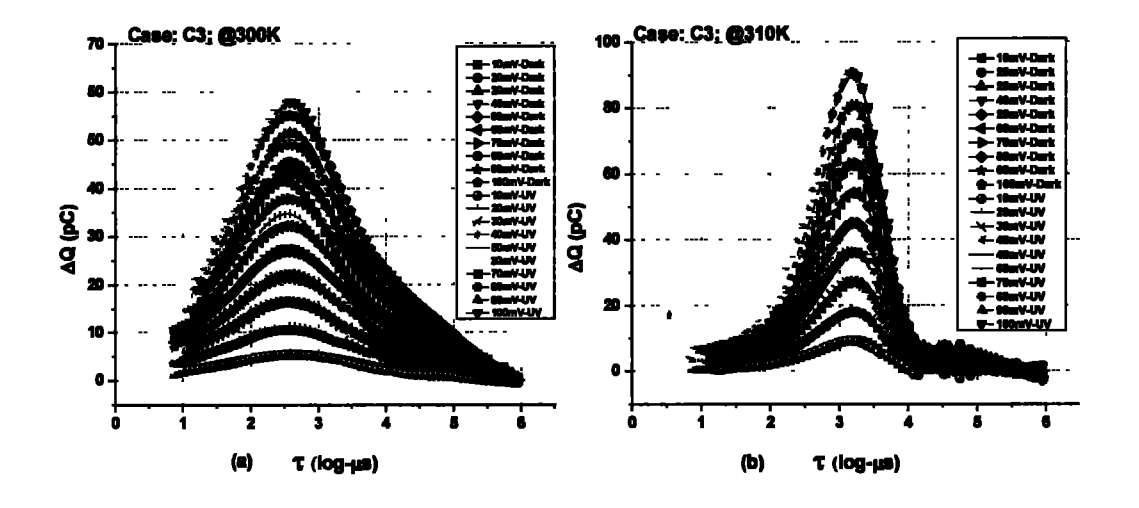


Figure 5.34: Q-DLTS analysis of Case C2 under multiple bias sequences ranging from 10-100mV (a) 300K temperature, (b) 310K temperature, (c) 320K temperature, (d) 330K temperature, (e) 340K temperature



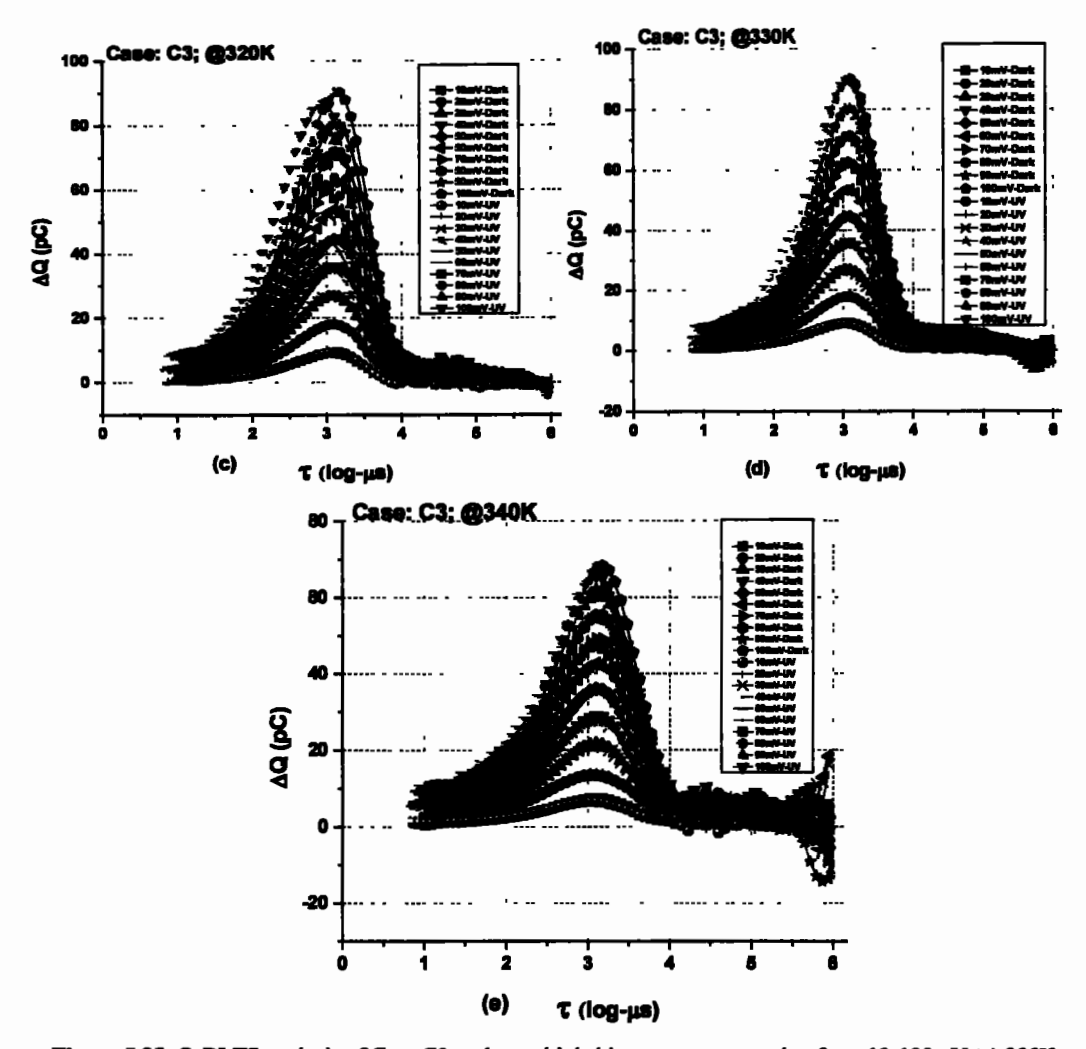


Figure 5.35: Q-DLTS analysis of Case C3 under multiple bias sequences ranging from 10-100mV (a) 300K temperature, (b) 310K temperature, (c) 320K temperature, (d) 330K temperature, (e) 340K temperature

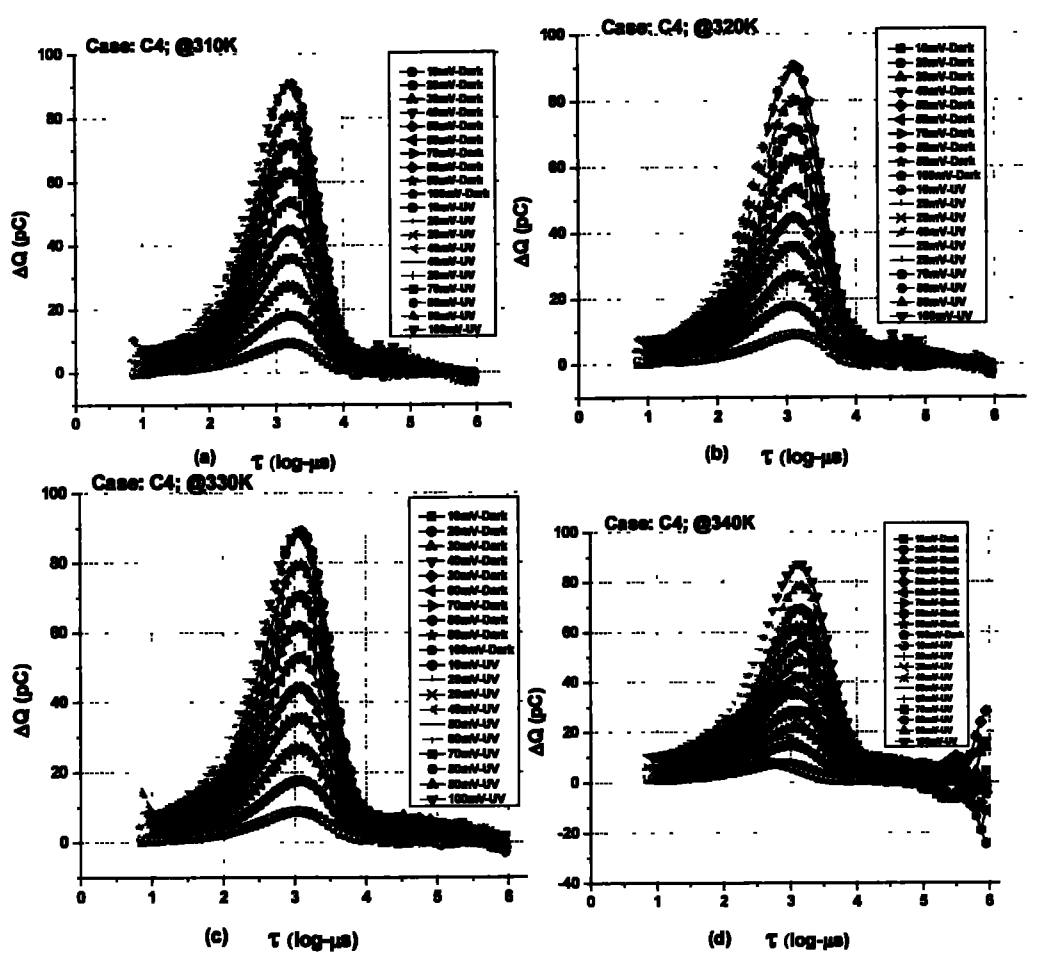


Figure 5.36: Q-DLTS analysis of Case C4 under multiple bias sequences ranging from 10-100mV, (a) 310K temperature, (b) 320K temperature, (c) 330K temperature, (d) 340K temperature

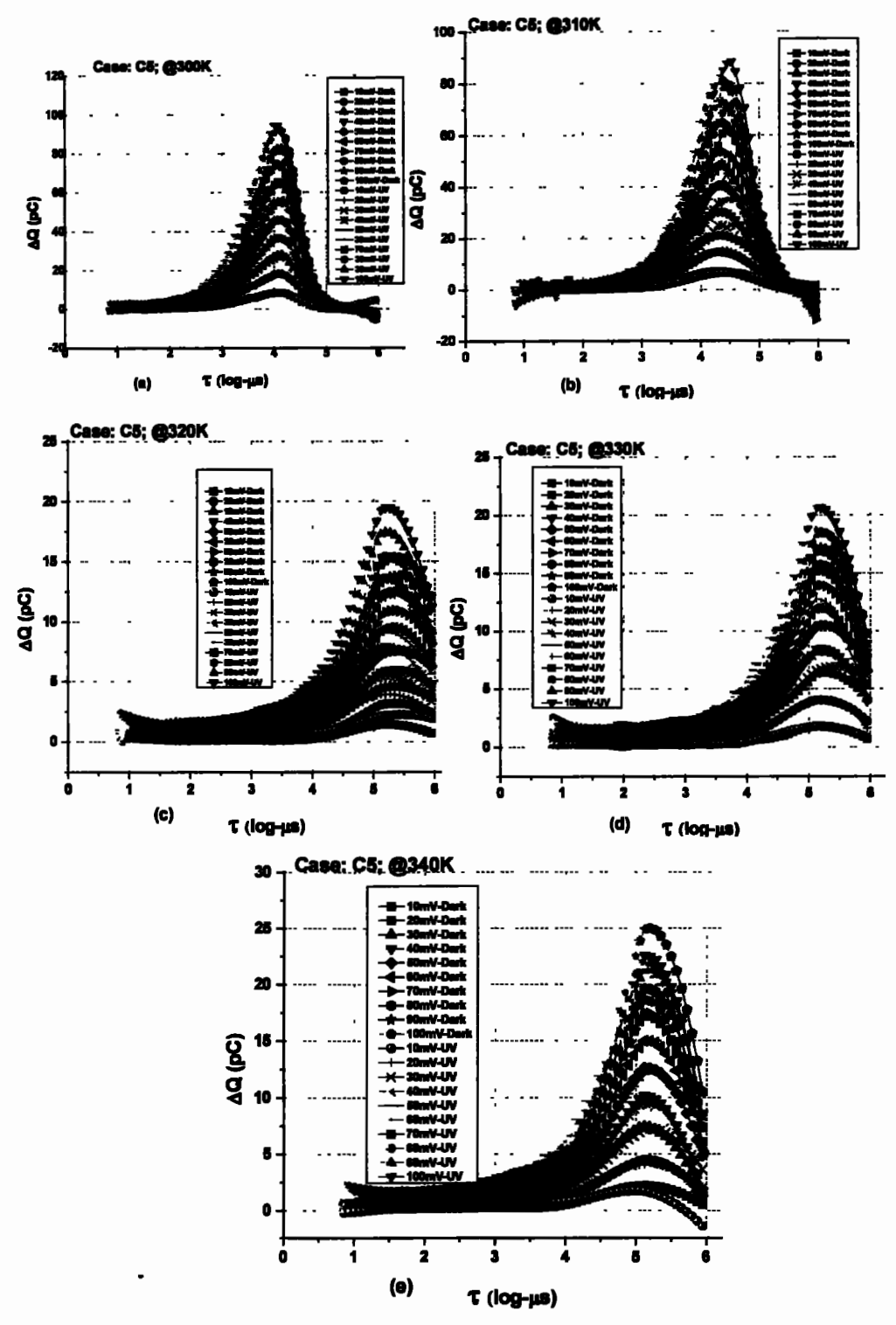


Figure 5.37: Q-DLTS analysis of Case C5 under multiple bias sequences ranging from 10-100mV, (a) 300K temperature, (b) 310K temperature, (c) 320K temperature, (d) 330K temperature, (e) 340K temperature

For quick analysis; the Arrhenius analysis of C2 case under dark mode at 40mV condition is the most reliable center with minimum tolerance in trap's location. The corresponding Q-DLTS spectra and aforementioned Arrhenius slopes are indicated in Figure 5.38.

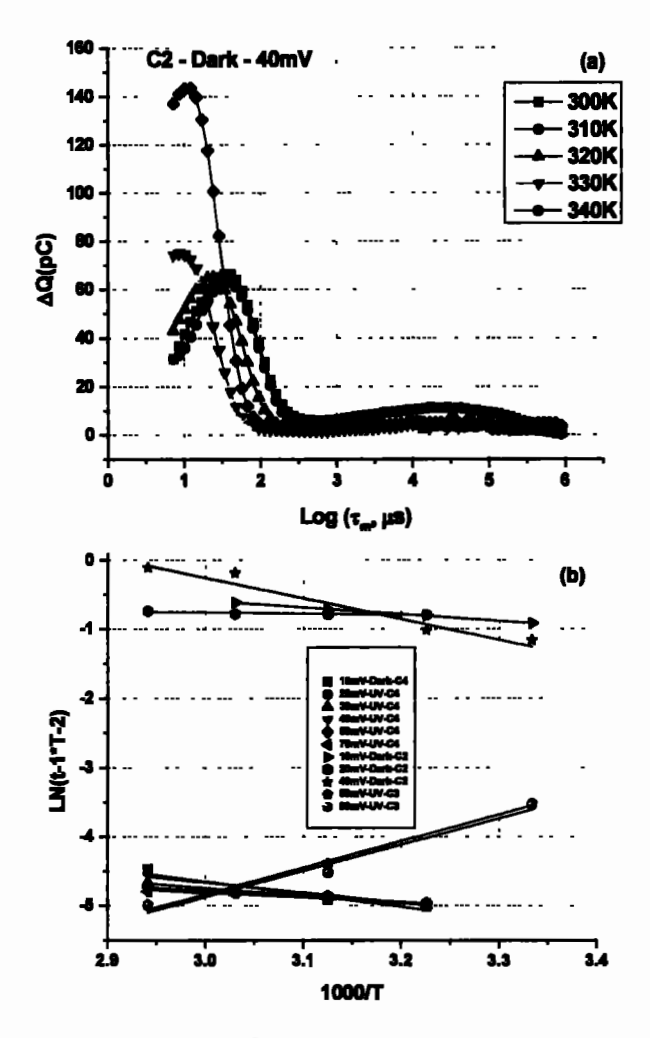


Figure 5.38: Q-DLTS analysis, (a) Q-DLTS of 40mV-Dark-C2. (b) Arrhenius analysis of all detectable cases

For all cases; one has experimented each cases at all particular drift potentials. However, only C2, C3 and C4 cases (for particular potentials) shows linear Arrhenius characteristics, thus, one have discarded other respective cases and mentioned only those whose responses are in good agreement with the linear region and their respective trap parameters are mentioned in Table 5.5 at length.

Table 5.5: Q-DLTS based Arrhenius analysis of successfully observed trap parameters

Case	Electric Potential	Luminous Mode	Trap Location (Et)	Capture Cross section (σ)
C4	10mV	Dark	Ev + 0.158 eV	4.98E-22
C4	20 mV	UV-Light	Ev + 0.126 eV	1.60E-22
C4	30 mV	UV-Light	Ev + 0,094 eV	4.93E-23
C4	40 mV	UV-Light	Ev + 0.063 eV	1.58E-23
C4	50 mV	UV-Light	Ev + 0.069 eV	1.98E-23
C4	70 mV	UV-Light	Ev + 0.059 eV	1.38E-23
C2	10 mV	Dark	Ev + 0.083 eV	2.19E-21
C2	20 mV	Dark	Ev + 0.016 eV	1.77E-22
C2	40 mV	Dark	Ev + 0.259 eV	1.35E-18
C3	80 mV	UV-Light	Ec - 0.333 eV	1.55E-29
C3	90 mV	UV-Light	Ec - 0.327 eV	1.83E-29

It is clear from Table 5.5 that most of the trap centres observed for the respective cases are the recombination in nature because the traps are localized themselves near the valance band edge as reported in [23-24]. For example, at 40 mV (C2-Dark) the trap's location is  $\sim Ev + 0.259$  eV which is recombination center i.e., whenever the UV light is impinged onto the device, respective trap level captures the free carriers with the effective capture cross section of  $\sim 1.35 \times 10^{18}$  at that particular location and reduces the numerical gain as highlighted in Figure 5. However, the numerical gain, in this case, is still in an acceptable limit. This indicates that these trap centers are favorable for UV response and may provide better detection capability to the device.

In this section 5.2, AIN layer of ~200 nm onto the Silicon <111> substrate (n-type), has been grown, using Hydride Vapor Phase Epitaxial growth system and developed the interdigitated electrodes by the atomistic scale Physical Vapour Deposition PVD technique. After successful development of interdigitated electrodes, the said device matrix has been subjected to a range of electrical, transport and charge-based techniques with a special reference of charge-based UV light detection. Among the variety of circuit configurations, the maximum UV detection has been experienced in the case where the silicon is connected to more positive potential and the respective interdigitated electrodes are at 0V condition i.e., no electric potential has been

externally applied at 300K temperature (with the numerical gain of >100x). At 330K temperature condition, only interdigitated case provides maximum UV detection at the numerical gain of ~60x at an operating potential of 60 mV. In this case the bottom surface of Silicon has not been connected with any of the reference potential i.e., no physical connection of either positive or negative terminal of the drift source is available. The Q-DLTS based Arrhenius analysis performed under each bias potential (Dark and UV), however, reveals that only fewer cases follow the standard Arrhenius equation and fewer cases readily point to the corresponding defect levels and associated capture cross sections. Among all these detected trap centers, the favourable configuration supporting the light detection is the one where silicon was connected with more positive potential and the respective interdigitated electrodes were placed at 40 mV. Q-DLTS measurements also reveal that most of the measured trap centers in AlN/Si heterogenous junction-based device are the recombination ones and may likely to act favorably under UV detection.

# 5.3 Ion Implantation of Silicon and Development of Metal-Semiconductor-Metal (MSM) on AlN/Si

The Ion implantation of already developed AIN structure needs some ion-implantation sequences so that the range as well as potential of the photon detection would be optimized. As the bandgap of AIN is ~6eV, thus, only the photons equal to or greater than that of this energy would be detected. The lesser energy photon would have capability to be detected either if sufficient trap centers are presented within the bandgap for further exploitation. Using ion implantation one would be able in determining the impact to perform the detection mechanism for variety of photon energies. The ion implantation sequence of silicon ions has been depicted in Table 5.6.

Table 5.6: Silicon Ion Implantation on AIN/Silicon structure

Sample Structure	Implant	Dose (cm <sup>-2</sup> )	Energy (keV)	
AlN/Silicon	Silicon	~10 <sup>14</sup>	800	

The atomic and disorder profile of silicon atoms within the AlN device structure have been simulated using SUSPRE and shown in Figure 5.39.

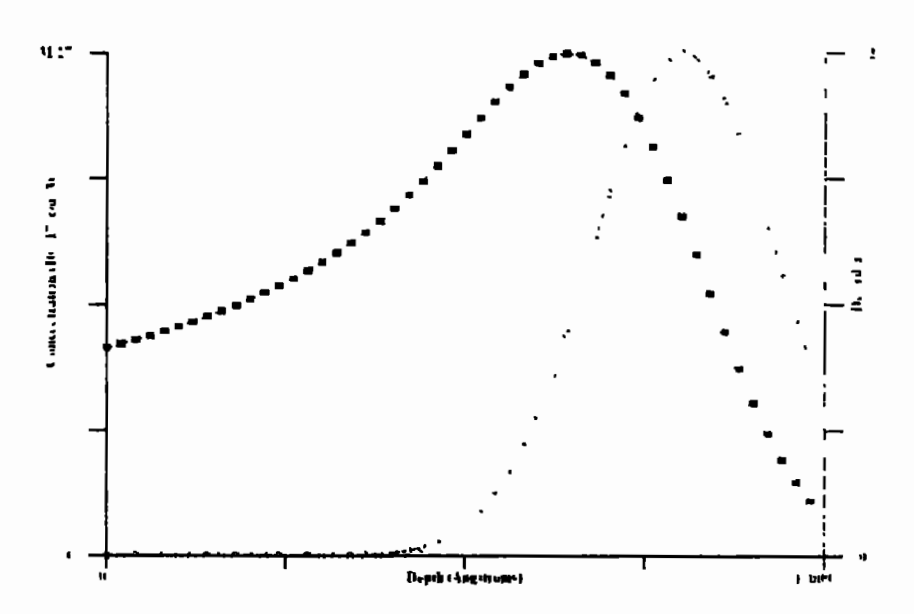


Figure 5.39: Atomic and disorder profile of silicon atoms within the AIN/Silicon structure

Figure 5.39 reveals that the top surface is surrounded by the silicon atoms in the carrier concentration in orders i.e. ~10<sup>17</sup>cm<sup>-3</sup>. The disorder profile at the top layers is about negligible, which means that the top surface has not been damaged to provide the sufficient defect levels in the silicon implanted region.

#### 5.3.1 Development of MSM structure on the silicon implanted region

In this section, we will develop a Metal-Semiconductor-Metal device structure onto the silicon implanted region by utilizing Physical Vapor Deposition (PVD) technique. The silicon ion implantations are performed at the discrete parameters mentioned in Table 5.6. The ion implantation of silicon was performed onto the hyperfine layers of AlN fabricated onto the pre-

fabricated n-type Silicon substrate. Initially the AlN wafer was cleaned by the standard cleaning protocols i.e., the splash of Acetone and Iso-Propyl Alcohol (IPA) followed by the deionized water. After the standard chemical cleanings, the AlN wafer was treated with the Nitrogen gas (99.99%) splash and placed into the deposition chamber using the resistive heating PVD. PVD was equipped with a close loop nitrogen gas splash system in order to prevent the freely available particulates into the bare atmosphere. In this experiment the Aluminum (Al) metal was chosen as a metal contact for MSM structure, however the prephotolithography steps were taken into account for the deposition at desired location as mentioned in Figure 5.37. The thickness of ~100nm was fixed during deposition step and the thickness value was continuously monitored using gold plated quartz crystal oscillator. For melting Aluminum (Al) metal, one has used tungsten boat and used ~90A for melting aluminum target. The step wise development of aluminum based MSM structure has been mentioned in Figure 5.40.

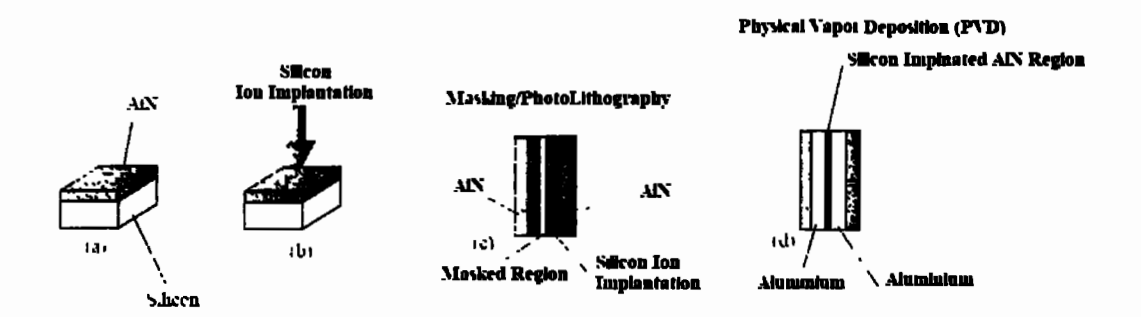


Figure 5.40: Development of MSM structure on implanted AIN region, (a) AIN/Silicon structure, (b) Silicon ion implantation using peletron accelerator, (c) Masking procedure using Photo-Lithography and (d) development of MSM structure using Physical Vapor Deposition (PVD)

### 5.3.2 Characterization of Silicon implanted AlN/Silicon structure

After carefully fabricated MSM structure, one needs to characterize subject device structure on variety of techniques for the evaluation of photon detection. Current-voltage (I-V), Charge-Deep Level Transient Spectroscopy (Q-DLTS), kinetics of dark and luminous currents (I-t) and Transient of Photo-Voltage (TPV) are performed for the test and evaluation of device output performance.

#### 5.3.2.1 Current-Voltage Characterization of Silicon Implanted AlN/Silicon Structure

This is the initial characterization step used to evaluate current-magnitude under incremental bias conditions. In this case one has varied the potential from zero to five volts and measured the current magnitude. At room temperature 300K the electric current was about  $6.7\mu$ A and as soon as the temperature increases the current magnitude also varied because the carrier gained higher energy and became active for conduction. Arrhenius characteristics (1000/T vs Ln( $\sigma$ )) shows that 82.44meV energy is needed to physically conduct at this part specific implanted region. The current-voltage and its respective Arrhinius analysis is shown in Figure 5.41.

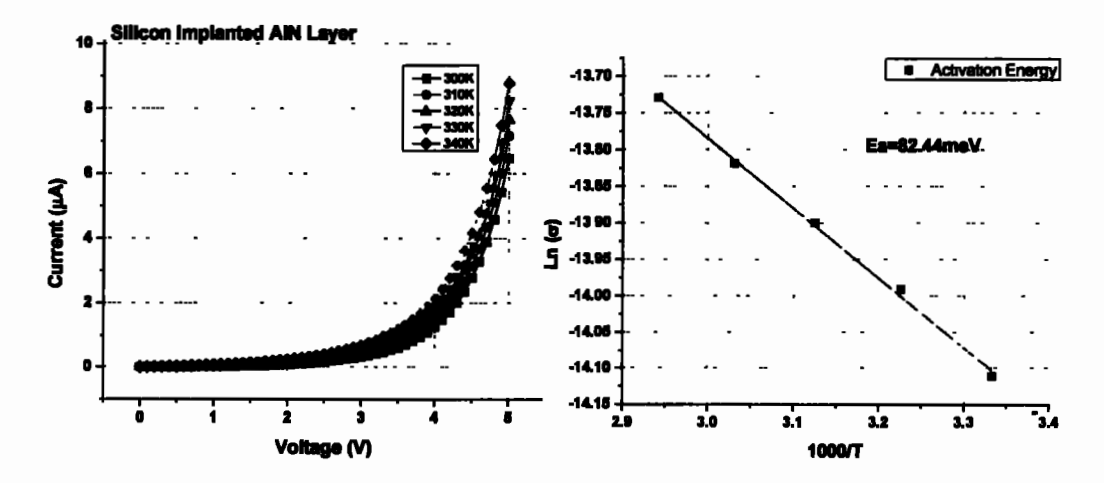


Figure 5.41: Current-Voltage and Arrhenius analysis of Silicon implanted AIN/Silicon structure

# 5.3.2.2 Charge Deep Level Transient Spectroscopy (Q-DLTS) of Silicon Implanted AlN/Silicon Structure

The inert behavior at AIN/Si interface has keenly been envisaged under a very powerful charge based technique named Charge-Deep Level Transient Spectroscopy (Q-DLTS). This becomes particularly important when the ion implantation has been performed on to the subject device. In order to map the defects at the interface/implanted region, O-DLTS technique is utilized, which is a charge relaxation technique based on the measurements of charge transients to analyze the quantity and quality of the traps. The quantity of the traps may be of two attributes i.e. the number of trap centers (either the recombination or the generation one) and the density of traps. The quality of the traps can be attributed towards the ability of physical attraction of the free carriers towards the said energy level energy. In Q-DLTS, initially the voltage is sustained at V<sub>0</sub> for a particular interval in order to just synchronize the power supply with the device under test. After this time span (charging time) the voltage bias is been drifted at some specific magnitude and this particular time span is more enough in order to perfectly charge the internal deep levels. For all said cases the charging time and the discrete voltages are ~ 100ms and 1, 2, 3 and 4V, respectively which is aligned with the device operational requirements generally used in the light detection and other photonic applications. After passing through the charging window, the bias was suddenly removed and discharge events were monitored from the powerful integrator circuitry which recorded each discharge interval. The time based Voltage-Charge (V-Q) diagram is shown in Figure 5.42 below.

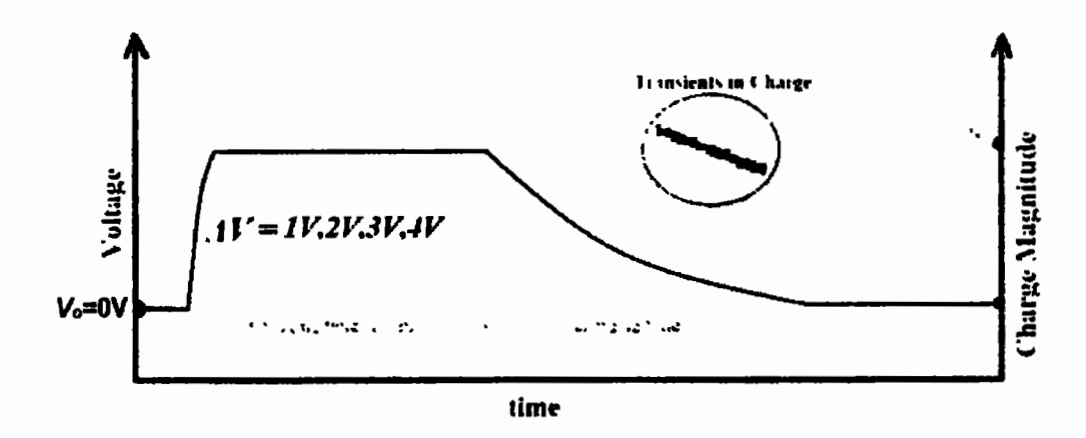


Figure 5.42: Current-Voltage and Arrhenius analysis of Silicon implanted AIN/Silicon structure

The brief introduction of the technique is given in section **5.1.2.3.** The Q-DLTS measurements are carried out at variety of applied voltage sequences as mentioned in Figure 5.39. From this analysis one could determine the quantity of traps formed. The change in the surface trap concentration may evaluated from the highest magnitude of change in charge magnitude and can be derived from Equation 5.8.

$$\Rightarrow N_T = \frac{44Q_{max}}{qA}$$
 Eq. 5.8 [17, 19]

Where, ' $\Delta Q_{max}$ ' is the maximum change in charge, 'q' is the universal charge constant (1.6x10<sup>-19</sup> C) and ' $\Delta$ ' is the surface area upon which charge carriers have to be accumulated. This could be analysed that as the application of drift bias potential increases the change in charge magnitude would also be increased which consequently increases the traps/defects magnitude as per relation 5.8. The Q-DLTS analysis of silicon implanted AlN structure is shown in Figure 5.43.

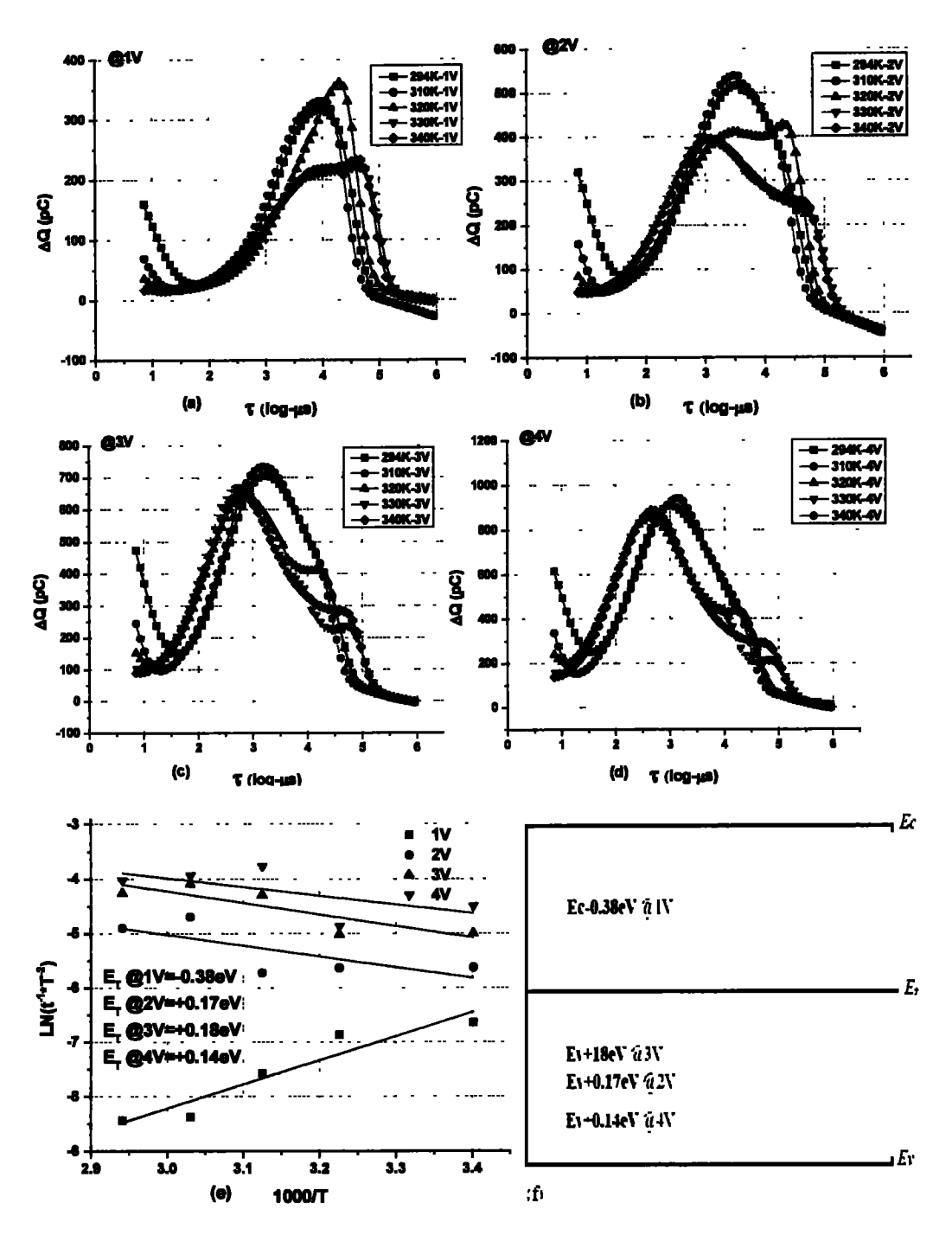


Figure 5.43: Charge Deep Level Transient Spectroscopy (Q-DLTS) at different temperature of Silicon implanted AlN/Silicon structure, (a) Q-DLTS spectra at 1V, (b) Q-DLTS spectra at 2V, (c) Q-DLTS spectra at 3V, (d) Q-DLTS spectra at 4V, (e) Q-DLTS based Arrhenius analysis, (f) Energy band picture at different drift potentials

The energy band picture is an essential notation that may provide the internal insight about the carrier dynamics as provided in Figure 5.43 (f). In this figure one has deliberately not depicted

the bandgap of the semiconductor because the subject region is heavily bombarded by the silicon atoms and it is not exactly known as to what is the real extent of band gap at a given region. This is because the Aluminium, Nitrogen and Silicon have been incorporated into a single lattice structure. This has been noticed that the highest generation center of Ec-0.38eV as evaluated been monitored by this charge based technique, which may play a vital role during photon sensing mechanism.

## 5.3.2.3 Transient of Photovoltage (TPV) of Silicon Implanted AlN/Silicon Structure

To properly envisage the impact for photonic activity of the AIN/Si stack; Transient of Photo-Voltages (TPV) analysis is performed. In this analysis, a very sharp pulse of visible light is incident on the device for a very short time interval [14] and the decay of charge carriers are observed as function of time. During this time the transient in voltage scale occurs and rises to some steady state value and then decay of the carriers are also observed. In TPV approach, the photo voltage transient at the end of light pulse consists of rapid drop followed by the slower decay. The initial drop is due to electron hole pair recombination and the slower decay is due to carrier emission [14]. Thus, both of the centers i.e. recombination and generation are activated and contribute to their respective impact in the device operation. Figure 5.44 shows the TPV analysis of silicon implanted AlN/Silicon structure.

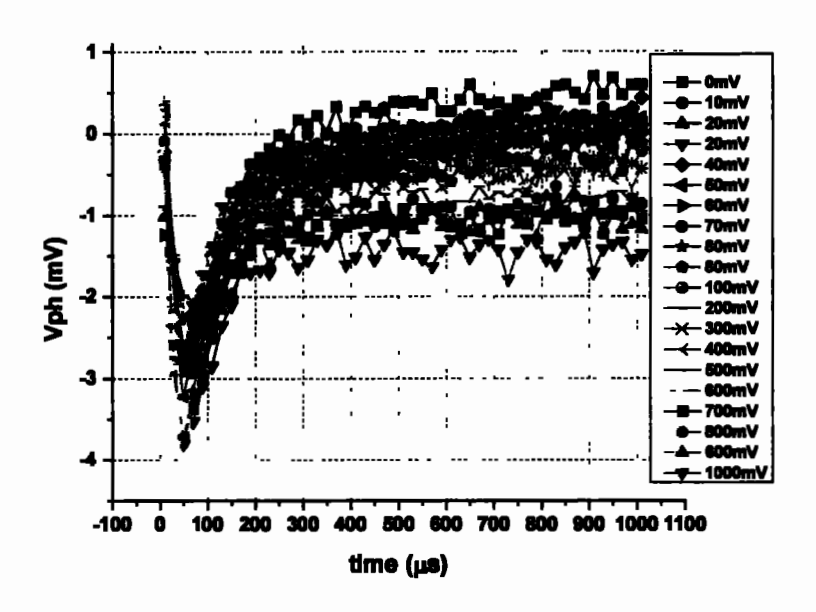


Figure 5.44: Transient of Photo-voltage (TPV) of Silicon Implanted AIN/Silicon Structure

Figure 5.44 shows the TPV spectra at different drift voltages ranging from 0-1000mV. As mentioned earlier the visible light is incident on the subject region. This provided substantial amount of charge carriers providing the detection in form of voltage transients. This is another benchmark achieved i.e. silicon implantation within the AIN could provide photon sensing in several forms of UV as well as low energy photons in visible regions. This phenomena may also be investigated in a larger paradigm in kinetics of dark and photo currents at visible as well as UV family of light sequences. The subject detection is only possible when the silicon atoms may produce their defects level within the near premises of valance band of AIN structure as already been mentioned in Figure 5.43 (f). This would indicate that subject region is also ready for the detection of low energy photons even when the bandgap is very high of the order of ~6eV. Another advantages of TPV spectra is that the transient of voltages has also been available even at rather higher drift biases, however the diminish time of voltages transients are larger for larger extent of voltages which could limit the overall bandwidth of the device.

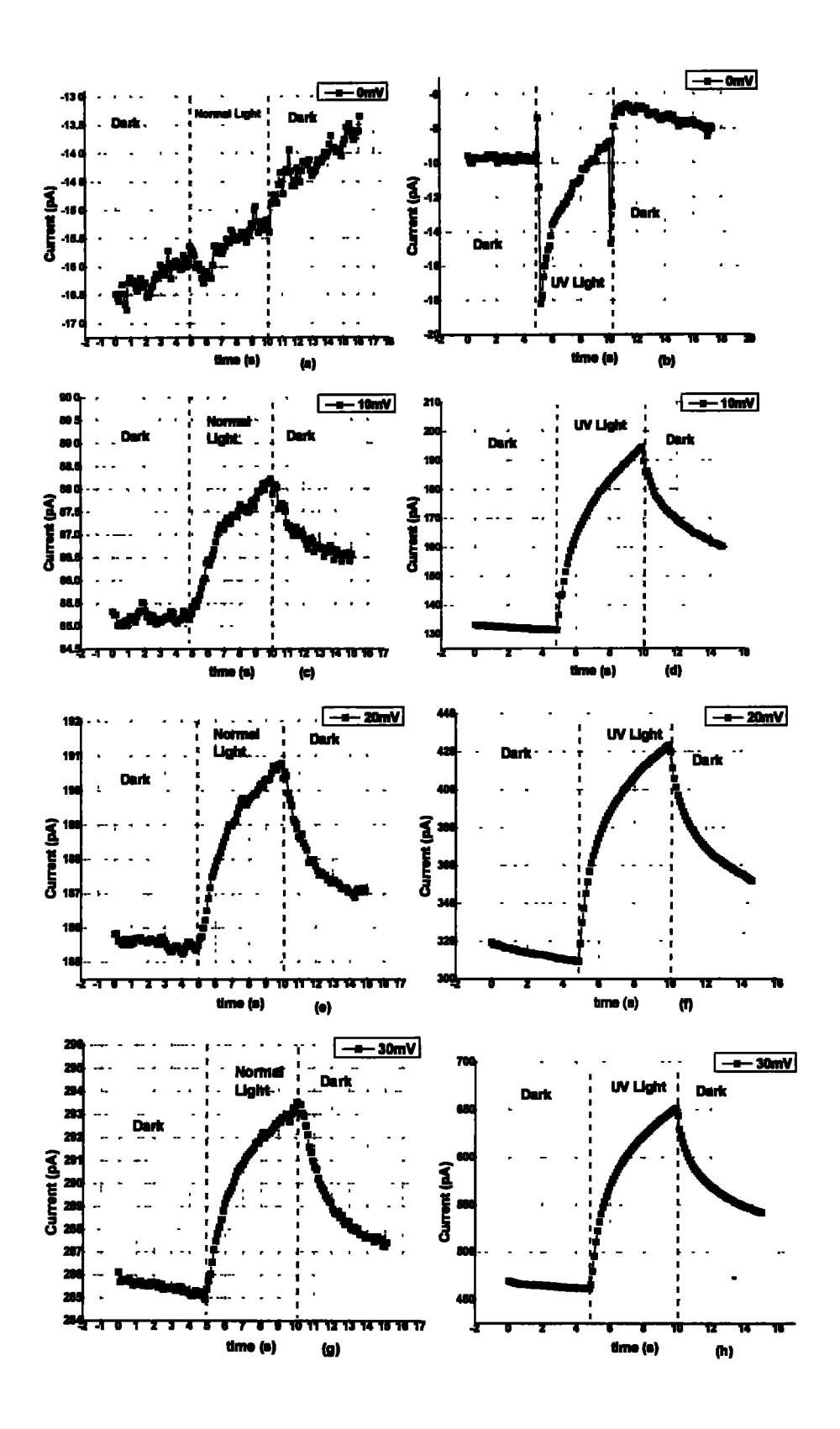
# 5.3.2.4 Kinetics of Dark and Light (Visible and UV) current of Silicon Implanted AlN/Silicon Structure

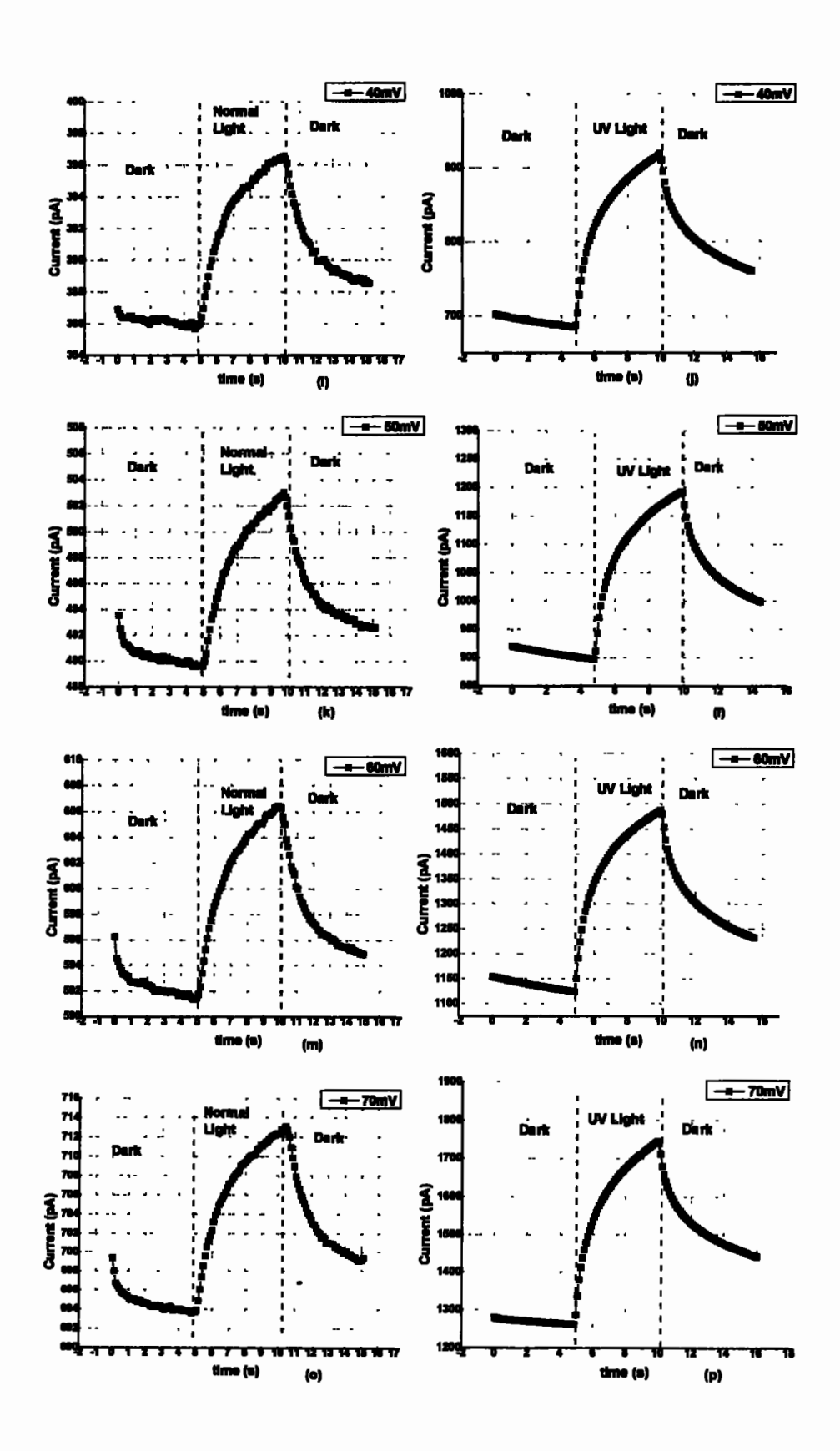
The final approach to map the carriers for their utilization in photonic activity in the fabricated device structure is the investigation of kinetics of current under two modes of operation i.e. only light is used as pumping source to the carriers and the other is the external drift voltages, respectively. This is an important feature for the photonic application particularly for the devices utilizing the UV to DUV phenomena. TPV and Q-DLTS studies have provided an insight that the visible light could also be detected from said implanted region. Kinetics of dark and light currents are shown in Figure 5.45.

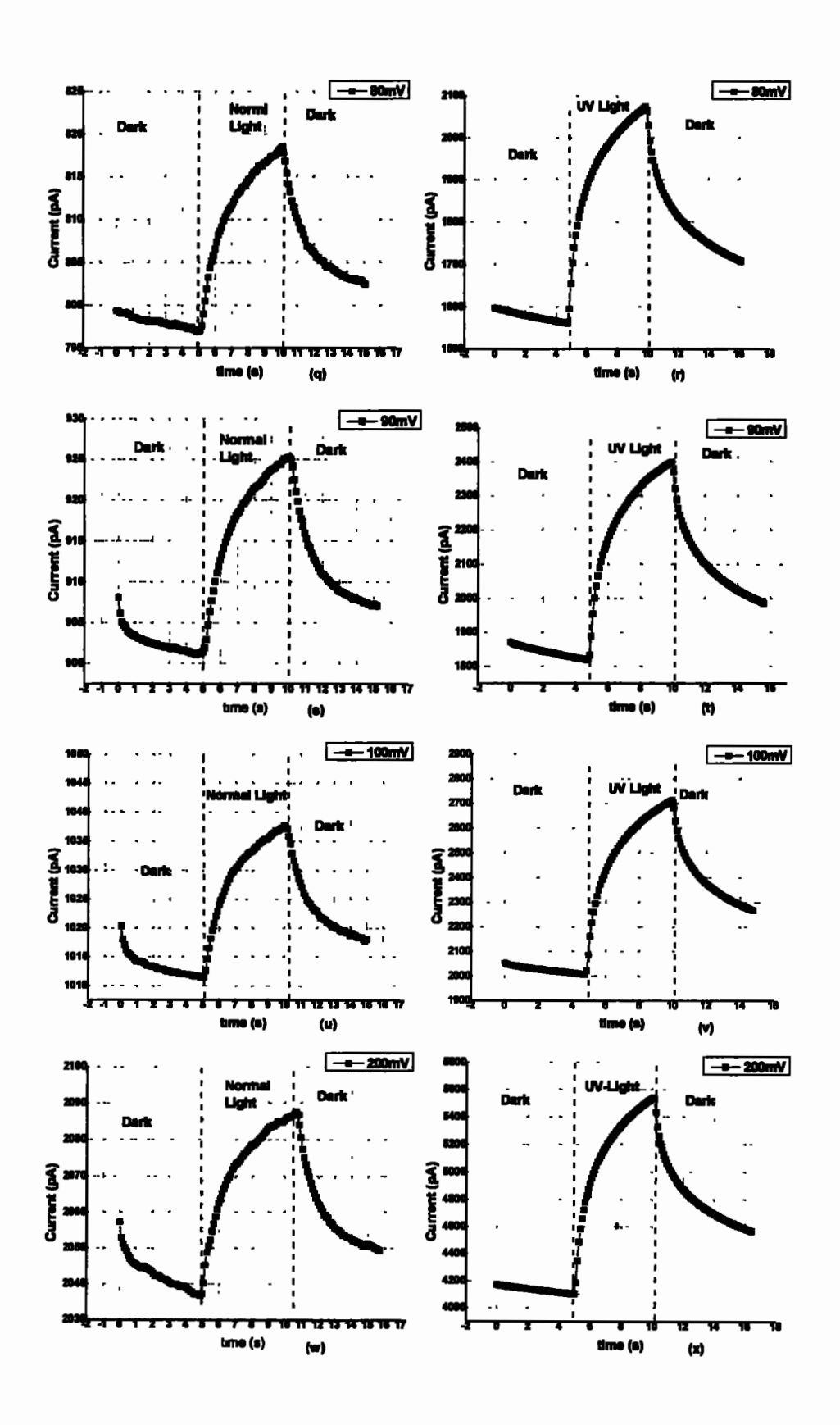
Figure 5.45 shows two operational windows i.e. Dark and Light (visible and UV family): In the Dark mode, the AIN stack is covered by an opaque object whereas in Light mode two types of light sourcs are utilized i.e. Normal visible light ranging from 380-780nm under Ultra Violet (UV) filtered Halogen's Lamp is shone onto the device stack for ~5 seconds. However the energy of the transmitted light has been filtered by an optical filter of UV light. Thus, the output light is completely free from UV family of wavelengths. The highest energy that can transmit through optical source is 380nm which points out to the maximum band gap of ~3.26eV where the Silicon band gap is just ~1.12eV. Thus, these energy profiles could easily be detected by the Silicon implanted region. The UV optical filter is deliberately used in order to see the impact of low energy photon quanta that may only interact with the respective deep levels. On another hand the Ultra Violet (UV) light has also been exposed for the detection purpose over the same dark-light sequences. For UV family of light detection, this is observed that when there is a transition between Dark to the luminous mode and the vice versa, the abrupt peak in an electronic current is recorded. This is the signature that when light of sufficient energy (Within the UV to DUV regime) strikes to the AlN lattice, the electron-hole pair gets generated but this pair diminishes because of the powerful recombination centers that recombine the free

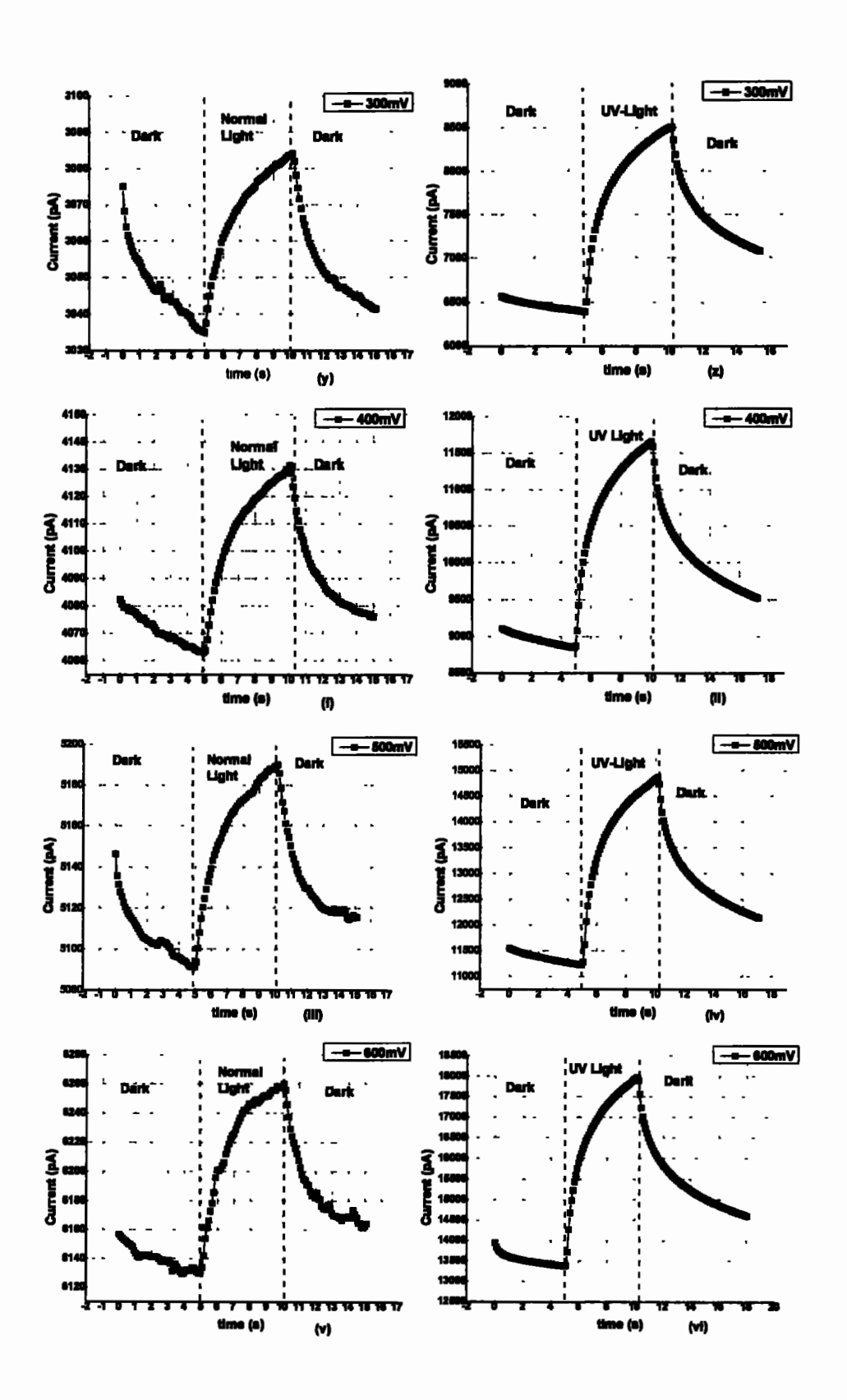
carriers. This is why only abrupt peak is observed rather than the continuous emission of carriers from the probed region. However when the low energy visible light is incident onto the subject implanted region, there is no enhancement/depletion of the carriers which would be observed at this specific zero potential. This may be owing to the fact that the energy of the light is too low to transit the carriers to its conduction levels.

While in a Photoconductive mode of operation (when external drift potential has been applied and the light of visible or UV would be incident onto the sample), the subject AlN stack is influenced by an external electric field and subjected to Dark and Light modes as mentioned earlier. Likewise the photovoltaic mode (at only zero potential), Figure 5.45 shows the photoconductive mode of silicon implanted structure of AlN (probed by MSM topology). For all of these cases, 10-1000mV are applied and visible as well as UV lights are subjected onto the silicon implanted AlN structure and sensed the electric current behavior for optimum detection of incoming photons. As soon as the external bias is applied, the subject stack is accumulated by the carriers at a certain level which is due to the capacitive nature of the stack by which the charge is sensed. When the Light shines the carrier multiplies themselves whenever the light is present presented over the period and when the source turns to the OFF state, the carrier diminishes themselves in a detrimental fashion. A detailed observation of visible and UV light behavior onto the said implant region has been shown in Figure 5.45. Under 0mv and 10-100mv applied drift potential (each case is represented separately)









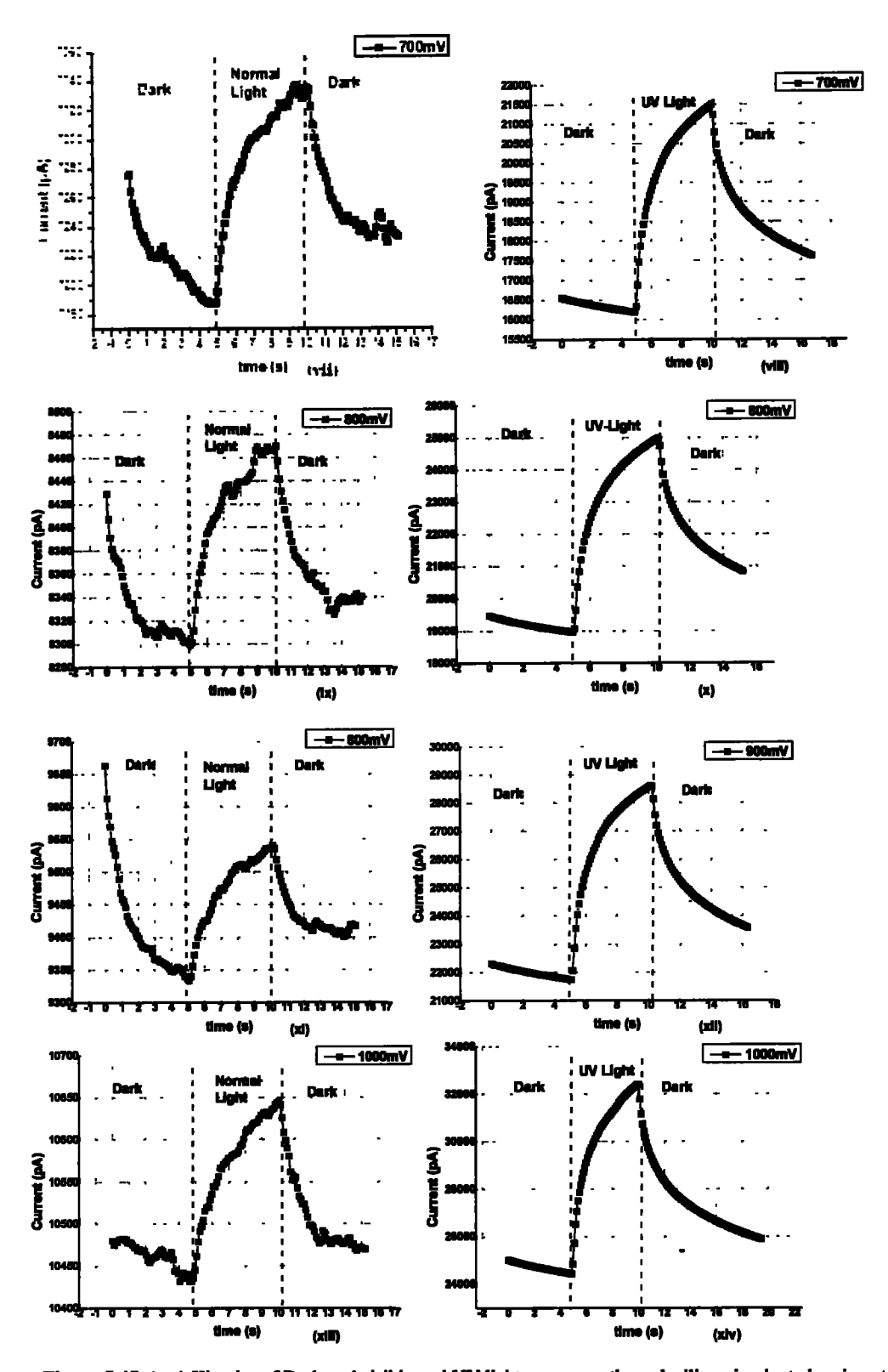


Figure 5.45: (a-z) Kinetics of Dark and visible and UV light sequences through silicon implanted region at AIN/Silicon structure under 0mV and 10-300mV applied drift potential (i-xiv) from 400-1000mV

From Figure 5.45 it is observed that the silicon implanted region would be able to detect both low energy photon quanta as well as the high energy photon quanta of UV/DUV regime. However, this has been noticed that the dark current at same potentials for both visible and UV cases are different which could limit the performance of the photo-detector. This may be because of the capacitive nature of the sensor i.e. as per transient analysis of the capacitor the electric current continuously decreases because of charging phenomena. Another variable that could be measured for the calibration of such type of photo sensors is the 'Gain' calculation. It is the measure of extent with which the light impinges into the electric current magnitude and could be related by the following relation 5.10.

$$Gain = \frac{Light Current}{Dark Current}$$
 (5.10)

The Dark, visible light and UV/DUV currents for Gain are measured and presented in Table 5.6.

Table 5.7: Dark, visible light and UV currents for Gain measurements

Voltage (mV)	Dark Current (pA)	Visible Light Current (pA)	Gain _Visible	Dark Current (pA)	UV Light Current (pA)	Gain _UV
0				7.368	18.17	2.466069
10	85.27	88.22	1.034596	131.313	194.52	1.481346
20	185.49	190.79	1.028573	309.25	423.35	1.368957
30	284.9	293.5	1.030186	465.6	651.57	1.39942
40	385.97	396.5	1.027282	684.69	919.4	1.342797
50	489.62	502.64	1.026592	897.5	1190.9	1.326908
60	591.43	606.4	1.025312	1123.38	1484.9	1.321815
70	693.7	712.79	1.027519	1261.53	1744	1.382448
80	797	818.47	1.026939	1561	2073.5	1.328315
90	901.46	925	1.026113	1818.8	2400	1.319551
100	1011.5	1037.6	1.025803	2006.4	2712.8	1.352073
200	2037.26	2087.12	1.024474	4102.4	5540	1.350429
300	3035	3084	1.016145	6391	8504	1.330621
400	4063.2	4131.2	1.016736	8846	11655.7	1.317624
500	5091.22	5190	1.019402	11221.57	14866.76	1.324838
600	6129.4	6260.1	1.021323	13382.39	17973	1.343034
700				16189	21456.32	1.325364
800	8300	8469.8	1.020458	18957.59	24988	1.3181
900	9333.3	9540.4	1.022189	21735.9	28592.79	1.315464

1000	10431.46	10645.42	1.020511	24426.26	32384.94	1.325825
------	----------	----------	----------	----------	----------	----------

For better clarification and visualization one has plotted statistical approach of gain magnitudes and are depicted in Figure 5.46. This could be noticed that both the visible and the UV lights have greater than one 'Gain'. This declared that both lights shows detection and contribute photonic currents at this specific implant scheme. However, the extent of 'Gain' performance for UV/DUV light is much greater than that of visible light.

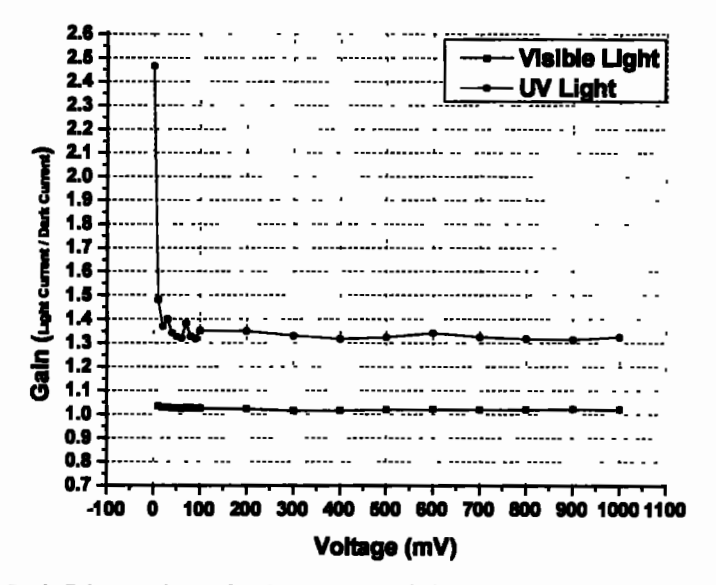


Figure 5.46: Gain magnitudes for Visible and UV light on silicon implanted AlN structure

## 5.4 Comparison with Reported Literature

D.J. Xi et al. have fabricated the AlN on p-Si grown by low pressure MO-CVD technique and studied the interface of AlN/p-Si using same Capacitance-Voltage (C-V) technique. During their analysis the thickness of AlN was just 15nm and the contact diameter was ~0.25mm, under the frequency and voltage range of 50Hz-1MHz and -3V/+3V, respectively. The maximum capacitance magnitude was ~403 pF @50Hz frequency [127]. In our scenario we an

intermediate frequency of ~25kHz, has been chosen and the contact area was ~1mm<sup>2</sup> and the capacitance was monitored to see the columbic interaction of charge carriers at AlN/n-Si interface and the maximum capacitance has been observed for +ve polarity i.e. ~72pF. The less value of capacitance has been observed due to thicker AIN layer compared to just 15nm AIN as reported by D.J. Xi [127], i.e. thicker insulator boundaries provide lesser capacitance magnitude. As per ideal capacitance-voltage technique of Metal Insulator Semiconductor (MIS) structure, there are three fundamental regions which would be related to the charge state i.e. Accumulation, Depletion and Inversion. However, these states are merely possible for the proper impulsion of charges when they are separated by some physical distance. In our particular cases, the silver contact acted as a metal layer, AlN acted as an insulator layer and the silicon is a semiconductor, thus, the structure is confined in the MIS geometry. One could only examine the depletion state because for proper examination of all said charge states, the insulator (AlN) layer should be totally surrounded by the metal (Ag.). Topology in our case of miniaturized contact area is limited because we require photonic detectivity from the AlN layer. thus, one needs larger bare AlN layer instead of total coverage by metal layer (because in that scenario, no light would interact with AlN region and photonic detectivity would not be possible).

Jason B. Rothenberger et al. have worked on the surface termination of AlN under Helium Atmosphere and performed the Q-DLTS to evaluate the trap levels and capture cross sections. They have observed that Helium atmosphere localized the trap centers at 0.31 eV, 0.61 eV, 0.52 eV, 0.19 eV, and 0.40 eV and capture cross sections  $4.9 \times 10^{-21}$ ,  $1.3 \times 10^{-16}$ ,  $2.9 \times 10^{-19}$ ,  $3.1 \times 10^{-19}$ , and  $4.7 \times 10^{-19}$  cm<sup>2</sup>, respectively [132]. Y. Taniyasu et al. have fabricated the AlN based p-n junction Deep UV LEDs (210nm). The n- and p-type region was developed by silicon and magnesium doping, respectively. The ionization energy was estimated ~630meV, which was acceptor in nature [133]. In another study B. Neuschl et al. have reported the donor

ionization energy of silicon into the AIN lattice of the magnitude of  $63.5 \pm 1.5$  meV [134]. The ionization energies are reported in the suggested literature [135] which were inspected by the temperature variant Photo-Luminisense (PL) spectroscopy. Whereas charge based technique, has been applied to evaluate the deep level donor and acceptor traps on different geometrical planes and the bias polarities (positions within the bandgap). Further, Q-DLTS in our case has utilized the temperature window ranging from 300K-350K for practical device operation; whereas they used temperature dependent PL in the ranges from 4K to 278K.

Thus, the nature of our experiment and the device schemes are relevant and appropriate with verifiable detectivity/securing performance of the stack/upgradeable substrate for UV/DUV applications. The electro-optical behaviour of the device fabricated in our work is promising for a variety of advanced device structures to be utilized in manufacturable detectors/photo sensors.

## Chapter 6

## **Conclusion and Future Work**

A summary of the work performed and outcomes, and an outlook to the details in the following sections. The main hierarchy of the work is detailed in three distinct cases:

- a. Fabrication and Characterization of AlN over Silicon Wafer
- b. Development of Metal-Semiconductor-Metal (MSM) structure on AlN/Si for UV sensing
- c. Ion-Implantation of Silicon on AlN region and Development of Metal-Semiconductor-Metal (MSM) structure on implanted AlN/Si for multi-wavelength detection

### 6.1 Conclusion

In this study we will discuss the details about the fabrication and characterization of the viability of atomistic scaled AlN thin films deposited over Silicon substrate. This study may provide an insight for the detection of narrow length photons for sensing applications. AlN/Si matrix for photon sensing with multi-wavelength photon-detection specifically in UV regime are studied and analysed in three specific cases as mentioned above.

 A Hyperfine layer onto the pre-fabricated n-type Silicon substrate, has been successfully developed. Initially the silicon wafer with <111> orientation was cleaned by the standard cleaning protocols i.e., the splash of Acetone and Iso-Propyl Alcohol (IPA) followed by the deionized water. After the standard chemical cleaning, the silicon wafer was treated with the Nitrogen gas (99.99%) splash and placed into the deposition chamber using the epitaxial technique of Hydride Vapor Phase Epitaxy (HVPE). HVPE was equipped with a horizontal open-flow hot wall reactor and resistively heated furnace as a two-zone heating system. Substrate temperature was limited to a narrow range from 800°C to 1200°C with Argon as carrier gas. The AIN was deposited at the thickness set point of about 200 nm using a reaction between aluminum chloride (formed by the reaction between Aluminum metal and HCl gas) and ammonia. The film thickness and the deposition rate were monitored (about ~0.6nm/seconds) by the Quartz crystal thickness monitor.

- After the deposition, the portion of the device is cleaved and is first imaged through SEM to see the cross-section of the sample. SEM images clearly shows the formation multi-layers of AIN over Silicon substrate.
- When the AlN was deposited on silicon wafer, diffusion of Silicon occurs into the thin AlN layer formed and a new type of interfacial layer called the Si<sub>3</sub>N<sub>4</sub> was likely to be formed with some thermo-dynamical instabilities due to the presence of defects at the AlN/Si interface. These dangling bonds act as a point defects capturing most of free carriers either photonically induced or produced through drift pump mechanism by applying input bias.
- After the stack fabrication, morphological and electrical techniques such as Current-Voltage (I-V), Capacitance-Voltage (CV), Charge Deep Level Transient Spectroscopy (Q-DLTS), Transient of Photo-voltages (TPV) and Kinetics of Dark and Luminous Currents and Spectroscopic Ellipsometry (SE) are employed. These experimental techniques are used to study the physical dynamics of the AlN/Si junction and the role

- of charges/defects with within the structure for their potential utilization and exfoliation in photonic devices & systems and their subsequent performance.
- From Hall Effect Analysis of base Silicon (substrate); sheet resistance, carrier concentration and mobility has been found to be around 11.1  $\Omega/\Box$ , -1.39x10<sup>17</sup> cm<sup>-3</sup> and 1.14 x10<sup>2</sup> cm<sup>2</sup>/Vs, respectively.
- For multiple active region, the viability of AlN/Silicon has been tested and emulated for photon sensing. Four possible physical schemes have been developed through which the charge is pumped into the AlN stack subsequently mapped. The optical measurements have also been performed and evidence of Si<sub>3</sub>N<sub>4</sub> layer formation at the AlN and Silicon interface, which plays pivotal role to the overall AlN/Si stack.
- Inspection of four trap level within the energy band picture is also presented. Effect of these traps have also been mapped on the comparatively low energy photon quanta in order to map the leakage and their physical dynamics caused by the incoming photons. The transient of photo voltage analysis shows that the AIN with negative potential is able to detect more charge carriers when compared with other charge assisted physically drift schemes.
- It is also concluded that photovoltaic based current kinetics are more responsive than photoconductive part. Whereas in photoconductive mode, the charges are first accumulated for a specific duration due to the capacitive nature of all said physical schemes and their low energy photonic response is limited compared to the photovoltaic operation.
- For UV sensing, Metal-Semiconductor-Metal (MSM) structure has been fabricated using Physical Vapor Deposition (PVD) technique on previously grown AlN layer of ~200 nm onto the Silicon <111> substrate. Interdigitated electrodes were developed as test device structures. After successful development of interdigitated electrodes, the

- said device matrix has been subjected to a range of electrical, transport and chargebased techniques with a special reference of charge-based UV light detection.
- Five different circuit level approaches for better UV detection. Among these variety of circuit configurations, the maximum UV detection is experienced in the case where the silicon is connected to more positive potential and the respective interdigitated electrodes are at 0V condition i.e., no electric potential has been externally applied at 300K temperature (with the numerical gain of >100x). However, each case has been further verified at five different temperatures ranging from 300-340K.
- At 330K temperature condition, only interdigitated case provides maximum UV detection at the numerical gain of ~60x at an operating potential of 60 mV. In this case the bottom surface of Silicon has not been connected with any of the reference potential i.e., no physical connection of either positive or negative terminal of the drift source is available.
- The Q-DLTS based Arrhenius analysis performed under each bias potential (Dark and UV), however, reveals that only fewer cases follow the standard Arrhenius equation and fewer cases readily point to the corresponding defect levels and associated capture cross sections. Among all these detected trap centers, the favourable configuration supporting the light detection is the one where silicon was connected with more positive potential and the respective interdigitated electrodes were placed at 40 mV. Q-DLTS measurements also reveal that most of the measured trap centers in AlN/Si heterogenous junction-based device are the recombination ones and may likely to act favorably under UV detection.
- For multi-energy photon detection an ion implant energy of 800keV has been chosen for Silicon implant, with dosage of ~10<sup>+14</sup> cm<sup>-2</sup> over AIN. This scheme has been tested again by variety of techniques i.e. Current-Voltage, Q-DLTS, TPV and kinetics of dark,

visible and UV light sequences. From kinetics analysis, it is observed that said implanted structure provides fabulous results against both the visible light detection as well as the UV light. For better clarification and visualization statistical approach of gain magnitudes has been utilized. For both the visible and the UV lights, gain value of >1 is achieved. This signifies that both lights (visible and UV) show detection and contribute photonic currents at this specific implant scenario. However, the extent of 'Gain' performance for UV light is much greater than that of visible light, necessary to contribute toward DUV application.

#### 6.2 Future Work

DUV-LEDs and other UV/DUV photonics are expected to have a wide range of applications besides being the alternative to the conventional mercury lamps. There are number of ideas which may be taken forward to realize the full potential of this research:

- Multiple substrates like sapphire and other combinations of III-V metrics (AlGaN; for instance) may be tried for optimum efficacy of the AlN template.
- A variety of UV to DUV lights with multiple light intensities may also be tried for the full spectrum of detection in terms of raising the potential of mass-manufactured device.
- During the growth of AlN; the substrate temperature may be increased to maximize the uniformity of the fabricated films. There is a likelihood that the process would yield lesser defects at the Silicon and Aluminum Nitride Interface which would be helpful during level and edge sensitive detection.
- In order to detect even larger range of photon energies; the multi energy implant sequences on the selected device architecture can also be tried. For futuristic approach, one can fabricate test devices with low energy implantation using He<sup>+</sup>, P<sup>+</sup>, Au<sup>+</sup> and C<sup>+</sup> ions to only damage the surface/near-surface regions retaining the bulk properties intact.
- Internal quantum efficiency, current injection efficiency, and light extraction efficiency are very much dependent of the crystalline quality of the substrate template, and

thus further research and process engineering is required to reduce the density of crystalline defects including the Threading Dislocations (TDs) and Point Defects (PDs). These defects, in most of the photonic ICs and device applications, tend to act as Shockley-Read-Hall (SRH) type non-radiative recombination centers.

- It will also be interesting to see the behavior of various kinds of doping strategies in AlN template and their subsequent effect on the device's output performance. Further; it will be important to find out as to how to fabricate the optical devices requiring the high injection efficiencies of the carriers (both n- and p-type) simultaneously.
- Detailed investigation on the new ellipsometry models for the AlN template may be required to best fit the new optical applications. This is important to address in the wake of the importance of the optical constants. For instance; the refractive index contrast between the AlN/Si and the air is rather large and there may be a probable formation of total reflection. In such a case, an increase in the light extraction efficiency is suggested. This would require robust optical modeling to choose the optimized parameters for the device fabrication.
  - The energy efficient deep ultra-violet optoelectronic devices suffer from critical
    issues associated with poor quality and large strain of nitride material system caused
    by the inherent mismatch of heteroepitaxy. A strain free AlN film with low
    dislocation density by graphene (Gr)-driving strain-pre-store engineering and a
    unique mechanism of strain-relaxation in quasi-van der waals epitaxy can be
    presented.
  - Growing III-V semiconductor materials on Si substrates for optoelectronics application is challenging because of their high lattice mismatch and different thermal coefficients, which cause the epitaxial layer to have a lower quality. A high quality AIN template can be grown on a micro-channel-patterned Si substrate using NH<sub>3</sub> pulsed flow multilayer AIN growth and epitaxial lateral overgrowth techniques.

 The effect of the quality of the Si substrate and the AlN layer can be separately researched and reported for the key aspect of DUV device efficiency, reliability, and longevity.

#### References

- [1] Sliney, D. H. (2001). Photoprotection of the eye-UV radiation and sunglasses. Journal of Photochemistry and Photobiology B: Biology, 64(2-3), 166-175.
- [2] Boyce, P. R. (2010). The impact of light in buildings on human health. Indoor and Built environment, 19(1), 8-20.
- [3] Parker, E. R. (2021). The influence of climate change on skin cancer incidence—A review of the evidence. International Journal of Women's Dermatology, 7(1), 17-27.
- [4] McCullagh, C., Robertson, J. M., Bahnemann, D. W., & Robertson, P. K. (2007). The application of TiO 2 photocatalysis for disinfection of water contaminated with pathogenic micro-organisms: a review. Research on Chemical Intermediates, 33(3), 359-375.
- [5] Sharma, P., Khan, M. Z., & Choubey, A. K. (2019). LED Revolution: Deep UV LED.
- [6] Liu, H., Zhang, Z., Hu, L., Gao, N., Sang, L., Liao, M., ... & Fang, X. (2014). New UV-A Photodetector Based on Individual Potassium Niobate Nanowires with High Performance. Advanced Optical Materials, 2(8), 771-778.
- [7] Ferry, D. K. (1975). High-field transport in wide-band-gap semiconductors. Physical Review B, 12(6), 2361.
- [8] Chattopadhyay, S., Ganguly, A., Chen, K. H., & Chen, L. C. (2009). One-dimensional group III-Nitrides: growth, properties, and applications in nanosensing and nano-optoelectronics. Critical Reviews in Solid State and Materials Sciences, 34(3-4), 224-279.
- [9] Zou, Y., Zhang, Y., Hu, Y., & Gu, H. (2018). Ultraviolet detectors based on wide bandgap semiconductor nanowire: A review. Sensors, 18(7), 2072.
- [10] Joshi, N. V. (2017). Photoconductivity: art, science, and technology. Routledge.
- [11] Berry, C. W. (2013). Plasmonic Photoconductors for Higher Performance Terahertz Radiation Sources (Doctoral dissertation
- [12] Liu, K., Sakurai, M., & Aono, M. (2010). ZnO-based ultraviolet photodetectors. Sensors, 10(9), 8604-8634.
- [13] Yang, X., & Yan, M. (2020). Removing contaminants from transferred CVD graphene. Nano Research, 13(3), 599-610.

- [14] Liang, F. X., Gao, Y., Xie, C., Tong, X. W., Li, Z. J., & Luo, L. B. (2018). Recent advances in the fabrication of graphene–ZnO heterojunctions for optoelectronic device applications.

  Journal of Materials Chemistry C, 6(15), 3815-3833.
- [15] Look, D. C. (2001). Recent advances in ZnO materials and devices. Materials Science and Engineering: B, 80(1-3), 383-387.
- [16] Peiris, S., de Silva, H. B., Ranasinghe, K. N., Bandara, S. V., & Perera, I. R. (2021). Recent development and future prospects of TiO2 photocatalysis. Journal of the Chinese Chemical Society, 68(5), 738-769.
- [17] Pan, Shusheng, and Guanghai Li. "Recent progress in p-type doping and optical properties of SnO2 nanostructures for optoelectronic device applications." Recent Patents on Nanotechnology 5.2 (2011): 138-161.
- [18] Dai, Z. R., Pan, Z. W., & Wang, Z. L. (2003). Novel nanostructures of functional oxides synthesized by thermal evaporation. Advanced Functional Materials, 13(1), 9-24.
- [19] Dai, Z. R., Pan, Z. W., & Wang, Z. L. (2003). Novel nanostructures of functional oxides synthesized by thermal evaporation. Advanced Functional Materials, 13(1), 9-24.
- [20] Vuong, D. D., Hien, V. X., Trung, K. Q., & Chien, N. D. (2011). Synthesis of SnO2 microspheres, nano-rods and nano-flowers via simple hydrothermal route. Physica E: Low-dimensional Systems and Nanostructures, 44(2), 345-349.
- [21] Zong-Mu, L., & Fa-Qiang, X. (2005). Synthesis and Characterization of SnO2 Onedimensional Nanostructures. Chinese Journal of Chemistry, 23(3), 337-340.
- [22] Dai, Zu Rong, Z. Wei Pan, and Z. L. Wang. "Novel nanostructures of functional oxides synthesized by thermal evaporation." Advanced Functional Materials 13.1 (2003): 9-24.
- [23] Koppens, F. H. L., Mueller, T., Avouris, P., Ferrari, A. C., Vitiello, M. S., & Polini, M. (2014). Photodetectors based on graphene, other two-dimensional materials and hybrid systems. Nature nanotechnology, 9(10), 780-793.
- [24] Huang, X., Jiang, P., & Tanaka, T. (2011). A review of dielectric polymer composites with high thermal conductivity. IEEE Electrical Insulation Magazine, 27(4), 8-16.
- [25] Morkoc, B. H., Strite, S., Gao, G. B., Lin, M. E., Sverdlov, B., & Burns, M. (1994). Large-band-gap SiC, III-V nitride, and II-VI ZnSe-based semiconductor device technologies. Journal of Applied physics, 76(3), 1363-1398.
- [26] Ning, C. Z., Dou, L., & Yang, P. (2017). Bandgap engineering in semiconductor alloy nanomaterials with widely tunable compositions. Nature Reviews Materials, 2(12), 1-14.
- [27] Zou, Y., Zhang, Y., Hu, Y., & Gu, H. (2018). Ultraviolet detectors based on wide bandgap semiconductor nanowire: A review. Sensors, 18(7), 2072.
- [28] Azani, M. R., Hassanpour, A., & Torres, T. (2020). Benefits, Problems, and Solutions of Silver Nanowire Transparent Conductive Electrodes in Indium Tin Oxide (ITO)-Free Flexible Solar Cells. Advanced Energy Materials, 10(48), 2002536.
- [29] Zou, Y., Zhang, Y., Hu, Y., & Gu, H. (2018). Ultraviolet detectors based on wide bandgap semiconductor nanowire: A review. Sensors, 18(7), 2072.
- [30] Morkoc, B. H., Strite, S., Gao, G. B., Lin, M. E., Sverdlov, B., & Burns, M. (1994). Large-band-gap SiC, III-V nitride, and II-VI ZnSe-based semiconductor device technologies. Journal of Applied physics, 76(3), 1363-1398.

- [31] Zou, Y., Zhang, Y., Hu, Y., & Gu, H. (2018). Ultraviolet detectors based on wide bandgap semiconductor nanowire: A review. Sensors, 18(7), 2072.
- [32] Jia, L., Zheng, W., & Huang, F. (2020). Vacuum-ultraviolet photodetectors. PhotoniX, 1(1),
   1-25. [33] Fitzgerald, B. W. (2018). Exploring the electromagnetic spectrum with superheroes. Physics Education, 54(1), 015019.
- [33] Weinstein, L. A. (1988). Electromagnetic waves. Radio i svyaz', Moscow.
- [34] Westerhoff, P., Alvarez, P. J., Kim, J., Li, Q., Alabastri, A., Halas, N. J., ... & Wong, M. S. (2021). Utilizing the broad electromagnetic spectrum and unique nanoscale properties for chemical-free water treatment, Current Opinion in Chemical Engineering, 33, 100709.
- [35] Stecker, F. W. (1971). Cosmic gamma rays (Vol. 249). Scientific and Technical Information Office, National Aeronautics and Space Administration.
- [36] Ong, R. A. (1998). Very high-energy gamma-ray astronomy. Physics Reports, 305(3-4), 93-202
- [37] Assmus, A. (1995). Early history of X rays. Beam Line, 25(2), 10-24.
- [38] Clarke, C., & Dux, A. (2015). Abdominal X-rays for Medical Students. John Wiley & Sons.
- [39] Sharma, B. K. (1981). Instrumental methods of chemical analysis. Krishna Prakashan Media.
- [40] Luo, X., Zhang, B., Lu, Y., Mei, Y., & Shen, L. (2022). Advances in application of ultraviolet irradiation for biofilm control in water and wastewater infrastructure. Journal of Hazardous Materials, 421, 126682.
- [41] Freeman, S. E., Hacham, H., Gange, R. W., Maytum, D. J., Sutherland, J. C., & Sutherland, B. M. (1989). Wavelength dependence of pyrimidine dimer formation in DNA of human skin irradiated in situ with ultraviolet light. Proceedings of the National Academy of Sciences, 86(14), 5605-5609.
- [42] Fang, H. B., Luo, Y., Zheng, Y. Z., Ma, W., & Tao, X. (2016). Facile large-scale synthesis of urea-derived porous graphitic carbon nitride with extraordinary visible-light spectrum photodegradation. Industrial & Engineering Chemistry Research, 55(16), 4506-4514.
- [43] Mahmoud, B. H., Hexsel, C. L., Hamzavi, I. H., & Lim, H. W. (2008). Effects of visible light on the skin. Photochemistry and photobiology, 84(2), 450-462.
- [44] Tadakuma, T. (1993). Possible application of the laser in immunobiology. The Keio journal of medicine, 42(4), 180-182. Somorjai, G. A., & Rupprechter, G. (1999). Molecular studies of catalytic reactions on crystal surfaces at high pressures and high temperatures by infrared—visible sum frequency generation (SFG) surface vibrational spectroscopy. The Journal of Physical Chemistry B, 103(10), 1623-1638.
- [45] Somorjai, G. A., & Rupprechter, G. (1999). Molecular studies of catalytic reactions on crystal surfaces at high pressures and high temperatures by infrared—visible sum frequency generation (SFG) surface vibrational spectroscopy. The Journal of Physical Cherhistry B, 103(10), 1623-1638.
- [46] Haque, M. J., & Muntjir, M. (2017). Night Vision Technology: An Overview. International Journal of Computer Applications, 975, 8887.

- [47] Kumar, N., Singh, U., Singh, T. P., & Sinha, A. K. (2011). A review on the applications of high power, high frequency microwave source: Gyrotron. Journal of fusion energy, 30(4), 257-276.
- [48] Cooper, N. S. (2020). Microwave ovens. Development of Packaging and Products for Use in Microwave Ovens, 177-199..
- [49] Shinohara, N. (2019). Wireless Power Transmission: Inductive Coupling, Radio Wave, and Resonance Coupling. Advances in Energy Systems: The Large-scale Renewable Energy Integration Challenge, 211-220
- [50] Moliton, A., & Nunzi, J. M. (2006). How to model the behaviour of organic photovoltaic cells. Polymer International, 55(6), 583-600.
- [51] Yu, C., & Wang, H. (2010). Large lateral photovoltaic effect in metal-(oxide-) semiconductor structures. Sensors, 10(11), 10155-10180.
- [52] Qiao, S., Liang, B., Liu, J., Fu, G., & Wang, S. (2021). Lateral photovoltaic effect based on novel materials and external modulations. Journal of Physics D: Applied Physics, 54(15), 153003.
- [53] Copeland, A. W., Black, O. D., & Garrett, A. B. (1942). The Photovoltaic Effect. Chemical reviews, 31(1), 177-226.
- [54] Fridkin, V. M., & Popov, B. (1978). Anomalous photovoltaic effect in ferroelectrics. Soviet Physics Uspekhi, 21(12), 981.
- [55] Brongersma, M. L., Halas, N. J., & Nordlander, P. (2015). Plasmon-induced hot carrier science and technology. Nature nanotechnology, 10(1), 25-34.
- [56] Marghany, M. (2019). Synthetic Aperture Radar Imaging Mechanism for Oil Spills. Gulf Professional Publishing.
- [57] Klassen, S. (2011). The photoelectric effect: Reconstructing the story for the physics classroom. Science & Education, 20(7), 719-731.
- [58] Pospischil, A., Furchi, M. M., & Mueller, T. (2014). Solar-energy conversion and light emission in an atomic monolayer p-n diode. Nature nanotechnology, 9(4), 257-261.
- [59] Yang, L., Wang, S., Zeng, Q., Zhang, Z., & Peng, L. M. (2013). Carbon nanotube photoelectronic and photovoltaic devices and their applications in infrared detection. Small, 9(8), 1225-1236.
- [60] Hannan, M. A., Lipu, M. H., Ker, P. J., Begum, R. A., Agelidis, V. G., & Blaabjerg, F. (2019). Power electronics contribution to renewable energy conversion addressing emission reduction: Applications, issues, and recommendations. Applied energy, 251, 113404.
- [61] Kabir, M. Z. (2015). Dark current mechanisms in amorphous selenium-based photoconductive detectors: an overview and re-examination. Journal of Materials Science: Materials in Electronics, 26(7), 4659-4667.
- [62] He, X., Léonard, F., & Kono, J. (2015). Uncooled carbon nanotube photodetectors. Advanced Optical Materials, 3(8), 989-1011.
- [63] He, X., Léonard, F., & Kono, J. (2015). Uncooled carbon nanotube photodetectors. Advanced Optical Materials, 3(8), 989-1011.

- [64] Bazkir, Ö. (2009). Quantum efficiency determination of unbiased silicon photodiode and photodiode based trap detectors. Rev. Adv. Mater. Sci, 21(1), 90-98.
- [65] Vuoristo, P. (2014). Thermal spray coating processes. In Comprehensive materials processing, 1st edition Volume 4: Coatings and films (pp. 229-276). Elsevier.
- [66] Beling, A., & Campbell, J. C. (2014). High-speed photodiodes. IEEE Journal of Selected Topics in Quantum Electronics, 20(6), 57-63.
- [67] Campbell, J. C. (2007). Recent advances in telecommunications avalanche photodiodes. Journal of Lightwave Technology, 25(1), 109-121.
- [68] Andelković, M. S., & Ristić, G. S. (2013). Feasibility study of a current mode gamma radiation dosimeter based on a commercial PIN photodiode and a custom made auto-ranging electrometer. Nuclear Technology and Radiation Protection, 28(1), 73-83.
- [69] Gradišnik, V., & Linić, A. (2013). Defects characterization in pin a-Si: H photodiode i-layer. Journal of non-crystalline solids, 363, 193-198.
- [70] Anzivino, G., Arnaudon, H., Baillon, P., Benetti, P., Boskma, L., Burger, P., ... & Zhao, M. (1995). Review of the hybrid photo diode tube (HPD) an advanced light detector for physics. Nuclear Instruments and Methods in Physics Research Section A: Accelerators, Spectrometers, Detectors and Associated Equipment, 365(1), 76-82.
- [71] Singh, A., Srivastav, V., & Pal, R. (2011). HgCdTe avalanche photodiodes: A review. Optics & Laser Technology, 43(7), 1358-1370.
- [72] Youn, D. H., Kim, H. T., & Kang, K. Y. (2005). Observation of abrupt metallic transitions in p-type GaAs devices and comparison with avalanche breakdown in the InGaAs APD. Journal of the Korean Physical Society, 47(1), 1-5.
- [73] Brennan, K. F., Haralson II, J., Parks Jr, J. W., & Salem, A. (1999). Review of reliability issues of metal-semiconductor-metal and avalanche photodiode photonic detectors. Microelectronics Reliability, 39(12), 1873-1883.
- [74] Ahmed, A. A., Devarajan, M., & Afzal, N. (2017). Fabrication and characterization of high performance MSM UV photodetector based on NiO film. Sensors and Actuators A: Physical, 262, 78-86.
- [75] Ababneh, A., Albataineh, Z., Dagamseh, A. M. K., Al-kofahi, I. S., Schäfer, B., Zengerle, T., & Seidel, H. (2020). Optical characterization of sputtered aluminum nitride thin films—correlating refractive index with degree of c-axis orientation. Thin Solid Films, 693, 137701.
- [76] Mondal, R. K., Adhikari, S., Chatterjee, V., & Pal, S. (2021). Recent Advances and Challenges in AlGaN-based Ultra-violet Light Emitting Diode Technologies. Materials Research Bulletin, 111258.
- [77] Porcel, M. A., Hinojosa, A., Jans, H., Stassen, A., Goyvaerts, J., Geuzebroek, D., ... & Artundo, I. (2019). Silicon nitride photonic integration for visible light applications. Optics & Laser Technology, 112, 299-306.
- [78] Ma, Z., Almalki, A., Yang, X., Wu, X., Xi, X., Li, J., ... & Zhao, L. (2020). The influence of point defects on AlGaN-based deep ultraviolet LEDs. Journal of Alloys and Compounds, 845, 156177.
- [79] Taniyasu, Y., & Kasu, M. (2008). Aluminum nitride deep-ultraviolet light-emitting p-n junction diodes. Diamond and related materials, 17(7-10), 1273-1277.

- [80] Legesse, M., Rashkeev, S. N., Saidaoui, H., El Mellouhi, F., Ahzi, S., & Alharbi, F. H. (2020). Band gap tuning in aluminum doped two-dimensional hexagonal boron nitride. Materials Chemistry and Physics, 250, 123176.
- [81] Naderi, N., & Moghaddam, M. (2020). Ultra-sensitive UV sensors based on porous silicon carbide thin films on silicon substrate. Ceramics International, 46(9), 13821-13826.
- [82] Zhang, D., Mylsamy, G., Yang, X., Xie, Z., Su, X., Liang, F., ... & Dai, Y. (2021). High purity and good dispersity AlN nanoparticles synthesized by an arc discharge with assistance of direct nitridation. Ceramics International, 47(12), 16972-16979.
- [83] Asghar, M., Iqbal, F., Faraz, S., Jokubavicius, V., Wahab, Q., & Syväjärvi, M. (2012). Characterization of deep level defects in sublimation grown p-type 6H-SiC epilayers by deep level transient spectroscopy. Physica B: Condensed Matter, 407(15), 3041-3043.
- [84] Lee, J., Jang, E. H., Chang, W. S., Jeong, S., Lee, E., Jeong, J. H., & Choi, J. H. (2018). High performance ultraviolet photodetector based on a spray-coated nanocrystal quantum dots layer and Si photodiode. Sensors and Actuators A: Physical, 273, 182-188.
- [85] Ahmad, H., & Tamil, T. M. K. (2018). Enhancement of broadband ultraviolet visible photodetection by boron nitride nanoparticles in bulk graphene oxide layer. Optical Materials, 86, 18-23.
- [86] Zielony, E., Przezdziecka, E., Placzek-Popko, E., Lisowski, W., Stachowicz, M., Paradowska, K. M., ... & Kozanecki, A. (2018). Deep levels in the MBE ZnO: As/n-GaN diodes—Photoluminescence, electrical properties and deep level transient spectroscopy. Journal of Alloys and Compounds, 742, 296-303.
- [87] Jiang, H, Wang, X. H., Lei, W, Fan, G. F., & Lu, W. Z. (2019) Effects of two-step sintening on thermal and mechanical properties of aluminum nitride ceramics by impedance spectroscopy analysis. *Journal of the European Ceramic Society*, 39(2-3), 249-254
- [88] Fahad, S., Noman, M., Qureshi, A. F., Alı, M., & Ahmed, S. (2021). Defect mapping of active layer of CdTe solar cells using charge deep level transient spectroscopy (Q-DLTS). Engineering Failure Analysis, 119, 104991.
- [89] Kern, W., & Schuegraf, K. K. (2001). Deposition technologies and applications: Introduction and overview. In Handbook of Thin Film Deposition Processes and Techniques (pp. 11-43).
  William Andrew Publishing.
- [90] Asahi, H., & Horikoshi, Y. (Eds.). (2019). Molecular beam epitaxy: materials and applications for electronics and optoelectronics. John Wiley & Sons.
- [91] Katsuhiro Tomioka, Takashi Fukui, in Handbook of Crystal Growth (Second Edition), 2015
- [92] Monemar, B., Larsson, H., Hemmingsson, C., Ivanov, I. G., & Gogova, D. (2005). Growth of thick GaN layers with hydride vapour phase epitaxy. Journal of crystal growth, 281(1), 17-31.
- [93] Mattox, D. M. (2010). Handbook of physical vapor deposition (PVD) processing. William Andrew.
- [94] Helmersson, U., Lattemann, M., Bohlmark, J., Ehiasarian, A. P., & Gudmundsson, J. T. (2006). Ionized physical vapor deposition (IPVD): A review of technology and applications. Thin solid films, 513(1-2), 1-24.

- [95] Ghader Faraji, Hyoung Seop Kim, Hessam Torabzadeh Kashi, Introduction, Editor(s): Ghader Faraji, Hyoung Seop Kim, Hessam Torabzadeh Kashi, Severe Plastic Deformation, Elsevier, 2018, Pages 1-17,
- [96] Muhammad Shahid Rafique, Muhammad Rafique, Muhammad Bilal Tahir, Syeda Hajra, Tasmia Nawaz, Falak Shafiq, Chapter 3 - Synthesis methods of nanostructures, Editor(s): Muhammad Bilal Tahir, Muhammad Rafique, Muhammad Shahid Rafique, In Micro and Nano Technologies, Nanotechnology and Photocatalysis for Environmental Applications, Elsevier, 2020, Pages 45-56,
- [97] Bekir Sami Yilbas, Abdullah Al-Sharafi, Haider Ali, Chapter 3 Surfaces for Self-Cleaning, Editor(s): Bekir Sami Yilbas, Abdullah Al-Sharafi, Haider Ali, Self-Cleaning of Surfaces and Water Droplet Mobility, Elsevier, 2019, Pages 45-98,
- [98] Saive, R. (2019). S-Shaped current-voltage characteristics in solar cells: A review. IEEE journal of photovoltaics, 9(6), 1477-1484.
- [99] Chikh-Bled, B., Benyoucef, B., & Aillerie, M. (2012). Experimental measurement of electric conductivity and activation energy in congruent lithium niobate crystal. Journal of Active and Passive Electronic Devices, 7(3), 261-270.
- [100] Lee, K., Shur, M. S., Drummond, T. J., & Morkoc, H. (1983). Current—Voltage and capacitance—Voltage characteristics of modulation-doped field-effect transistors. IEEE Transactions on Electron Devices, 30(3), 207-212.
- [101] Oskar J. Sandberg, Kristofer Tvingstedt, Paul Meredith, and Ardalan Armin The Journal of Physical Chemistry C 2019 123 (23), 14261-14271 DOI: 10.1021/acs.jpcc.9b03133
- [102] Ryan, J. W., & Palomares, E. (2017). Photo-Induced Charge Carrier Recombination Kinetics in Small Molecule Organic Solar Cells and the Influence of Film Nanomorphology. Advanced Energy Materials, 7(10), 1601509.
- [103] Wei Zheng, Lemin Jia, Feng Huang, Vacuum-Ultraviolet Photon Detections, iScience, Volume 23, Issue 6, 2020, 101145.
- [104] Yang, J. L., Liu, K. W., & Shen, D. Z. (2017). Recent progress of ZnMgO ultraviolet photodetector. Chinese Physics B, 26(4), 047308.
- [105] Fujiwara, H. (2007). Spectroscopic ellipsometry: principles and applications. John Wiley & Sons.
- [106] Veli-Matti Airaksinen, Chapter 15 Silicon Wafer and Thin Film Measurements, Editor(s): Markku Tilli, Teruaki Motooka, Veli-Matti Airaksinen, Sami Franssila, Mervi Paulasto-Kröckel, Veikko Lindroos, In Micro and Nano Technologies, Handbook of Silicon Based MEMS Materials and Technologies (Second Edition), William Andrew Publishing, 2015, Pages 381-390,
- [107] Vernon-Parry, K. D. (2000). Scanning electron microscopy: an introduction. III-Vs Review, 13(4), 40-44.
- [108] Ashok K. Singh, Chapter 4 Experimental Methodologies for the Characterization of Nanoparticles, Editor(s): Ashok K. Singh, Engineered Nanoparticles, Academic Press, 2016, Pages 125-170,

- [109] Choudhary, S. (2010). Uranium and Other Heavy Metal Resistance and Accumulation in a Pseudomonas Aeruginosa Strain: Potential in Bioremediation (Doctoral dissertation, IIT Kharagpur).
- [110] Paprocki, K., Fabisiak, K., Bogdanowicz, R., Gołuński, Ł., Staryga, E., Szybowicz, M., ... & Banaszak-Piechowska, A. (2017). Charge-based deep level transient spectroscopy of B-doped and undoped polycrystalline diamond films. Journal of Materials Science, 52(17), 10119-10126. DOI: 10.1007/s10853-017-1217-0
- [111] Hussain, K., Shuja, A., Ali, M., & Fahad, S. (2020). Carrier removal and transport in photonic integrated circuit ready InGaAsP/InP substrate: Electrical and transients of charges evaluation. Materials Science in Semiconductor Processing, 121, 105384. DOI: 10.1016/j.mssp.2020.105384
- [112] Fahad, S., Noman, M., Qureshi, A. F., Ali, M., & Ahmed, S. Defect mapping of active layer of CdTe solar cells using charge deep level transient spectroscopy (Q-DLTS). Engineering Failure Analysis, 119, 104991. DOI: 10.1016/j.engfailanal.2020.104991
- [113] R. Marnadu, J. Chandrasekaran, S. Maruthamuthu, V. Balasubramani, P. Vivek, R. Suresh, Ultra-high photoresponse with superiorly sensitive metal-insulatorsemiconductor (MIS) structured diodes for UV photodetector application, Appl. Surf. Sci. 480 (2019) 308–322.
- [114] Schwendeman, I. (2002). Optical and transport properties of conjugated polymers, and their application to electrochromic devices. University of Florida.
- [115] Y. Taniyasu, M. Kasu, Aluminum nitride deep-ultraviolet light-emitting p-n junction diodes, Diam. Relat. Mater. 17 (7-10) (2008) 1273-1277
- [116] D. Thomson, A. Zilkie, J.E. Bowers, T. Komljenovic, G.T. Reed, L. Vivien, J.M. Hartmann, Roadmap on silicon photonics, J. Opt. 18 (7) (2016), 073003
- [117] Thomson, D., Zilkie, A., Bowers, J. E., Komljenovic, T., Reed, G. T., Vivien, L., ... & Nedeljkovic, M. (2016). Roadmap on silicon photonics. Journal of Optics, 18(7), 073003.
- [118] L. Tian, Y. Wang, E. Jin, Y. Li, R. Wang, Y. Shang, Aluminum nitride-filled elastic silicone rubber composites for drag reduction, Adv. Mech. Eng. 9 (4) (2017)
- [119] N. Alfaraj, J.W. Min, C.H. Kang, A.A. Alatawi, D. Priante, R.C. Subedi, B.S. Ooi, Deepultraviolet integrated photonic and optoelectronic devices: a prospect of the hybridization of group III-nitrides, III-oxides, and two-dimensional materials, J. Semiconduct. 40 (12) (2019) 121801
- [120] R.K. Choudhary, P. Mishra, A. Biswas, A.C. Bidaye, Structural and optical properties of aluminum nitride thin films deposited by pulsed dc magnetron sputtering, International Scholarly Research Notices (2013)
- [121] Y. Li, W. Wang, X. Li, L. Huang, Y. Zheng, X. Chen, G. Li, Nucleation layer design for growth of a high-quality AIN epitaxial film on a Si (111) substrate, CrystEngComm 20 (11) (2018) 1483–1490.
- [122] G.S. Kim, S.Y. Lee, J.H. Hahn, Synthesis of CrN/AlN superlattice coatings using closed-field unbalanced magnetron sputtering process, Surf. Coating. Technol. 171 (1-3) (2003) 91-95
- [123] G.F. Iriarte, F. Engelmark, I.V. Katardjiev, Reactive sputter deposition of highly oriented AlN films at room temperature, J. Mater. Res. 17 (6) (2002) 1469–1475

- [124] E. Simoen, D. Visalli, M. Van Hove, M. Leys, P. Favia, H. Bender, A. Stesmans, Electrically active defects at AlN/Si interface studied by DLTS and ESR, Phys. Status Solidi 209 (10) (2012) 1851–1856
- [125] V. Ligatchev, Rusli, Z. Pan, Density of defect states of aluminum nitride grown on silicon and silicon carbide substrates at room temperature, Appl. Phys. Lett. 87 (24) (2005) 242903.
- [126] K. Hussain, A. Shuja, M. Ali, Z. Ibrahim, Q. Mehmood, Ion-induced electrical isolation in GaN-based platform for applications in integrated photonics, IEEE Access 7 (2019) 184303– 184311
- [127] D.J. Xi, Y.D. Zheng, P. Chen, R.M. Chu, S.L. Gu, B. Shen, R. Zhang, Study on the AlN/Si (111) interface properties, Opt. Mater. 23 (1-2) (2003) 143-146.
- [128] K. Hussain, A. Shuja, M. Ali, S. Fahad, Carrier removal and transport in photonic integrated circuit ready InGaAsP/InP substrate: electrical and transients of charges evaluation, Mater. Sci. Semicond. Process. 121 (2020) 105384.
- [129] Fahad, S., Noman, M., Qureshi, A. F., Ali, M., & Ahmed, S. Defect mapping of active layer of CdTe solar cells using charge deep level transient spectroscopy (Q-DLTS). Eng. Fail. Anal., 119, 104991. DOI: 10.1016/j.engfailanal.2020.104991
- [130] K. Paprocki, K. Fabisiak, R. Bogdanowicz, Ł. Gołunski, 'E. Staryga, M. Szybowicz, A. Banaszak-Piechowska, Charge-based deep level transient spectroscopy of Bdoped and undoped polycrystalline diamond films, J. Mater. Sci. 52 (17) (2017) 10119-10126
- [131] M. Ali, S. Ahmed, F. Younus, Z. Ali, Electrical, charge transients and photo response study of as-deposited and phosphorus implanted Cd1-xZnxTe devices for PV applications, Radiat. Phys. Chem. 166 (2020) 108498
- [132] J.B. Rothenberger, D.E. Montenegro, M.A. Prelas, T.K. Ghosh, R.V. Tompson, S. K. Loyalka, A Q-DLTS investigation of aluminum nitride surface termination, J. Mater. Res. 27 (8) (2012) 1198-1204,
- [133] Y. Taniyasu, M. Kasu, Aluminum nitride deep-ultraviolet light-emitting p-n junction diodes, Diam. Relat. Mater. 17 (7-10) (2008) 1273-1277...
- [134] B. Neuschl, K. Thonke, M. Feneberg, R. Goldhahn, T. Wunderer, Z. Yang, Z. Sitar, Direct determination of the silicon donor ionization energy in homoepitaxial AIN from photoluminescence two-electron transitions, Appl. Phys. Lett. 103 (12) (2013) 122105.
- [135] Lee, W. Y., Lackey, W. J., & Agrawal, P. K. (1991). Kinetic analysis of chemical vapor deposition of boron nitride. Journal of the American Ceramic Society, 74(10), 2642-2648.
- [136] Khan, A. H., Odeh, M. F., Meese, J. M., Charlson, E. M., Charlson, E. J., Stacy, T., ... & Wragg, J. L. (1994). Growth of oriented aluminium nitride films on silicon by chemical vapour deposition. Journal of materials science, 29(16), 4314-4318.
- [137] Yoshida, S., Misawa, S., Fujii, Y., Takada, S., Hayakawa, H., Gonda, S., & Itoh, A. (1979). Reactive molecular beam epitaxy of aluminium nitride. Journal of Vacuum Science and Technology, 16(4), 990-993.
- [138] An, Z., Men, C., Xu, Z., Chu, P. K., & Lin, C. (2005). Electrical properties of AlN thin films prepared by ion beam enhanced deposition. Surface and Coatings Technology, 196(1-3), 130-134.

- [139] Lin, W. T., Meng, L. C., Chen, G. J., & Liu, H. S. (1995). Epitaxial growth of cubic AlN films on (100) and (111) silicon by pulsed laser ablation. Applied physics letters, 66(16), 2066-2068.
- [140] Okano, H., Takahashi, Y., Tanaka, T., Shibata, K., & Nakano, S. (1992). Preparation of c-axis oriented AlN thin films by low-temperature reactive sputtering. Japanese journal of applied physics, 31(10R), 3446.
- [141] Meng, W. J., Heremans, J., & Cheng, Y. T. (1991). Epitaxial growth of aluminum nitride on Si (111) by reactive sputtering. Applied physics letters, 59(17), 2097-2099.
- [142] Zhang, J. X., Cheng, H., Chen, Y. Z., Uddin, A., Yuan, S., Geng, S. J., & Zhang, S. (2005). Growth of AlN films on Si (100) and Si (111) substrates by reactive magnetron sputtering. Surface and Coatings Technology, 198(1-3), 68-73.
- [143] Kamber, D. S., Wu, Y., Letts, E., DenBaars, S. P., Speck, J. S., Nakamura, S., & Newman, S. A. (2007). Lateral epitaxial overgrowth of aluminum nitride on patterned silicon carbide substrates by hydride vapor phase epitaxy. Applied physics letters, 90(12), 122116.
- [144] Bing-Hwai Hwang, Chi-Shan Chen, Hong-Yang Lu, Tzu-Chien Hsu, Growth mechanism of reactively sputtered aluminum nitride thin films, Materials Science and Engineering: A, Volume 325, Issues 1–2, 2002, Pages 380-388,
- [145] Li, Y., Wang, W., Li, X., Huang, L., Zheng, Y., Chen, X., & Li, G. (2018). Nucleation layer design for growth of a high-quality AlN epitaxial film on a Si (111) substrate.

  CrystEngComm, 20(11), 1483-1490.
- [146] Rothenberger, J. B., Montenegro, D. E., Prelas, M. A., Ghosh, T. K., Tompson, R. V., & Loyalka, S. K. (2012). A Q-DLTS investigation of aluminum nitride surface termination. Journal of Materials Research, 27(8), 1198-1204.
- [147] Simoen, E., Visalli, D., Van Hove, M., Leys, M., Favia, P., Bender, H., ... & Stesmans, A. (2012). Electrically active defects at AlN/Si interface studied by DLTS and ESR. physica status solidi (a), 209(10), 1851-1856.
- [148] Ligatchev, V., Rusli, & Pan, Z. (2005). Density of defect states of aluminum nitride grown on silicon and silicon carbide substrates at room temperature. Applied Physics Letters, 87(24), 242903.

